

MAXIMUM TORQUE PER AMPERE (MTPA) CONTROL FOR PERMANENT
MAGNET SYNCHRONOUS MACHINE DRIVE SYSTEM

A Thesis

Presented to

The Graduate Faculty of The University of Akron

In Partial Fulfillment

of the Requirements for the Degree

Master of Science

Adeeb Ahmed

August, 2013

MAXIMUM TORQUE PER AMPERE (MTPA) CONTROL FOR PERMANENT
MAGNET SYNCHRONOUS MACHINE DRIVE SYSTEM

Adeeb Ahmed

Thesis

Approved:

Accepted:

Advisor
Dr. Yilmaz Sozer

Department Chair
Dr. J. Alexis De Abreu Garcia

Committee member
Dr. Malik Elbuluk

Dean of the College
Dr. George K. Haritos

Committee Member
Dr. Tom T. Hartley

Dean of the Graduate School
Dr. George R. Newkome

Date

ABSTRACT

A novel speed control algorithm for permanent magnet synchronous motors (PMSM) which maximizes efficiency without requiring phase current sensors is proposed in this thesis. The algorithm is described for a buried magnet type interior permanent magnet (IPM) motor but it is also suitable for surface mount type motors. The suggested algorithm implements maximum torque per ampere (MTPA) control in a PMSM drive system, considering the parameter variations due to magnetic saturation and change in temperature. Only DC link current, DC bus voltage and mechanical speed are used in the implementation of the algorithm, eliminating the requirement for three phase current measurements. The scheme employs an online search algorithm with an initial condition computed from a-priori system information. Hybridization of the search algorithm with pre-computed control coefficients ensures robustness against parameter variations while maintaining good dynamic performance. The proposed scheme is implemented on a 1.5 HP IPM and the validity of the approach is justified through experimental and simulation results.

ACKNOWLEDGEMENTS

I would like to thank my advisor Dr. Yilmaz Sozer for his constant guidance and supervision. I would also like to thank my committee members Dr. Malik Elbuluk and Dr. Tom T. Hartley for their guidance. I also wish to express my gratitude to Mr. Erik Rinaldo and Mr. Dale Ertley for their prompt support concerning any mechanical issues I have encountered through the course of this study.

TABLE OF CONTENTS

	Page
LIST OF TABLES	viii
LIST OF FIGURES	ix
CHAPTER	
I. INTRODUCTION	1
1.1. Overview	1
1.2. Thesis Objectives	2
1.3. Organization of Thesis	3
II. PMSM MODEL AND PRELIMINARIES	4
2.1. Basic structure of PMSM	4
2.2. Three Phase Model	6
2.3. Effects of Parameter Variation	8
2.4. Vector Control Preliminaries	10
2.5. Motor Model in dq Reference Frame	13
2.6. Parameter Variations in dq Reference Frame	14
III. LITERATURE REVIEW	16
3.1. Maximum Torque per Ampere Definition	16
3.2. Previous work on MTPA	21
3.2.1. A-Priori Methods	21

3.2.2. Methods Based on Search Algorithm	27
IV. PROPOSED CONTROL SCHEME	29
4.1. Experimental and Simulation Motor Parameters	29
4.2. Preliminary Block Diagram	30
4.3. Analytical Background.....	34
4.4. Phase Advance Angle Based on Ideal Motor Model	39
4.5. Incorporating Non-idealities in Motor Model	40
4.6. Maximum Power per Ampere Concept (MPPA)	44
4.7. Procedure for Finding the Optimum Phase Advance Angle (δ_{opt})	45
4.8. MTPA and MPPA Coincidence	50
4.9. Analysis for Optimum δ_{opt}	55
4.10. Estimation for Optimum δ_{opt}	57
4.11. Convergence of the Proposed Algorithm	65
4.12. Design Procedure of the PI Controller	67
4.13. Compensation for Temperature Variation and Estimation Error	73
4.14. Proposed Control Scheme	75
V. SIMULATION RESULTS	77
5.1. Overview	77
5.2. Used Motor Model	77
5.3. Steady State Performance Analysis.....	78
5.4. Temperature Effects	82
VI. EXPERIMENTAL IMPLEMENTATION	87
6.1. Hardware Development.....	87

6.2. Design of Control Interface.....	87
6.3. Design of Interface Board	89
6.4. Current Conditioning Circuitry	90
6.5. Implementation of Position Decoding and Conditioning.....	91
6.6. Shoot Through Protection	91
6.7. Experimental Setup	92
6.8. Implementation of Space Vector Modulation	94
VII. EXPERIMENTAL RESULTS	99
7.1. Overview	99
7.2. Primary Data Collection.....	99
7.3. Load Torque Variation at Constant Speed	103
7.4. Speed Variation at Constant Load Torque	111
7.5. Effect of Gradient Descent Compensation.....	117
7.6. Steady State Current Wave Shapes	119
VII. CONCLUSION	123
BIBLIOGRAPHY.....	125

LIST OF TABLES

Table	Page
4-1: Experimental motor parameters	30
5-1: Motor parameters considered for higher temperature operation	83
6-1: Experimental implementation details	93
6-2: Duty ratios for different switches	97
7-1: Data obtained from procedure described in Section 4.7.....	101

LIST OF FIGURES

Figure	Page
2-1: External view of a typical PMSM (Photo courtesy: HNC)	5
2-2: Flux path for SPM motors. Flux linkage path is independent of rotor position resulting in constant inductance for all rotor angles (a) q -axis flux path (b) d -axis path ..	5
2-3: Flux path for IPM motors. (a) q -axis flux path has lower reluctance resulting in higher inductance. (b) d -axis path has higher reluctance which results in lower inductance	6
2-4: Three-phase equivalent circuit for PMSM considering saliency.	7
2-5: 3-phase equivalent circuit for PMSM considering saliency, magnetic saturation and temperature effects.....	9
2-6: Three phase voltage and $\alpha\beta$ reference frame.	10
2-7: dq PMSM model in rotor reference frame.....	13
2-8: dq PMSM model in rotor reference frame considering saturation and temperature effects.....	15
3-1: Variation in required i_q for different i_d values. Negative i_d produces more reluctance torque reducing the requirement for the i_q magnitude.	18
3-2: Magnetic torque produced by i_q ; this torque output is directly proportional to i_q and only parameter dependence occurs if there is any change in permanent magnet flux.....	18
3-3: Reluctance torque variation with i_d ; positive i_d creates negative reluctance torque which eliminates any positive desired value for i_d	19
3-4: Phase current magnitudes for different i_d values; point of minimum phase current varies for different torque level.....	19
3-5: i_q, i_d lines for generating desired torques; intersections of the constant torque lines and MTPA line represent the optimum i_q, i_d pairs for generating corresponding torques. The dotted quarter circle shows the current limit for a particular motor.	20

4-1: Basic block diagram for a conventional control scheme.....	31
4-2: Inside look of a typical voltage reference generator block.....	31
4-3: Preliminary block diagram for the proposed control scheme.....	33
4-4: Current magnitudes with change in phase advance angle δ at different load torque levels. Curves were generated considering the ideal motor model operating at 800 RPM. The locations marked by ∇ represent the minimum possible current magnitudes.	37
4-5: Required voltage magnitudes with change in phase advance angle δ at different load torque levels. (Optimum phase advance angles are marked by ∇).	38
4-6: Current magnitudes with change in phase advance angle δ at different speeds. Curves were generated considering ideal motor model operating at 0.4 Nm load torque and small viscous damping. The locations marked by ∇ represent the minimum possible current magnitudes.....	38
4-7: Required voltage magnitudes with change in phase advance angle δ at different speeds and 0.4 Nm load torque with some viscous damping. (Optimum phase advance angles are marked by ∇).....	39
4-8: Optimum phase advance angles as a function of torque and for different speed considering ideal motor model.....	40
4-9: Variation in quadrature axis inductance L_q with change in i_q	42
4-10: Variation in direct axis inductance L_d with change in i_q	43
4-11: Motor inductance measured using LCR meter for one mechanical or two electrical cycles (The dotted horizontal lines show quadrature and direct axis inductance values. Vertical dotted lines indicate the rotor d -axes).....	43
4-12: Constant speed operation for generating sufficient data to choose optimum phase advance angle δ . The small glitches on the speed represent the introduction of higher load torque at those instants.....	46
4-13: Load torque profile applied for each operating speeds data were taken.	47
4-14: The constant step variation of phase advance angle for different values of load torque. Each time any glitch detected in the speed profile represented an introduction of load torque which was used as a trigger for starting of a new ramp.....	47
4-15: Variation in required terminal voltage with the change in δ	48
4-16: Change in direct axis current with the change in phase advance angle. As anticipated, higher values of δ generated larger d -axis current in negative axis giving higher reluctance torque.....	48

4-17: Variation in quadrature axis current with the change in δ	49
4-18: Variation in DC link input power with the change in δ . The curve holds a ‘bowl’ shape at each torque level with the change in δ	49
4-19: DC link input power for different δ (700 RPM with 0.1 Nm load torque).	50
4-20: Current magnitude for different δ (700 RPM with 0.1 Nm load torque).	51
4-21: DC link input power for different δ (700 RPM with 0.5 Nm load torque).	51
4-22: Current magnitude for different δ (700 RPM with 0.5 Nm load torque).	52
4-23: DC link input power for different δ (700 RPM with 0.8 Nm load torque).	52
4-24: Current magnitude for different δ (700 RPM with 0.8 Nm load torque).	53
4-25: DC link input power with the change in δ obtained using simulation for 800 RPM.	54
4-26: Current phasor magnitude with the change in δ obtained using simulation for 800 RPM.	54
4-27: Optimum phase advance angle δ_{opt} with the variation of load torque and operating speed (Experimental).	55
4-28: Optimum phase advance angle δ_{opt} with the variation of load torque and operating speed (Simulation).	56
4-29: Optimum phase advance angle variation with load torque obtained for three different speed (Experimental).	56
4-30: Optimum phase advance angle variation with load torque obtained for three different speed (Simulation).	57
4-31: Optimum phase advance angle δ_{opt} as a function of DC link power and operating speed (Experimental).	58
4-32: Optimum phase advance angle δ_{opt} as a function of DC link power and operating speed (Simulation).	59
4-33: Optimum phase advance angle Vs. DC link input power obtained for three different speeds (Experimental).	59
4-34: Optimum phase advance angle Vs. DC link input power obtained for three different speeds (Simulation).	60

4-35: Optimum phase advance angle δ_{opt} estimated using Eqn. 4-20 for 800 RPM. Solid line presents the actual δ_{opt} whereas estimated angle is shown in dotted line.....	61
4-36: $M_{\omega ME}(1)$ plotted as a function of speed using Eqn. 4-22 (Shown in dotted line). The solid line shows $M_{\omega M}(1)$ obtained during primary adaptation of Least Square method.....	63
4-37: $M_{\omega ME}(2)$ plotted as a function of speed using Eqn. 4-22 (Shown in dotted line). The solid line shows $M_{\omega M}(2)$ obtained during primary adaptation of least square method.	63
4-38: Optimum phase advance angle δ_{opt} estimated using Eqn. 4-20 for 800 RPM. $M_{\omega M}$ vector for computing δ_{opt} was estimated using Eqn. 4-22. Solid line presents the actual δ_{opt} whereas estimated angle is shown in dotted line.	64
4-39: The bowl shaped DC link input power curve at 700 RPM with 0.1 Nm load torque (Zoomed in at the bottom of the curve).	66
4-40: Variation in δ is shown in blue step function which resulted power variation shown in Figure 4-38. δ_{opt} is marked by ∇ . The red line represents the phase advance angle calculated using estimation matrix D_M with power variation shown in Figure 4-38 as input.	66
4-41: Frequency response of the linearized system at $\omega_n = 143.8$ rad/sec and $V_n = 25$ Volt.	72
4-42: Frequency response of the PI controller.	72
4-43: Frequency response of the combined system.	73
4-44: Basic block diagram for error compensation.....	74
4-45: Motor connection diagram with necessary feedback signals	75
5-1: Torque output for load torque variation at 900 RPM.....	79
5-2: Phase advance angle variation with change in load torque at 900 RPM.....	79
5-3: DC Link input power variation at 900 RPM while step change in load torque was introduced in steps starting from 0.1 Nm. Dotted lines represent the minimum achievable power computed during motor training.	80
5-4: Quadrature axis current i_q variation during load variation at 900 RPM (Filtered value is shown).	80
5-5: Direct axis current i_d variation during load variation at 900 RPM (Filtered value is shown).....	81

5-6: Phase advance angle achieved at steady state are marked by ∇ . Angles computed during motor training for generating the D_M matrix are marked by square.....	81
5-7: i_q, i_d trajectory obtained by the algorithm is marked by ∇ . Trajectory computed during motor training is marked by square. Two dotted lines show the trajectory computed using constant motor model.	82
5-8: DC link input power at 900 RPM with 0.8 Nm load torque.....	84
5-9: DC link input power at 900 RPM with 0.8 Nm load torque at steady state.	84
5-10: i_q, i_d trajectory obtained by the algorithm when perturbation was ‘ON’ is marked by ∇ . Trajectory obtained without the aid of perturbation is marked by circles. Desired trajectory computed for higher temperature is marked by squares.	86
5-11: Desired phase advance angle at higher temperature is marked by squares. Phase advance angle achieved at steady state with and without the help of perturbation are marked by ∇ and circles respectively.....	86
6-1: dSPACE MicroAutobox II, Front and rear view.....	88
6-2: Simplified block diagram of the interfacing board (Only major sections are shown).	89
6-3: First order Low Pass Filter.	90
6-4: Butterworth filter used for encoder and voltage sensor output filtration.	91
6-5: Shoot through protection circuit.....	92
6-6: Experimental Setup	93
6-7: Basic block diagram for motor control using Space Vector Modulation for voltage regulation.	95
6-8: Space Vector Modulation Implementation.....	95
6-9: Voltage vectors in $\alpha\beta$ reference frame.....	96
6-10: 3-phase 50 Hz reference voltage V_a, V_b, V_c	98
6-11: Duty ratios for inverter upper switches.	98
7-1: i_q, i_d trajectories at different speeds computed from data obtained following the procedures described in Section 4.7. Two dotted lines show the trajectories computed using constant motor model.	101
7-2: Estimated Torque Output for load torque variation at 800 RPM.	104

7-3: Phase advance angle variation with change in load torque at 800 RPM.....	105
7-4: Contribution of phase advance angle variation from perturbation algorithm at 800 RPM.....	105
7-5: DC Link input power at 800 RPM while step change in load torque was introduced starting from 0.1 Nm. Dotted lines represent the minimum achievable power levels computed during motor training.	106
7-6: Quadrature axis current i_q during load variation at 800 RPM (Filtered value is shown).....	106
7-7: Direct axis current i_d during load variation at 800 RPM (Filtered value is shown).	107
7-8: Voltage magnitude during load variation at 800 RPM (Filtered value is shown)... ..	107
7-9: Speed Response of the motor with the application of load variation.	108
7-10: Phase advance angles achieved at steady state for 800 RPM are marked by ∇ . Angles computed during motor training for generating the D_M matrix are marked by squares.....	109
7-11: i_q, i_d trajectory at 800 RPM obtained by the algorithm is marked by ∇ . Trajectory computed during motor training is marked by squares. Two dotted lines show the trajectories computed using constant motor model.	110
7-12: Phase advance angles achieved at steady state for 700 RPM are marked by ∇ . Angles computed during motor training for generating the D_M matrix are marked by squares.....	110
7-13: i_q, i_d trajectory at 700 RPM obtained by the algorithm is marked by ∇ . Trajectory computed during motor training is marked by squares. Two dotted lines show the trajectories computed using constant motor model.	111
7-14: Speed response at constant load torque of 0.6 Nm.....	112
7-15: Estimated torque output at 0.6 Nm load torque. Generated torque increases with the increase in speed to overcome additional damping.	113
7-16: Phase advance angle generated by the control scheme for different speeds at 0.6 Nm load torque.	113
7-17: Contribution of phase advance angle variation from perturbation algorithm for different speeds at 0.6 Nm load torque.	114
7-18: Voltage magnitude during speed variation at 0.6 Nm load torque (Filtered value is shown).....	114

7-19: Quadrature axis current i_q during speed variation at 0.6 Nm load torque (Filtered value is shown).	115
7-20: Direct axis current i_d during speed variation at 0.6 Nm load torque (Filtered value is shown).	115
7-21: DC Link input power at 0.6 Nm while step change in speed command was introduced at 50 RPM interval starting from 700 RPM and ending at 900 RPM. Dotted lines represent the minimum achievable power levels computed during motor training.	116
7-22: Phase advance angles achieved at steady state for 0.6 Nm are marked by ∇ . Angles computed during motor training for generating the D_M matrix are marked by squares.	116
7-23: i_q, i_d trajectory at 0.6 Nm obtained by the algorithm is marked by ∇ . Trajectory computed during motor training is marked by squares. Two dotted lines show the trajectories computed using constant motor model.	117
7-24: Speed variation due to application of load torque at 1000 RPM. Speed response shows two glitches generating from the application and removal of sudden load torque.	118
7-25: DC link input power variation at 1000 RPM. The dotted line represents the power input with perturbation whereas the solid line is for phase advance angle solely estimated by D_M	119
7-26: Unfiltered DC link input power at 900 RPM.	120
7-27: Unfiltered direct axis current i_d at 900 RPM.	121
7-28: Unfiltered quadrature axis current i_q at 900 RPM.	121
7-29: Unfiltered three phase current at 900 RPM.	122

CHAPTER I

INTRODUCTION

1.1. Overview

Electric motors have been commonly used in many applications such as household appliances, hybrid and electric vehicles, off road traction systems and industrial processes as a means to convert electrical energy into mechanical energy. Being the largest consumer of electric power [1][2][3], electric motors have always received the attention of researchers.

Among the different types of electric motors, permanent magnet synchronous motors (PMSM) which do not require brushes for commutation, are gaining attention due to their high performance and efficient operation. Having permanent magnets (PM) on the rotor eliminates the rotor current requirement to generate the rotor field. Elimination of the rotor current enables more efficient operation compared to similar sized induction motors. Brushless operation ensures lower maintenance requirements and also eliminates the losses in the brushes. Properties such as lower maintenance cost, high torque density, and low torque to inertia ratio are making PMSMs attractive alternatives over other motors in applications such as spindle drives, air-conditioning compressors, cooling towers, electric vehicles and integrated starters and alternators [4][5][6][7][8].

PMSMs can be divided into two main categories based on their rotor structure, the surface mount type and the buried magnet type. In surface mount PMSMs or surface PM motors (SPMs), magnets are placed at the surface of the rotor using adhesive. This arrangement is not suitable for high speed operation since centrifugal force at high speed tends to throw the magnets out. Circularly symmetric placement of the magnets in SPMs creates an even path for the flux and gives the motor a non-salient structure.

Buried magnet type PMSMs are known as interior PM motors (IPMs). The buried magnet structure makes it robust for high speed operation [9] but asymmetric placement of magnets causes the IPM to exhibit magnetic saliency. The inductance of an IPM is therefore a function of rotor position and this causes the motor to have reluctance torque along with magnetic torque [4][10].

1.2. Thesis Objectives

Though the presence of rotor saliency provides an additional source of torque in IPMs, utilizing that advantage adds complexity in the control of these machines. IPMs produce sinusoidal 3-phase back EMF voltages that provide constant power if 3-phase sinusoidal current is maintained in the stator. Phase current components in phase with corresponding back EMF voltages (Quadrature axis current), produce only magnetic torque but do not contribute in producing reluctance torque. The current components 90 degrees out of phase with back EMF voltages (Direct axis current), produce reluctance torque in conjunction with quadrature axis currents. Thus, there exist an infinite number of current vectors providing the same amount of torque. For most efficient operation, the current vector with

the lowest possible magnitude should be chosen to reduce winding losses. Significant variation in motor parameters and operating conditions make it difficult to come up with optimum current vectors. In this thesis, a current minimizing control strategy, also known as Maximum Torque per Ampere (MTPA) control for IPMs is proposed. Rather than using conventional vector control, a method based on only DC link power measurement is suggested. Parameter variation arising from different sources is also considered in the control application.

1.3. Organization of Thesis

The basic model of an IPM is presented in Chapter II. The goal of the thesis and previous works concerning the objectives are presented in Chapter III. The proposed control scheme incorporated with some analysis of the motor behavior is addressed in Chapter IV. Simulation results are described in Chapter V. Preliminary setup description along with some fundamental procedures for algorithm implementation are presented in Chapter VI. Final experimental results are described in Chapter VII, and the conclusion is given in Chapter VIII.

CHAPTER II

PMSM MODEL AND PRELIMINARIES

2.1. Basic structure of PMSM

PMSMs are usually available in various sizes. The typical external view of a PMSM is shown in Figure 2-1. In most of the cases, a suitable position encoder placed inside the metal housing is provided by the manufacturer to ensure a robust structure.

Rotor structures of surface mount and buried magnet motors are shown in Figure 2-2 and Figure 2-3 respectively. Magnets have higher reluctance than iron and therefore, more magnet in the path of the flux reduces the inductance. For surface mount motors, the magnets are positioned in a circular shape around the rotor as shown in Figure 2-2. If the position of the rotor changes, the permanent magnet covered by the flux path essentially remains the same as shown in Figure 2-2(a) and Figure 2-2(b). Thus, for surface mount PM machines, inductance is not a function of angular position causing the motor to have a magnetically non-salient structure.

Figure 2-3(a) and Figure 2-3(b) show the flux path for an IPM for different rotor positions. The magnets inside the rotor are placed such a way that permanent magnet covered by the flux path changes with rotor position. This essentially causes the inductance to change with

rotor position. Figure 2-3(a) shows the position where flux path experiences the least amount of permanent magnet resulting in the highest possible inductance.



Figure 2-1: External view of a typical PMSM (Photo courtesy: HNC)

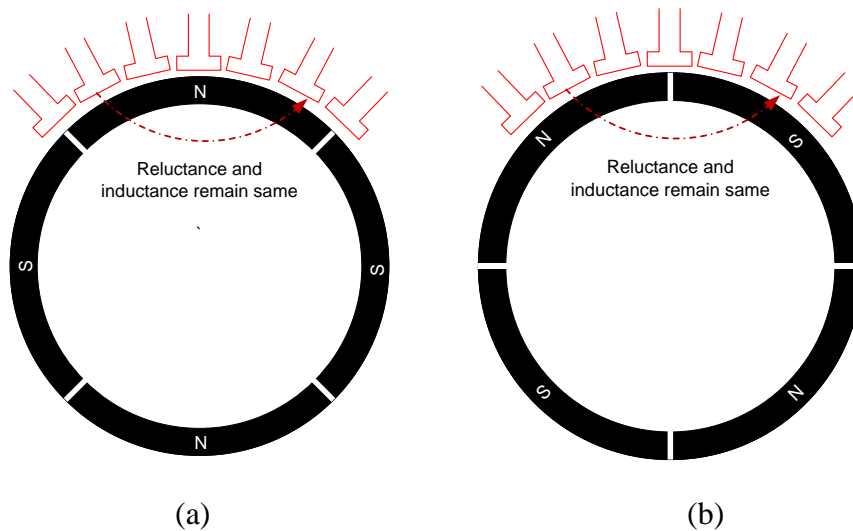


Figure 2-2: Flux path for SPM motors. Flux linkage path is independent of rotor position resulting in constant inductance for all rotor angles (a) q -axis flux path (b) d -axis path

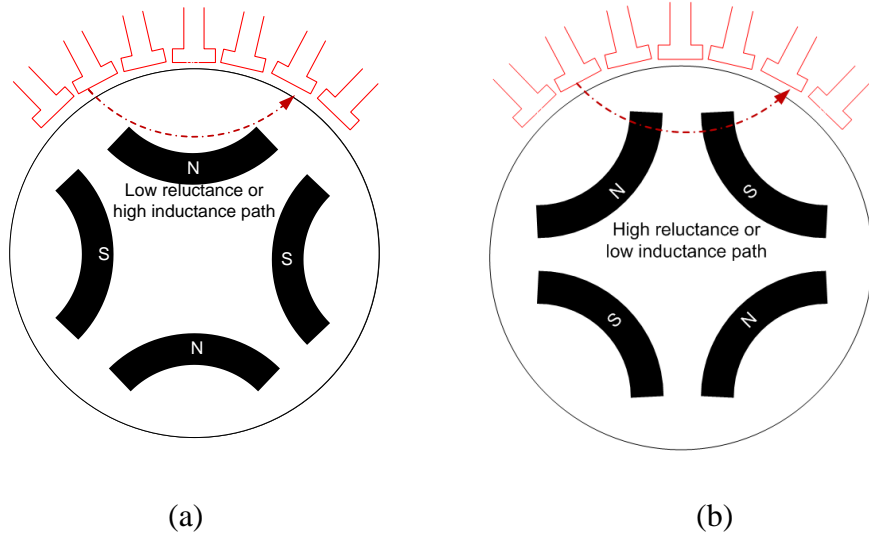


Figure 2-3: Flux path for IPM motors. (a) q -axis flux path has lower reluctance resulting in higher inductance. (b) d -axis path has higher reluctance that results in lower inductance

2.2. Three Phase Model

PMSMs can be simulated or analyzed based on the well-known model found in the literature [11][12][13]. Figure 2-4 shows the 3-phase model for the IPM. Phase inductance is considered to be a function of electrical rotor position θ since reluctance of the flux path changes with rotor position. According to [14], self-inductance of the machine can be expressed as a function of electrical rotor position as

$$L_a(\theta) = L_{ls} + L_{0s} - L_{2s}\cos(2\theta) \quad (2-1)$$

$$L_b(\theta) = L_{ls} + L_{0s} - L_{2s}\cos\left(2\theta + \frac{2\pi}{3}\right) \quad (2-2)$$

$$L_c(\theta) = L_{ls} + L_{0s} - L_{2s}\cos\left(2\theta - \frac{2\pi}{3}\right) \quad (2-3)$$

Mutual inductances between phases can be written as

$$M_{ab}(\theta) = -\frac{1}{2}L_{0s} - L_{2s}\cos(2\theta - \frac{2\pi}{3}) \quad (2-4)$$

$$M_{ac}(\theta) = -\frac{1}{2}L_{0s} - L_{2s}\cos(2\theta + \frac{2\pi}{3}) \quad (2-5)$$

$$M_{bc}(\theta) = -\frac{1}{2}L_{0s} - L_{2s}\cos(2\theta) \quad (2-6)$$

Flux produced by the permanent magnets can also be expressed as a function of rotor position [14][15]. Thus

$$\phi_a(\theta) = \Phi_m\cos(\theta) \quad (2-7)$$

$$\phi_b(\theta) = \Phi_m\cos(\theta - \frac{2\pi}{3}) \quad (2-8)$$

$$\phi_c(\theta) = \Phi_m\cos(\theta + \frac{2\pi}{3}) \quad (2-9)$$

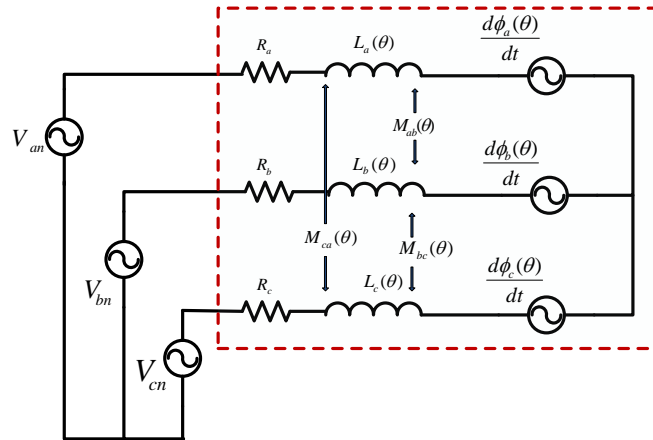


Figure 2-4: Three phase equivalent circuit for PMSM considering saliency.

According to [16], the motor equation can be directly written as Eqn. 2-10 where p denotes

$$\frac{d}{dt}$$

$$\begin{bmatrix} v_a \\ v_b \\ v_c \end{bmatrix} = \begin{bmatrix} R_a & 0 & 0 \\ 0 & R_b & 0 \\ 0 & 0 & R_c \end{bmatrix} \begin{bmatrix} i_a \\ i_b \\ i_c \end{bmatrix} + p \begin{bmatrix} L_a(\theta) & M_{ba}(\theta) & M_{ca}(\theta) \\ M_{ba}(\theta) & L_b(\theta) & M_{cb}(\theta) \\ M_{ca}(\theta) & M_{cb}(\theta) & L_c(\theta) \end{bmatrix} \begin{bmatrix} i_a \\ i_b \\ i_c \end{bmatrix} + \begin{bmatrix} \frac{d\phi_a(\theta)}{dt} \\ \frac{d\phi_b(\theta)}{dt} \\ \frac{d\phi_c(\theta)}{dt} \end{bmatrix} \quad (2-10)$$

2.3. Effects of Parameter Variation

According to [17] [18] [19], the permanent magnet flux linkage changes with temperature, making Back EMF voltage a function of temperature as well. Thus

$$\Phi_m(T) = \phi_{25}(1 - \alpha_\phi \Delta T) \quad (2-11)$$

where ϕ_{25} is the flux linkage at room temperature (25°C), α_ϕ is the reversible temperature coefficient of the magnetic material.

Stator resistance increases with temperature and can be expressed by a linear expression for a certain temperature range if the temperature coefficient of the material is known [17].

This gives the following expression for stator resistance

$$R(T) = R_{T_o}(1 + \alpha_R \Delta T) \quad (2-12)$$

here, R_{T_o} = resistance at known temperature T_o , and $\Delta T = T - T_o$ where T = operating temperature. α_R is the temperature coefficient of the material (copper).

Due to the core saturation, values of L_{ls} , L_{0s} , L_{2s} change with stator currents and can be considered as functions of stator currents [16]. Thus, inductances can be presented as functions of phase currents and rotor position.

$$L_a(i_a, i_b, i_c, \theta) = L_{ls}(i_a, i_b, i_c) + L_{0s}(i_a, i_b, i_c) - L_{2s}(i_a, i_b, i_c) \cos(2\theta) \quad (2-13)$$

$$L_b(i_a, i_b, i_c, \theta) = L_{ls}(i_a, i_b, i_c) + L_{0s}(i_a, i_b, i_c) - L_{2s}(i_a, i_b, i_c)\cos(2\theta + \frac{2\pi}{3}) \quad (2-14)$$

$$L_c(i_a, i_b, i_c, \theta) = L_{ls}(i_a, i_b, i_c) + L_{0s}(i_a, i_b, i_c) - L_{2s}(i_a, i_b, i_c)\cos(2\theta - \frac{2\pi}{3}) \quad (2-15)$$

The mutual inductances can be defined as

$$M_{ab}(i_a, i_b, i_c, \theta) = -\frac{1}{2}L_{0s}(i_a, i_b, i_c) - L_{2s}(i_a, i_b, i_c)\cos(2\theta - \frac{2\pi}{3}) \quad (2-16)$$

$$M_{ac}(i_a, i_b, i_c, \theta) = -\frac{1}{2}L_{0s}(i_a, i_b, i_c) - L_{2s}(i_a, i_b, i_c)\cos(2\theta + \frac{2\pi}{3}) \quad (2-17)$$

$$M_{bc}(i_a, i_b, i_c, \theta) = -\frac{1}{2}L_{0s}(i_a, i_b, i_c) - L_{2s}(i_a, i_b, i_c)\cos(2\theta) \quad (2-18)$$

A modified motor model considering all these variations can be expressed as shown in Figure 2-5.

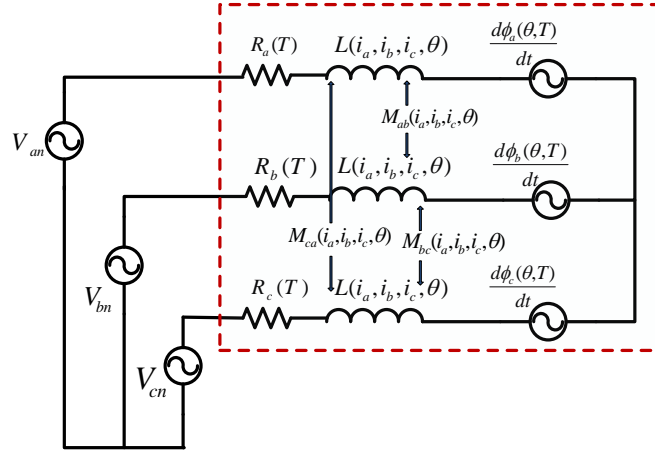


Figure 2-5: 3-phase equivalent circuit for PMSM considering saliency, magnetic saturation and temperature effects.

2.4. Vector Control Preliminaries

Three phase balanced voltages or currents can be represented as vectors comprised of magnitudes and phase angles as

$$F_{abc} = [F_a \ F_b \ F_c]^T = \left[F_M \cos(\theta) \quad F_M \cos\left(\theta - \frac{2\pi}{3}\right) \quad F_M \cos\left(\theta + \frac{2\pi}{3}\right) \right]^T \quad (2-19)$$

In a balanced 3-phase system, the summation of the three vectors is zero, which provides redundancy in the representation. It is sometimes convenient to represent 3-phase quantities in a stationary reference frame called $\alpha\beta$, where α and β are two perpendicular axes. It is sufficient to have projections of the three vectors on these perpendicular axes. Figure 2-6 shows the 3-phase vectors at a particular instant and the projections on the $\alpha\beta$ axes [20].

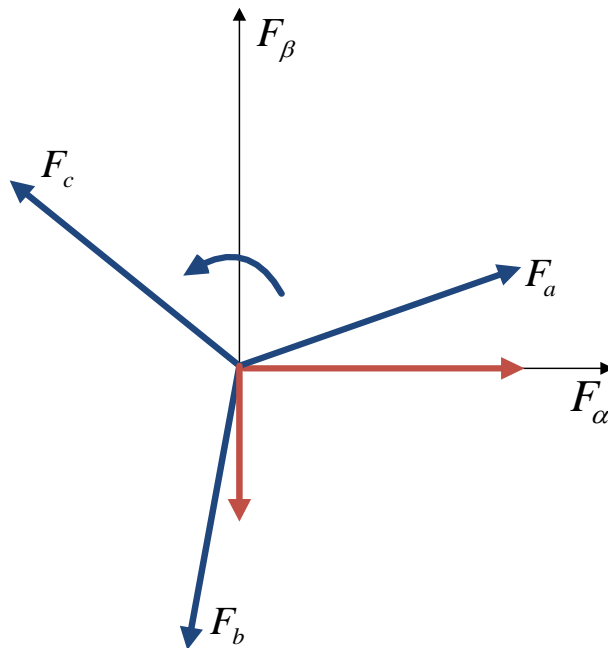


Figure 2-6: Three phase voltage and $\alpha\beta$ reference frame.

For transforming the 3-phase vectors into the 2-phase format, phase information of the 3-phase quantity is not required. By some simple trigonometric computations, it is possible to find a constant transformation matrix that transforms any vector in the abc reference frame into the stationary $\alpha\beta$ reference frame. Using trigonometric computation from Figure 2-6

$$F_\alpha = \frac{2}{3} [F_a \cos(0) \quad F_b \cos\left(-\frac{2\pi}{3}\right) \quad F_c \cos\left(\frac{2\pi}{3}\right)] \quad (2-20)$$

$$F_\beta = \frac{2}{3} [F_a \sin(0) \quad F_b \sin\left(-\frac{2\pi}{3}\right) \quad F_c \sin\left(\frac{2\pi}{3}\right)] \quad (2-21)$$

For symmetric balanced voltages

$$\begin{bmatrix} F_\alpha \\ F_\beta \end{bmatrix} = \frac{2}{3} \begin{bmatrix} \cos(0) & \cos\left(-\frac{2\pi}{3}\right) & \cos\left(\frac{2\pi}{3}\right) \\ \sin(0) & \sin\left(-\frac{2\pi}{3}\right) & \sin\left(\frac{2\pi}{3}\right) \end{bmatrix} \begin{bmatrix} F_a \\ F_b \\ F_c \end{bmatrix} \quad (2-22)$$

$$\begin{bmatrix} F_\alpha \\ F_\beta \end{bmatrix} = \frac{2}{3} \begin{bmatrix} 1 & -\frac{1}{2} & -\frac{1}{2} \\ 0 & \frac{\sqrt{3}}{2} & -\frac{\sqrt{3}}{2} \end{bmatrix} \begin{bmatrix} F_M \cos(\theta) \\ F_M \cos\left(\theta - \frac{2\pi}{3}\right) \\ F_M \cos\left(\theta + \frac{2\pi}{3}\right) \end{bmatrix} \quad (2-23)$$

Simplifying, we get

$$\begin{bmatrix} F_\alpha \\ F_\beta \end{bmatrix} = \begin{bmatrix} F_M \cos(\theta) \\ F_M \sin(\theta) \end{bmatrix} \quad (2-24)$$

This transformation gives us vectors rotating at the same frequency as the original 3-phase vectors. Instead of keeping the reference frame stationary, if the axes are rotated at the same frequency with the 3-phase vectors, projections of the 3-phase vectors on those rotating axes will become constant. Thus, 3-phase AC quantities will eventually be

converted into two DC quantities. This transformation is called the *abc* to *dq* transformation. Moreover, if the axes for taking the projections are such that, one of them is locked with the phase ‘a’ of the 3-phase vectors, summation of projections will be zero in the other perpendicular axis. That means if the *d* – axis is locked with phase ‘a’, quantities at *q*-axis will always be zero since F_b and F_c will cancel each other along *q* – axis. The concept can be seen using the following representation

$$\begin{bmatrix} F_d \\ F_q \end{bmatrix} = \begin{bmatrix} \cos(\theta) & \sin(\theta) \\ -\sin(\theta) & \cos(\theta) \end{bmatrix} \begin{bmatrix} F_\alpha \\ F_\beta \end{bmatrix} \quad (2-25)$$

$$\begin{bmatrix} F_d \\ F_q \end{bmatrix} = \begin{bmatrix} \cos(\theta) & \sin(\theta) \\ -\sin(\theta) & \cos(\theta) \end{bmatrix} \begin{bmatrix} F_M \cos(\theta) \\ F_M \sin(\theta) \end{bmatrix} \quad (2-26)$$

Simplifying, we get

$$\begin{bmatrix} F_d \\ F_q \end{bmatrix} = \begin{bmatrix} F_M \\ 0 \end{bmatrix} \quad (2-27)$$

Here, F_d and F_q are projections of the vectors along the ‘direct’ and ‘quadrature’ axes respectively. The θ used in the conversion is taken as the measured rotor position. The new reference frame that the stator quantities are converted to is called the rotor reference frame. The *q*-axis is aligned with mechanical placement of the magnets such that permanent magnet flux is zero along the *q*-axis. The *dq* motor model in rotor reference frame converts stator currents, back EMF voltages and applied voltages into DC quantities making the controller simpler. Moreover, generated torque in the motor also becomes a simple function of currents along *d* and *q* axes.

2.5. Motor Model in dq Reference Frame

The transformation from the abc reference frame to the dq reference frame is a well-known transformation in the field of motor control and is known as the Park transformation [21]. Applying the Park transformation in the 3-phase PMSM model provides us with the dq motor model in the rotor reference frame as shown in Figure 2-7 [12] [22][23].

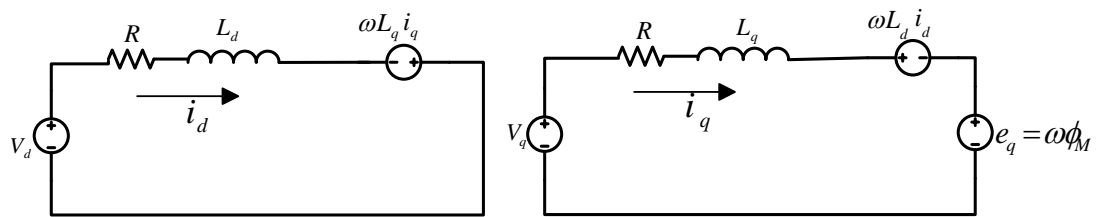


Figure 2-7: dq PMSM model in rotor reference frame.

Here,

L_d = Inductance along direct axis

L_q = Inductance along quadrature axis

v_d = d – axis applied voltage

v_q = q – axis applied voltage

i_d = d – axis stator current

i_q = q – axis stator current

ω = Electrical angular velocity

$\omega = P\omega_m$ [ω_m = mechanical speed, P = number of pole pairs]

ϕ_M = Permanent magnet flux linkage

e_q = Back EMF voltage along q axis

R = Stator winding resistance

The model shown in Figure 2-7 provides simple equations for computing the voltage-current relationship at different speeds. Using the dq motor model in the rotor reference frame, we get

$$\begin{bmatrix} v_q \\ v_d \end{bmatrix} = \begin{bmatrix} R + L_q \frac{d}{dt} & \omega L_d \\ -\omega L_q & R + L_d \frac{d}{dt} \end{bmatrix} \begin{bmatrix} i_q \\ i_d \end{bmatrix} + \begin{bmatrix} \omega \phi_M \\ 0 \end{bmatrix} \quad (2-28)$$

Produced torque can be expressed as

$$T_e = \frac{3}{2} P [\phi_M + (L_d - L_q) i_d] i_q \quad (2-29)$$

2.6. Parameter Variations in dq Reference Frame

As described in Section 2.3, motor parameters in PMSM exhibit significant deviations over the nominal operating region of a motor. Core saturation due to stator currents deviates motor inductances, but experimental results suggest L_d , L_q are functions of quadrature axis current i_q [24][25][18]. L_d suffers a small droop whereas droop of L_q is a non-linear function of i_q that affects the performance significantly [24]. The PMSM model in the dq reference frame should be modified to accommodate parameter variations due to stator

currents or changes in temperature, to be able to simulate the experimental motor accurately. Figure 2-8 shows the modified dq motor model including the deviations caused by stator currents and temperature.

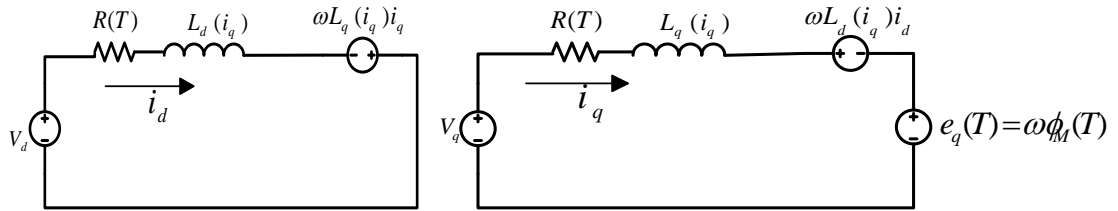


Figure 2-8: dq PMSM model in rotor reference frame considering saturation and temperature effects.

To introduce inductance droop and temperature effects, the torque equation can be represented using the following format

$$T_e = \frac{3}{2} P \left[\phi_M(T) + (L_d(i_q) - L_q(i_q)) i_d \right] i_q \quad (2-30)$$

here, $L_d(i_q)$ and $L_q(i_q)$ are both functions of quadrature axis current i_q .

CHAPTER III

LITERATURE REVIEW

3.1. Maximum Torque per Ampere Definition

The torque production in an IPM is a function of ϕ_M , i_d , $i_q L_d$ and L_q as described in Eqn. 2-30. There are an infinite number of i_q and i_d combinations which can produce the same amount of torque. Introducing the inductance droop even complicates i_q and i_d selection further.

The torque produced by any IPM can be split into two components. The component arising from the permanent magnet flux is called reactance torque or magnetic torque and expressed by

$$T_{magnetic} = \frac{3}{2} P \phi_M i_q \quad (3-1)$$

The other component arising from rotor saliency can be called reluctance torque and expressed by

$$T_{reluctance} = \frac{3}{2} P (L_d - L_q) i_d i_q \quad (3-2)$$

Since permanent magnets have higher reluctance or lower permeability than iron, inductance along the d -axis is usually lower than that along the q -axis [26]. Thus, for conventional IPMs, L_d is smaller than L_q . This in turns necessitates introduction of negative i_d in order to produce any positive torque.

Figure 3-1 shows the variation required in i_q for different i_d in producing a particular amount of torque. A constant parameter motor model was considered to avoid complexity. Negative i_d reduces the required amount of i_q by aiding in the reluctance torque generation. Figure 3-2 shows the amount of torque produced by ϕ_M and i_q which is essentially directly proportional to the magnitude of i_q . Figure 3-3 shows the contribution of reluctance torque arising from i_d . Since a positive value of direct axis current is opposing the magnetic torque, a positive i_d is never desired. As shown in Figure 3-4, for any torque level, there exists a particular i_q, i_d pair that causes minimum phase currents. Since resistive loss in the stator solely depends on phase current magnitudes, it is always preferred to operate the motor as close as possible to these i_q, i_d pairs. Since it is similar to maximizing the torque output for a particular amount of current, the operation scheme is called Maximum Torque per Ampere (MTPA).

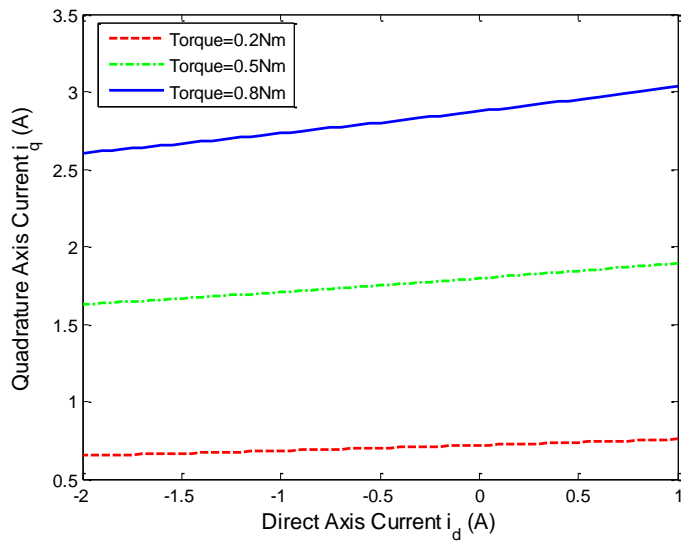


Figure 3-1: Variation in required i_q for different i_d values. Negative i_d produces more reluctance torque reducing the requirement for the i_q magnitude.

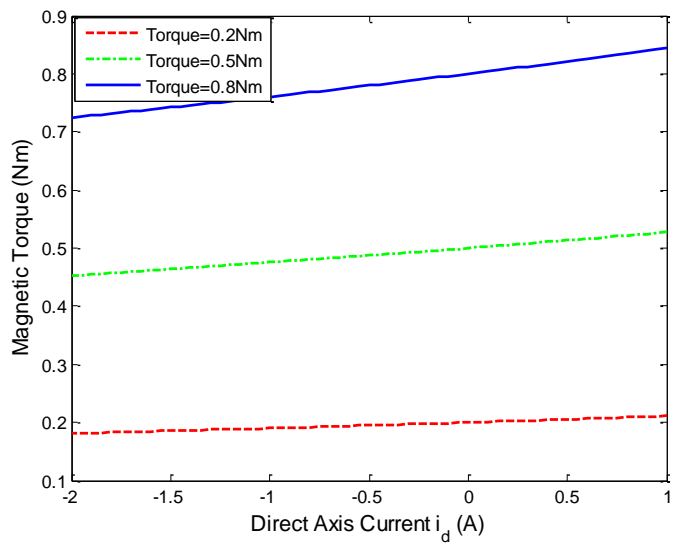


Figure 3-2: Magnetic torque produced by i_q ; the torque output is directly proportional to i_q and only parameter dependence occurs if there is any change in permanent magnet flux.

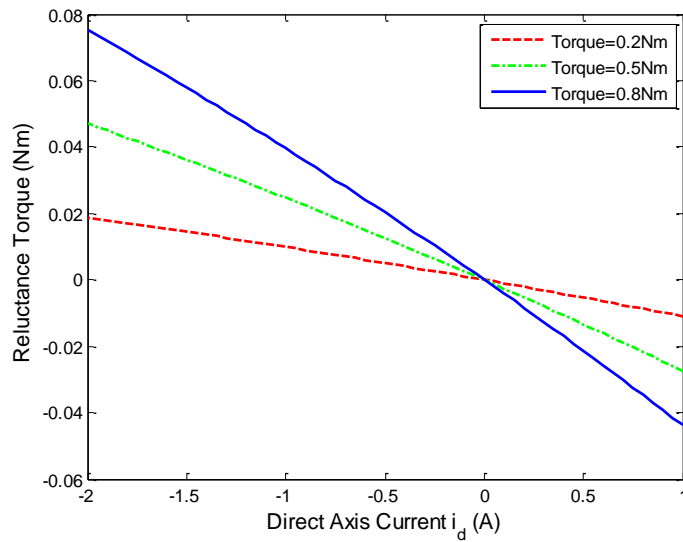


Figure 3-3: Reluctance torque variation with i_d ; positive i_d creates negative reluctance torque which eliminates any positive desired value for i_d .

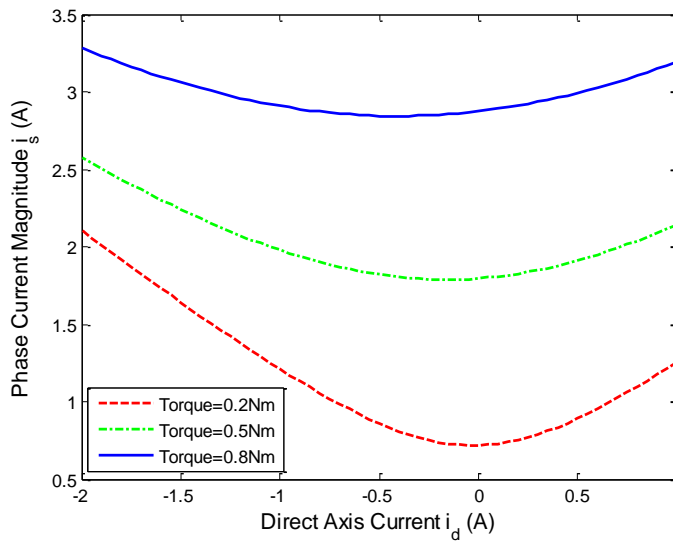


Figure 3-4: Phase current magnitudes for different i_d values; point of minimum phase current varies for different torque level.

The concept of MTPA can be better realized from closer observation of Figure 3-5. The MTPA line shows the i_d, i_q pairs which produce desired torque with the minimum possible current magnitudes. The concave curves show the constant torque lines indicating all the

i_d, i_q pairs falling on those lines produce the same amount of torque. But as discussed earlier, there exists only one particular i_d, i_q pair that produces desired torque with minimum current magnitude. These desired pairs are the points where constant torque lines intersect with MTPA line. The dotted quarter circle represents the maximum allowed current limit for the particular motor.

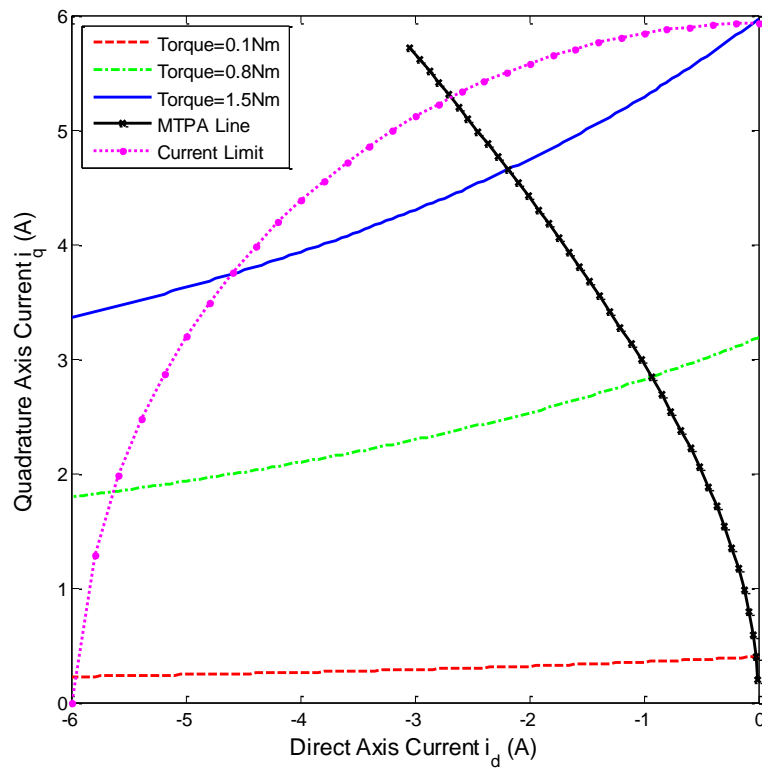


Figure 3-5: i_d, i_q lines for generating desired torques; intersections of the constant torque lines and MTPA line represent the optimum i_d, i_q pairs for generating corresponding torques. The dotted quarter circle shows the current limit for a particular motor.

3.2. Previous work on MTPA

Developing a control strategy for MTPA operation has drawn considerable attention and various solutions have been proposed so far. Early researchers proposed techniques based on constant parameter motor models which fail to give satisfactory performance over the entire operating region. Later, control schemes considering magnetic saturation and temperature effects were proposed. With the advancement in processing power of DSP controllers, more computation intensive algorithms have been proposed in recent years. Based on their operational strategies, proposed control schemes can be roughly grouped into two main categories;

- i) A-priori methods (Based on premade tables, polynomials or solution of equations based on motor model and parameters),
- ii) Methods based on a search algorithm.

3.2.1. A-Priori Methods

Most of the control strategies proposed so far use premade tables, estimation polynomials or utilize equations to compute MTPA operating points. Two major techniques implementing a-priori methods are observed in the literature as

- i) Control schemes based on the solution of the biquadratic equation (Methods that directly compute i_d, i_q at a given condition),

- ii) Control schemes based on i_d, i_q relationships at MTPA (i_q is computed through Proportional Integral (PI) controller, i_d as a function of i_q , speed and other parameters).

3.2.1.1. Control Schemes Based on Biquadratic Torque Equation

As explained in Section 3.1, maximizing the torque equation subject to $i_q^2 + i_d^2$ gives necessary i_q, i_d pairs for the MTPA trajectory for a particular motor. Several methods have been proposed based on the solution of the biquadratic equation obtained by differentiating the torque equation with respect to stator current magnitudes [4][27][28][29][30][31]. Since it is computationally intensive to solve the equation in real time, most of the work in the literature proposed using pre-computed look up tables or estimation polynomials. Offline optimization is performed and either stored in the look up tables or curve fit into equations.

Jahns, Kliman and Neumann proposed computing the i_d, i_q as a function of normalized torque in [27]. Current components are computed without considering the effects of the magnetic saturation. At higher current levels, magnetic saturation reduces the flux at the air gap and quadrature axis inductance L_q significantly. The nonlinear saturation along with rotor saliency makes it complicated to find optimum i_d, i_q pairs at high current.

A control strategy using the derivative of the torque equation based on constant motor parameters was proposed in [4]. Since the proposed method requires solving a fourth order equation, an offline solution was proposed using the least square estimation method. The proposed least square estimation method provides the current reference as a second order

function of the quantity called ‘virtual control’ which is a scaled version of the required torque.

Authors in [28] proposed using real time implementation of the biquadratic equation solution method based on a constant parameter motor model with a systematic approach proposed by Lodovico Ferrari [29]. The method provides a solution for the reference current instead of using an iterative search which made it possible to be adopted for online implementation. A recursive method was also proposed in [28] to incorporate inductance variation due to core saturation.

Kim, Hartwig and Lorenz proposed offline parameter estimation and a-priori computed an MTPA locus in [30], where the offline estimator is used to produce the MTPA trajectory considering parameter variations. The computed trajectory was different from the one obtained using the constant parameter model; especially at higher current regions. The method also proposed online estimation of motor inductances which were only used to generate a reference voltage for current regulation.

A lookup table based solution was proposed in [31] that considers the effects of the temperature variation as well. Kim and Sul proposed generating of two 2-D lookup tables for two different permanent magnet flux linkage conditions ϕ_{M1} and ϕ_{M2} . A flux observer was proposed to estimate permanent magnet flux linkage $\hat{\phi}_M$. Final reference currents were computed by performing interpolation between values found from pre-computed lookup tables for ϕ_{M1} and ϕ_{M2} and estimated flux linkage $\hat{\phi}_M$.

3.2.1.2. Control Schemes Based on i_d, i_q Relationship at MTPA

Instead of finding i_d, i_q using polynomials or look up tables, several researchers proposed using the i_q, i_d relationship for MTPA. In these methods, only i_d was generated as functions of i_q , speed and other parameters. A PI controller or some other means were used to generate an i_q reference.

Morimoto, et al, proposed computing the required i_d based on equations found by differentiating the torque expression with respect to current magnitude[32]. This gave following straight forward relationship between i_d and i_q

$$i_d = \frac{\phi_M}{2(L_d - L_q)} - \sqrt{\frac{\phi_M^2}{4(L_q - L_d)^2} + i_q^2} \quad (3-3)$$

i_d can be represented by the stator current i_s

$$i_d = \frac{\phi_M}{4(L_d - L_q)} - \sqrt{\frac{\phi_M^2}{16(L_q - L_d)^2} + \frac{i_s^2}{2}} \quad (3-4)$$

$$\text{where } i_s = \sqrt{i_q^2 + i_d^2}. \quad (3-5)$$

In the proposed algorithm, a PI speed controller was used to generate the necessary i_q based on the operating conditions. The required i_d for MTPA operation was generated using Eqn. 3-3. Introduction of the computed i_d changes the operating point while the PI controller adjusts the i_q reference that in turns produces a new i_d reference. The procedure ultimately converges to a suitable i_d, i_q pair. An almost similar technique was proposed by the same

authors in [33] which considers L_q as a function of i_q to compensate for magnetic saturation.

Authors in [24] [25] on the other hand, proposed computing i_d based on saturation and the cross coupling effect using a Lagrange multiplier [34] approach. The expression for i_d is given by

$$i_d = -\frac{I_{do} \left[\left(\frac{dL_{md}(i_{qs})}{di_{qs}} \right) i_{qs} + L_{md}(i_{qs}) \right]}{2\Delta} - \sqrt{\frac{I_{do}^2 \left[\left(\frac{dL_{md}(i_{qs})}{di_{qs}} \right) i_{qs} \right]^2}{4\Delta^2} + \frac{(L_d(i_{qs}) - L_q(i_{qs})) i_{qs}^2}{\Delta}} \quad (3-6)$$

$$\text{where } \Delta = \left\{ \left[\frac{d(L_{md}(i_{qs}) - L_{mq}(i_{qs}))}{di_{qs}} \right] i_{qs} + L_d(i_{qs}) - L_q(i_{qs}) \right\}$$

In both methods, inductances were considered to be functions of quadrature axis current as suggested in most of the literature.

Niazi, Toliyat et al, proposed online estimation of L_d, L_q and utilized the estimated parameters while computing the reference currents [10]. A steady state motor model was used for parameter estimation. This method was proposed for permanent magnet assisted synchronous reluctance motors (PMSynRM) that has a similar torque equation as IPMs. The i_d, i_q relationship mentioned in Eqn. 3-3 provides another convenient form of solution based on current phase angle β in a straight forward manner [35].

$$\beta = \sin^{-1} \left(\frac{-\phi_M + \sqrt{\phi_M^2 + 8(L_d - L_q^2)i_s^2}}{4(L_d - L_q)i_s} \right) \quad (3-7)$$

$$\text{where } i_d = -i_s \sin(\beta) \quad i_q = i_s \cos(\beta) \quad (3-8)$$

Equation 3-7 was used with the estimated L_d, L_q along with some perturbation technique for maximizing torque generation. An almost similar strategy was also proposed in [36], but modifications were made in the parameter estimation technique. An affine projection algorithm [37] was proposed for parameter estimation which required fewer computations compared to Recursive Least Square or Kalman filtering techniques.

Kang, Lim et al. proposed a method based on offline training of the motor at constant temperature to develop a lookup table of reference current magnitudes and phase angles for operating at MTPA [38]. The novelty of the method was mostly on adding the temperature compensation considering the weakening of permanent magnets at high temperature. A reverse lookup table was used for torque estimation in the proposed method. The magnetic flux linkage was modeled using the reversible temperature coefficient of the permanent magnet material.

Modeling i_d as a function of i_q and speed was proposed in [39] by Mademlis, Kioskeridis, et al. Instead of using the equation based on MTPA, a loss modeling control (LMC) was proposed. The control scheme proposes determination of optimum i_d using a predetermined polynomial of speed and i_q .

3.2.2. Methods Based on Search Algorithm

Another well known technique involves using some online search algorithm for achieving MTPA operation. The benefit of using such an approach is to get lower parameter dependence. Even an ill-defined motor model can give satisfactory performance because of lower dependence on the motor model. The downside of these algorithms is poor performance during transients. Most of the search algorithms rely on some means of perturb and observe method which takes time to converge to a desired operating point. Moreover, Mademlis, Kioskeridis et al demanded that, algorithms based on searching sometimes fail to attain a desired state and cause undesirable torque disturbance [39].

Among different search based algorithms proposed for PM motors, Colby and Novotny proposed a technique in [40] which only requires DC link current measurement. Instead of going into the dq reference frame, a method was proposed which implements the control in the 3-phase abc reference frame. In the proposed method, DC link current is used to generate an optimum voltage reference to minimize losses.

Zhu, Chen and Howe in [5] proposed searching for optimum i_d, i_q by monitoring the real time performance of the motor. The amount of i_d is controlled by measuring the error between the actual and the reference current in the flux weakening region. During MTPA operation, the i_d command is generated by observing the current phasor magnitude or from DC link current measurement. While the speed remains constant, a change in the DC link current is used to determine the performance of the machine and adjust the i_d command.

On the other hand, authors in [9] and [41] proposed an online tracking method to determine optimum current phase angle β for MTPA operation. Anton, Kwan et al in [9] proposed

estimation of β by a perturb and observe method to minimize the magnitude of the stator current. At MTPA point, β would be oscillating around its optimum value. The proposed technique performs well at steady state but would fail during rapid load and speed command changes. Kim, Yoon, et al in [41] proposed a method that would bring the $\frac{\delta T}{\delta \beta}$ to zero at MTPA point through high frequency current injection.

Bolognani et al proposed a hybrid controller which uses pre-computed current phase angle β for MTPA operation using a constant parameter motor model [42]. A new reference frame was proposed called the MTPA reference frame which is essentially the dq reference frame shifted by the current phasor angle β . The phase shifting of the reference frame caused only $i_{\hat{q}}$ to produce torque. An algorithm to modify pre-computed β was only introduced at steady state as a compensation for parameter variation.

CHAPTER IV

PROPOSED CONTROL SCHEME

In this chapter, a hybrid control scheme is proposed that utilizes both a-priori system information as well as a search based technique for MTPA operation of the IPMs. Though the proposed scheme operates entirely in the 3-phase domain, analysis will be done in the dq reference frame for easier understanding. In the first part of the chapter, a preliminary block diagram will be presented to provide necessary understanding of the analytical approach. Analytical explanation will be given later to prove the validity of the proposed control algorithm.

4.1. Experimental and Simulation Motor Parameters

The algorithm was developed particularly for a buried magnet PMSM or IPM motor which exhibits rotor saliency but it is still applicable for SPM motors by keeping $i_d = 0$. A 1.5 HP Kollmorgen Goldline Servomotor was chosen for developing simulation models and implementing the proposed algorithm in both simulations and experiments. Motor parameters for the experimental motor are provided in Table 4-1.

Table 4-1 : Experimental motor parameters

Parameter	Value	Unit
DC Resistance (at 25°C) (Line to Neutral)	1.375	Ω
d axis inductance L_d	4.55	mH
q axis inductance L_q	9.375	mH
Flux linkage ϕ_M	0.0928	V/rad/sec (electrical angular velocity)
Number of pole pairs P	2	
Maximum Line current i_{max} (RMS)	4.2	A

The non-idealities measured from the experimental motor are incorporated into the simulation model.

4.2. Preliminary Block Diagram

The proposed control scheme is particularly designed for speed control of a PMSM drive system. A generalized block diagram for a conventional motor control scheme is shown in Figure 4-1. A PI controller is used to generate the necessary reference torque to attain commanded speed. The steady state value of this reference torque depends on the effective load torque and losses in the drive system. A suitable technique is used to generate a current reference that produces the required torque with the minimum possible current magnitude. This block may vary depending on the algorithm adopted and may require different

feedback signals to operate. The following block preceded by the dq to abc transformation block is responsible for ensuring the motor to operate at the desired state. This block generates required voltage references v_d and v_q for the motor to operate at the commanded current. Figure 4-2 shows a typical block diagram to produce reference voltages to be applied to the motor. Generated voltages at the dq reference frame are thus converted into the abc reference frame and sent to the control block responsible for applying that voltage at the motor terminals using a 3-phase inverter.

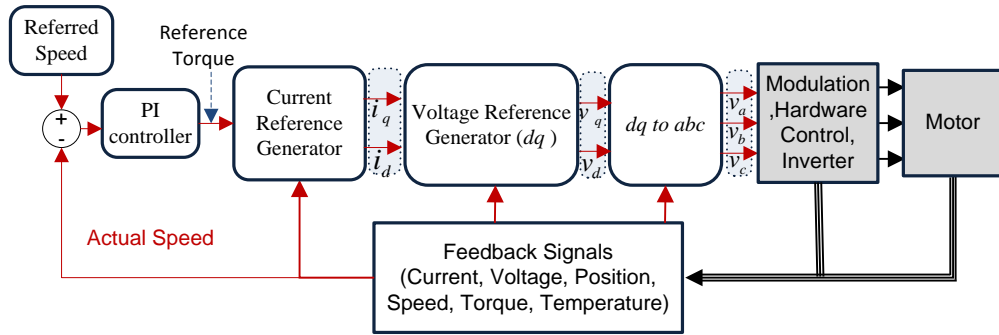


Figure 4-1: Basic block diagram for a conventional control scheme.

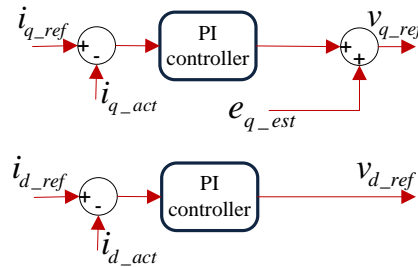


Figure 4-2: Inside look of a typical voltage reference generator block

Since the motor model is developed in the rotor reference frame, ensuring the total back EMF voltage to be along q axis, ($e_d = 0$), the i_q component of the current is aligned with the back EMF voltage. Hence, i_q, i_d can be represented by a current magnitude i_s and phase

difference with back EMF β according to Eqn. 3-7. Since i_d is always desired to be negative, the current phasor in a PMSM is either in phase (for $i_d = 0$) or leading (for $i_d < 0$) the back EMF voltage.

The constant parameter model of an IPM holds the following equations at steady state

$$\begin{bmatrix} v_q \\ v_d \end{bmatrix} = \begin{bmatrix} R & \omega L_d \\ -\omega L_q & R \end{bmatrix} \begin{bmatrix} i_q \\ i_d \end{bmatrix} + \begin{bmatrix} \omega \phi_M \\ 0 \end{bmatrix} \quad (4-1)$$

This model gives the following values for v_q and v_d

$$v_q = R i_q + \omega L_d i_d + \omega \phi_M \quad (4-2)$$

$$v_d = -\omega L_q i_q + R i_d \quad (4-3)$$

Since i_d is either negative or zero, it is evident that v_d is always negative whereas v_q is always positive. If the voltage phase advance angle δ is defined as the angle between back EMF and voltages at the inverter output, then v_d, v_q can be represented using voltage magnitude v_m and phase advance angle δ . Hence

$$v_m = \sqrt{v_d^2 + v_q^2} \quad (4-4)$$

$$\text{where, } v_q = v_m \cos(\delta) \quad v_d = -v_m \sin(\delta)$$

Regardless of the control scheme used for generating i_q, i_d pairs, it is the final voltage vector that must be computed and applied at the motor terminals. The entire procedure consists three main steps

- i) Finding required torque to achieve reference speed using a PI controller
- ii) Finding i_d, i_q or i_s, β that produces referred torque with minimum possible phase current (MTPA)

- iii) Finding v_d, v_q or v_m, δ that regulates the motor phase current at the commanded level.

Since motor parameters behave in a predictable manner for a particular motor, it seems legitimate to find v_d, v_q or v_m, δ directly from the speed reference at a particular loading condition. Figure 4-3 shows the preliminary block diagram for the proposed control scheme. A simple PI controller is used to generate the voltage magnitude v_m whereas a control block is dedicated for creating a phase advance angle δ that causes the motor to operate at the MTPA condition. The PI controller can be designed using any straight forward technique and has a wide stability region. The challenging part is to design a block that generates δ considering all the non-idealities of the motor.

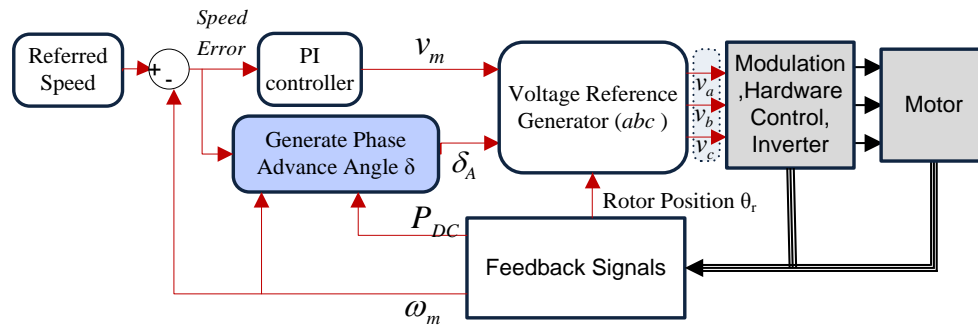


Figure 4-3: Preliminary block diagram for the proposed control scheme.

Another noticeable fact in the control mechanism is that, the magnitude of the voltage phasor v_m also depends on the value of δ . But whatever the value of δ , the speed controller loop would automatically adjust the v_m to keep the motor at the commanded speed.

4.3. Analytical Background

For the analysis of an IPM avoiding complex computations, it is better to use a constant parameter model. Thus, the system will be analyzed using a constant parameter model without considering magnetic saturation and temperature effects. Non-idealities will be introduced using a numerical approach in the later part of the chapter.

Representing the voltage vectors in phasor format, the following equations are found at steady state

$$\begin{bmatrix} v_m \cos(\delta) \\ -v_m \sin(\delta) \end{bmatrix} = \begin{bmatrix} R & \omega L_d \\ -\omega L_q & R \end{bmatrix} \begin{bmatrix} i_q \\ i_d \end{bmatrix} + \begin{bmatrix} \omega \phi_M \\ 0 \end{bmatrix} \quad (4-5)$$

The phase current vector can be defined as

$$\begin{bmatrix} i_q \\ i_d \end{bmatrix} = \frac{1}{R^2 + \omega^2 L_q L_d} \begin{bmatrix} R & -\omega L_d \\ \omega L_q & R \end{bmatrix} \begin{bmatrix} v_m \cos(\delta) - \omega \phi_M \\ -v_m \sin(\delta) \end{bmatrix} \quad (4-6)$$

i_q, i_d values can be represented as

$$i_q = \frac{1}{R^2 + \omega^2 L_q L_d} (R v_m \cos(\delta) - \omega R \phi_M + \omega L_d v_m \sin(\delta)) \quad (4-7)$$

$$i_d = \frac{1}{R^2 + \omega^2 L_q L_d} (-R v_m \sin(\delta) - \omega^2 L_q \phi_M + \omega L_q v_m \cos(\delta)) \quad (4-8)$$

As mentioned earlier, the PI controller is designed such a way that it will operate the motor at the designated speed regardless of the chosen value of δ . If the total load torque is

assumed constant (comprising load torque and viscous damping), the following equation is valid for the current components

$$T_L = (k_1 + k_2 i_d) i_q \quad (4-9)$$

$$\text{here } k_1 = \frac{3}{2} P \phi_M, \quad k_2 = \frac{3}{2} P (L_d - L_q)$$

and, $T_L = T_{load} + B_c \omega_M$ (B_c = viscous damping, ω_M = mechanical speed).

Putting the values of i_q, i_d in the torque equation, we get

$$T_L = [k_1 + \frac{k_2}{Z^2} (-R v_m \sin(\delta) - \omega^2 L_q \phi_M + \omega L_q v_m \cos(\delta))] \frac{1}{Z^2} (R v_m \cos(\delta) - \omega R \phi_M + \omega L_d v_m \sin(\delta)) \quad (4-10)$$

$$\text{where } \frac{1}{Z^2} = \frac{1}{R^2 + \omega^2 L_q L_d}.$$

After going through algebraic manipulations, the following equation is obtained

$$\begin{aligned} & v_m \cos(\delta) [k_3 R - 2k_2 R \omega^2 L_d \phi_M] \\ & - v_m \sin(\delta) [-k_3 \omega L_q - k_2 \omega \phi_M R^2 + k_2 \omega^3 \phi_M L_q L_d] \\ & - v_m^2 \sin^2(\delta) [k_2 R \omega L_d] + v_m^2 \cos^2(\delta) [k_2 \omega L_q R] \\ & - v_m^2 \cos(\delta) \sin(\delta) [k_2 R^2 - k_2 \omega^2 L_d L_q] \\ & + [-k_3 \omega R \phi_M + k_2 \omega^3 R \phi_M L_d - T_L Z^4] = 0 \end{aligned} \quad (4-11)$$

$$\text{here, } k_3 = k_1 Z^2$$

Putting some arbitrary value of δ will provide a quadratic equation for v_m . Solution of the quadratic equation would give the necessary voltage to operate at the desired speed ω_M (Mechanical) or ω (Electrical). The final quadratic equation has the following form

$$Av_m^2 + Bv_m + C = 0 \quad (4-12)$$

where

$$\begin{aligned} A &= -\sin^2(\delta) [k_2 R \omega L_d] + \cos^2(\delta) [k_2 \omega L_q R] - \cos(\delta) \sin(\delta) [k_2 R^2 - k_2 \omega^2 L_d L_q] \\ B &= \cos(\delta) [k_3 R - 2k_2 R \omega^2 L_d \phi_M] - \sin(\delta) [-k_3 \omega L_q - k_2 \omega \phi_M R^2 + k_2 \omega^3 \phi_M L_q L_d] \\ C &= [-k_3 \omega R \phi_M + k_2 \omega^3 R \phi_M L_d - T_L Z^4] \end{aligned} \quad (4-13)$$

Solution of the quadratic equation provides the desired voltage magnitude v_m . Hence

$$v_m = \frac{-B + \sqrt{B^2 - 4AC}}{2A} \quad (4-14)$$

Putting the value of v_m obtained using Eqn. 4-14 into Eqn.4-7 and 4-8 will provide the operating i_q, i_d . It is obvious that there exists an optimum value for phase advance angle δ that will result in minimum stator current. Optimum δ can be evaluated by solving for δ considering $\frac{\partial i_s}{\partial \delta} = 0$, but the analytical expression for i_s becomes complicated for performing the partial derivative. Thus a numerical approach was taken.

Figure 4-4 shows the variation in current magnitude with respect to δ for different torque levels. The curves were generated considering the ideal motor model operating at 800 RPM. Required values of voltage magnitudes for corresponding δ are plotted in Figure

4-5. As mentioned earlier, since a PI controller is dedicated for generating required voltage to attain commanded speed, whatever the value of δ , the corresponding voltage will be automatically generated by the PI controller. The points marked by ∇ in the curves represent the points of optimum δ s. Figure 4-6 and Figure 4-7 show the current variations and required voltage variation with the change in δ for different operating speeds at 0.4 Nm load. Close observation of the point of minimum current reveals that, the phase advance angle responsible for MTPA follows a certain pattern that can be predicted. Hence, the proposed control scheme was designed in such a way that the optimum δ was computed based on the operating conditions.

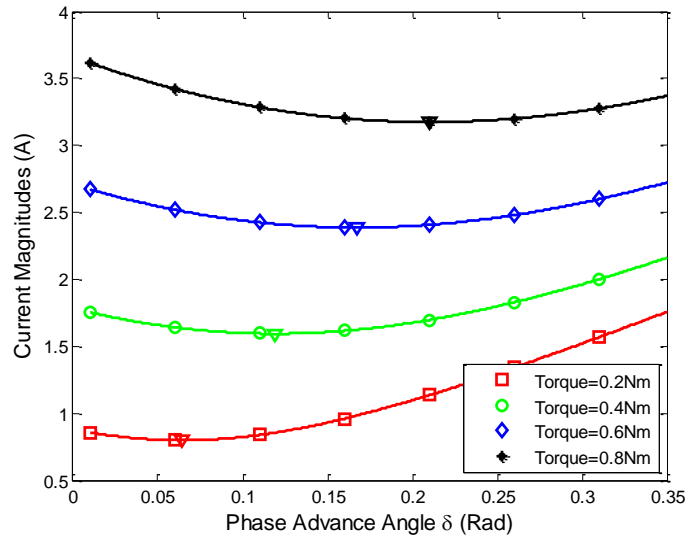


Figure 4-4: Current magnitudes with change in phase advance angle δ at different load torque levels. Curves were generated considering the ideal motor model operating at 800 RPM. The locations marked by ∇ represent the minimum possible current magnitudes.

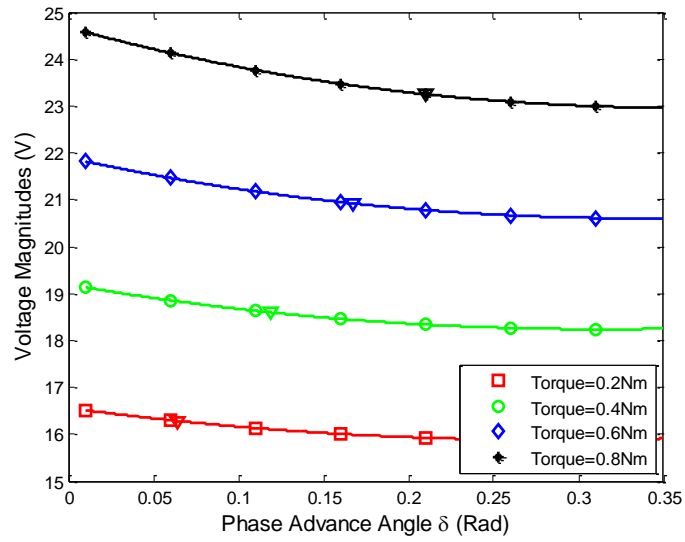


Figure 4-5: Required voltage magnitudes with change in phase advance angle δ at different load torque levels. (Optimum phase advance angles are marked by ∇).

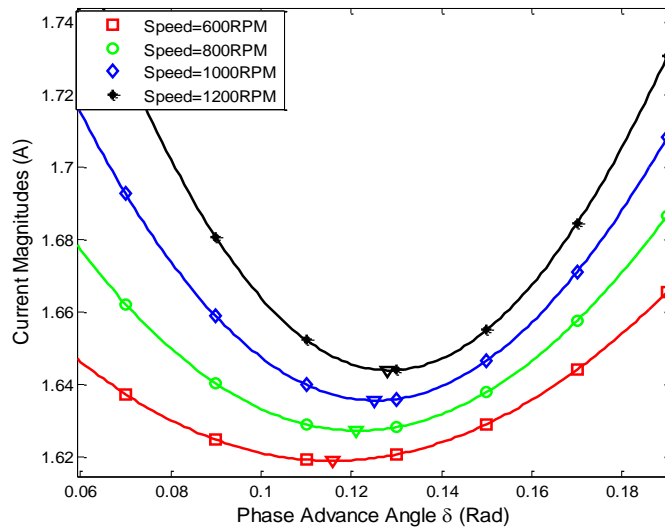


Figure 4-6: Current magnitudes with change in phase advance angle δ at different speeds. Curves were generated considering ideal motor model operating at 0.4 Nm load torque and small viscous damping. The locations marked by ∇ represent the minimum possible current magnitudes.

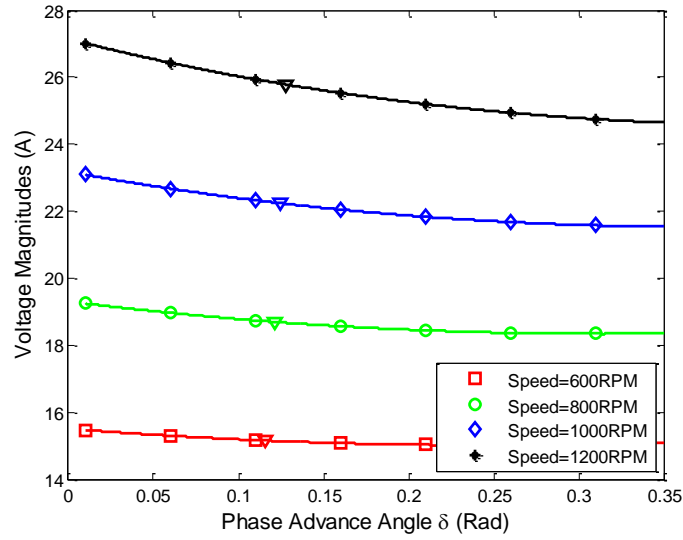


Figure 4-7: Required voltage magnitudes with change in phase advance angle δ at different speeds and 0.4Nm load torque with some viscous damping. (Optimum phase advance angles are marked by ∇).

4.4. Phase Advance Angle Based on Ideal Motor Model

Combining Eqn. 4-7 and 4-8 with the solution for v_m from Eqn. 4-14 gives the exact magnitude of the current phasor for the corresponding δ . The current magnitude for a particular load torque condition and speed can be presented as

$$i_s = \frac{1}{R^2 + \omega^2 L_q L_d} \sqrt{\left(\frac{-B + \sqrt{B^2 - 4AC}}{2A} R \cos(\delta) - \omega R \phi_M + \omega L_d \frac{-B + \sqrt{B^2 - 4AC}}{2A} \sin(\delta) \right)^2 + \left(-R \frac{-B + \sqrt{B^2 - 4AC}}{2A} \sin(\delta) - \omega^2 L_q \phi_M + \omega L_q \frac{-B + \sqrt{B^2 - 4AC}}{2A} \cos(\delta) \right)^2} \quad (4-15)$$

where values of A, B, C can be found in Eqn.4-13.

Equation 4-15 states that the magnitude of i_s is a function of phase advance angle, load torque, operating speed, and all motor parameters. The optimum phase advance angle is

found by considering $\frac{\partial i_s}{\partial \delta} = 0$ and is also a function of motor parameters and operating condition. In a short form, it can be expressed as

$$\delta_{opt} = F(T_L, \omega, R, L_d, L_q, \phi_M) \quad (4-16)$$

Numerically obtained loci of δ_{opt} are plotted in Figure 4-8 for three different speeds. Since these were obtained using an ideal motor model, the loci deviate significantly from those obtained experimentally.

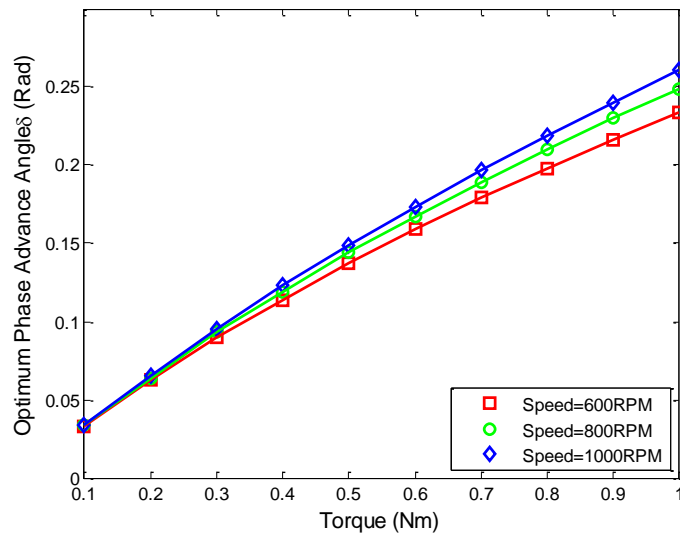


Figure 4-8: Optimum phase advance angles as a function of torque and for different speed considering ideal motor model.

4.5. Incorporating Non-idealities in Motor Model

As described in Section 2.6, an IPM shows large variations in parameters depending on operating conditions. The optimum value for δ depends on motor parameters, as shown in Eqn. 4-15 and 4-16 where parameter variations inflict significant impact on the locus of

δ_{opt} . Variations in motor parameters can be categorized into slow and abrupt variation. The slow variation in resistance and flux linkage are due to the temperature variation. The abrupt variation in inductances are due to magnetic saturation. Experimental results show that, large variation in rotor inductance along the quadrature axis affects the performance significantly.

To validate the performance of the proposed scheme, motor non-idealities were incorporated into the simulation model. For better comparison, the exact model of the experimental motor was built in simulations incorporating magnetic saturation.

Since most of the literature suggests L_q to be a function of quadrature axis current i_q , [24] [25] [43] the experimental motor was operated at a constant speed with varying loading conditions which resulted variation in i_q . Motor current was averaged over several cycles at steady state to ensure $\frac{di_q}{dt}$ and $\frac{di_d}{dt}$ to be zero. The following steady state equation was used to estimate L_q

$$L_q = \frac{-(v_d - Ri_d)}{\omega i_q} \quad (4-17)$$

Figure 4-9 shows variation of L_q for the IPM from the experimental test setup. The solid line shows the quadrature axis inductance measured from the experimental IPM. To incorporate the saturation effects, the inductance is described as a non-linear function of i_q . The dotted line represents the approximated L_q as a function of i_q for simulation purposes. Least square estimation [44] was used to estimate the parameters for the non-linear function. The following equation was used for the approximation

$$L_{qA} = 0.0151 i_q^{-0.5} \quad (4-18)$$

For the d -axis inductance, the variation is quite small compared to changes in L_q [24]. Thus, a small linear drop was assumed as shown in Figure 4-10. These inductance variations add realistic effects in motor performance in simulation.

Motor inductance was also measured using an LCR meter according to the method proposed in [45]. Inductance was measured for one complete revolution of the rotor which is referred to as two electrical cycles (2 pole pair motor). The vertical dotted lines indicate the position for rotor d -axes. The horizontal lines show the quadrature and direct axis inductances. It was observed that, L_q values for two electrical cycles were different from one another. Though this non-ideality was not incorporated in simulation, this variation in inductance can affect the performance of the experimental motor.

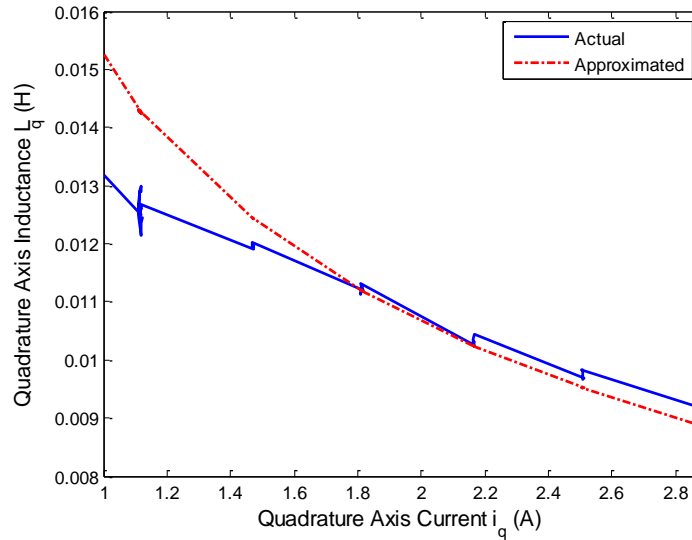


Figure 4-9: Variation in quadrature axis inductance L_q with change in i_q .

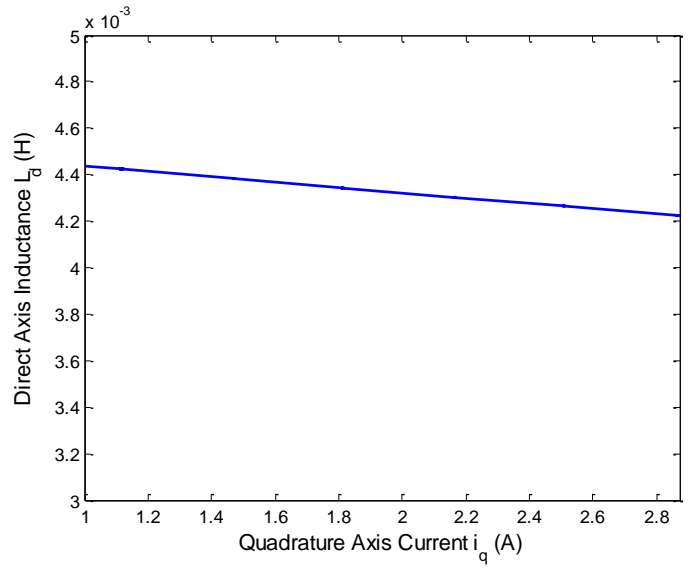


Figure 4-10: Variation in direct axis inductance L_d with change in i_q .

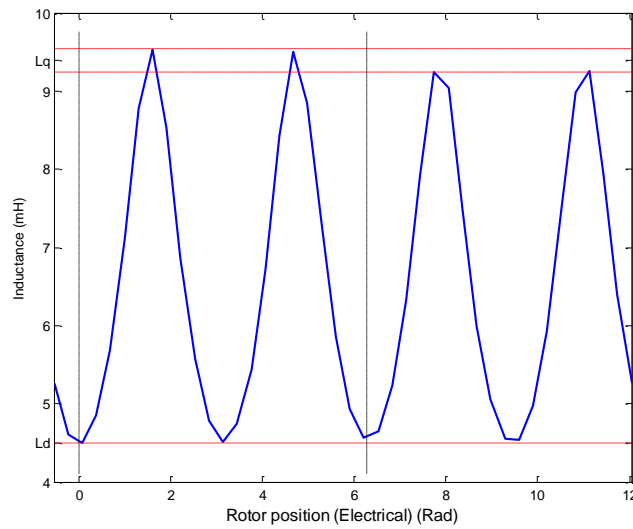


Figure 4-11: Motor inductance measured using LCR meter for one mechanical or two electrical cycles (The dotted horizontal lines show quadrature and direct axis inductance values. Vertical dotted lines indicate the rotor d -axes).

4.6. Maximum Power per Ampere Concept (MPPA)

Introduction of magnetic saturation makes the computation for the MTPA trajectory difficult. Moreover, copper loss is not the only loss associated with PM motors. An IPM can suffer from iron losses, stray losses and harmonic losses which are all the functions of operating conditions and motor parameters [39]. It will be ideal if the optimum trajectory is computed considering all these losses instead of considering only copper loss. Moreover, the plot of optimum δ as a function of torque is also not feasible in practical applications since it requires an expensive torque sensor or a very good torque estimator. It was found that the $i_d i_q$ trajectory obtained for achieving Maximum Power Per Ampere (MPPA) actually coincides with one found for MTPA [24]. It will also simplify the implementation since DC input power measurement requires only one current sensor when constant bus voltage is maintained. Though losses arising from any source other than copper loss was not considered in simulation, the MPPA point in experimental case would minimize total losses in the motor. The DC link power input in a motor drive system can be expressed in following way

$$P_{in} = T_L \omega_M + P_{copper} + P_{others} \quad (4-19)$$

Here, $T_L \omega_M$ represents the mechanical output power. P_{copper} is the copper loss associated with stator resistance that would have the minimum value in MTPA condition. P_{others} is the combination of all other losses including harmonic loss, stray loss, iron loss, etc. The objective of the MPPA control scheme is to minimize the DC input power for a given speed or torque condition.

4.7. Procedure for Finding the Optimum Phase Advance Angle (δ_{opt})

To find the optimum operating point considering all non-idealities in a real motor, a brute-force or exhaustive search algorithm was adopted. This technique can be referred as a training period for the main algorithm to gather enough information about the motor.

The motor was operated at a constant speed and phase advance angle was varied at constant step size starting from a minimum value limit up to a maximum limit. It was made sure that all possible δ values were covered in the process. To ensure that, the boundary limits for the varying process were chosen to be well beyond the feasible limits computed using the constant parameter model of the experimental motor. Figure 4-12 through Figure 4-18 present sample data taken while operating the motor at a constant speed of 800 RPM. Load torque was varied starting from 0 Nm to 0.8 Nm as shown in Figure 4-13. Application of a sudden load introduced a glitch in the speed response which was used as a trigger for starting the new δ variation (shown in Figure 4-14). Since a PI controller was dedicated for generating the necessary voltage to attain the reference speed, gradual variation in δ did not cause any change in the operating speed. The necessary change in voltage magnitude determined by the PI controller is shown in Figure 4-15. It was found that, higher values of δ caused a drop in required voltage since larger δ caused larger demagnetizing current i_d as shown in Figure 4-16. Larger i_d with the introduction of larger δ also caused larger reluctance torque. Since constant load torque was maintained during a ramp change in δ , i_q was automatically reduced to maintain a constant speed as seen in Figure 4-17. Figure 4-18 represents the most important measure for the procedure, which is the DC link input power. It can be observed that, for each torque level, the power input

curve holds a bowl shape with the variation in δ . Thus, there exists an optimum point for δ which will result in the minimum input power. The main purpose of the algorithm is to find the optimum phase advance angle δ_{opt} for any operating conditions. To collect necessary data for optimizing δ , the same procedure was repeated for different operating speeds. Afterwards, an automated program was run to find the optimum δ at each torque level. This generates a two dimensional matrix for optimum δ that covers the entire torque-speed range that the motor is intended to operate.

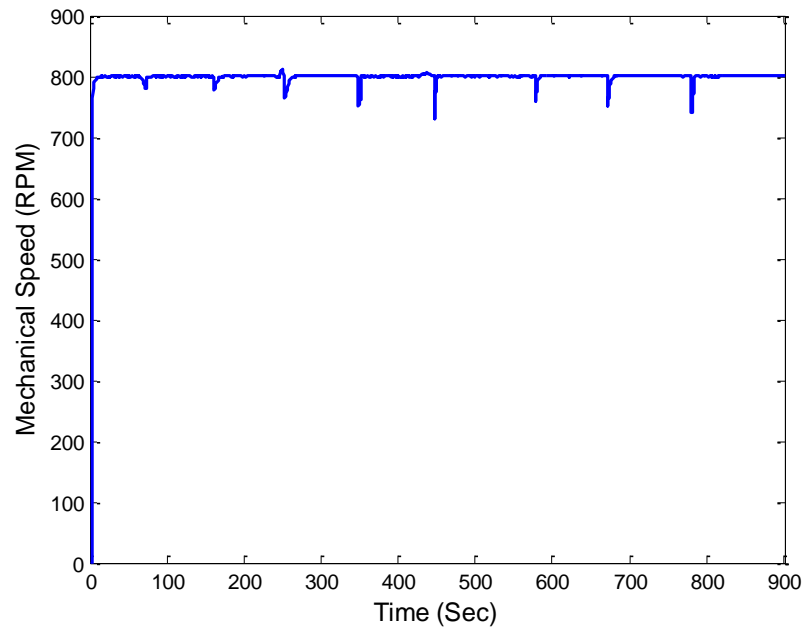


Figure 4-12: Constant speed operation for generating sufficient data to choose optimum phase advance angle δ . The small glitches on the speed represent the introduction of higher load torque at those instants.

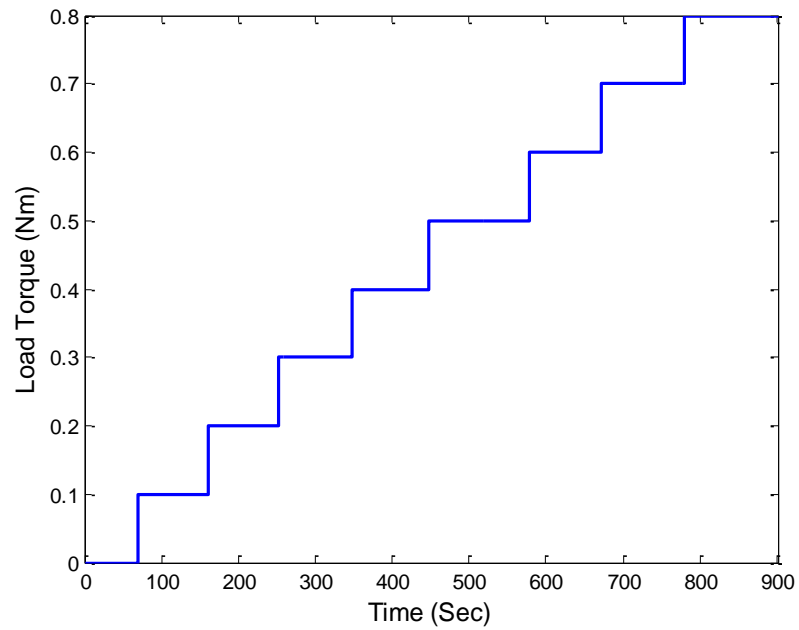


Figure 4-13: Load torque profile applied for each operating speeds data were taken.

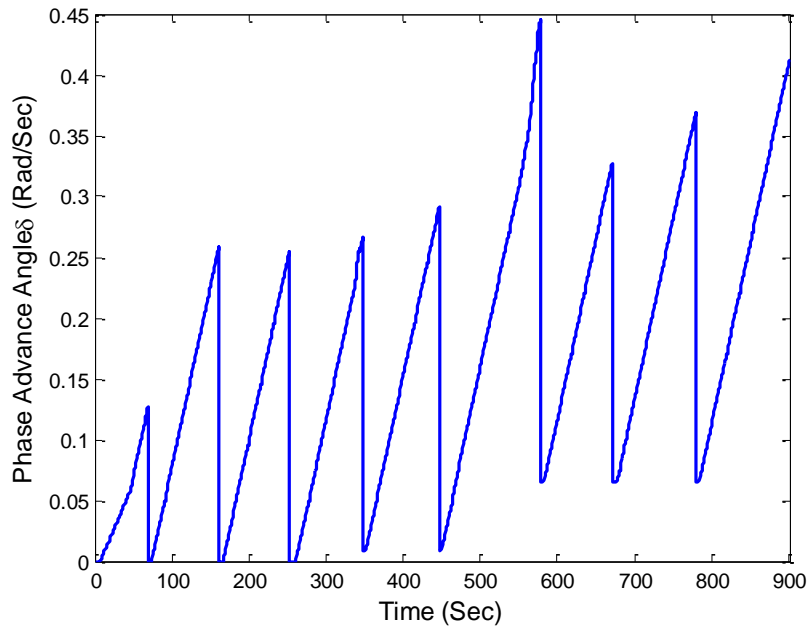


Figure 4-14: The constant step variation of phase advance angle for different values of load torque. Each time any glitch detected in the speed profile represented an introduction of load torque which was used as a trigger for starting of a new ramp.

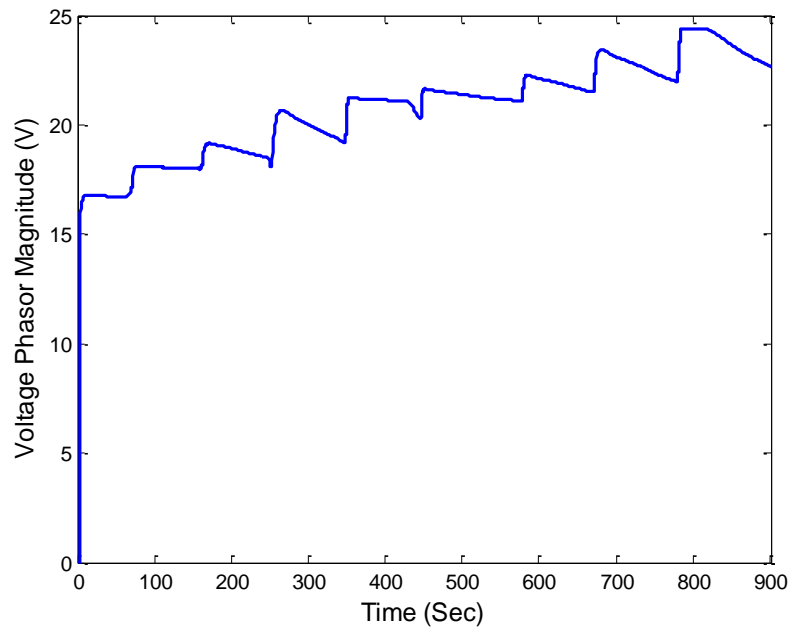


Figure 4-15: Variation in required terminal voltage with the change in δ .

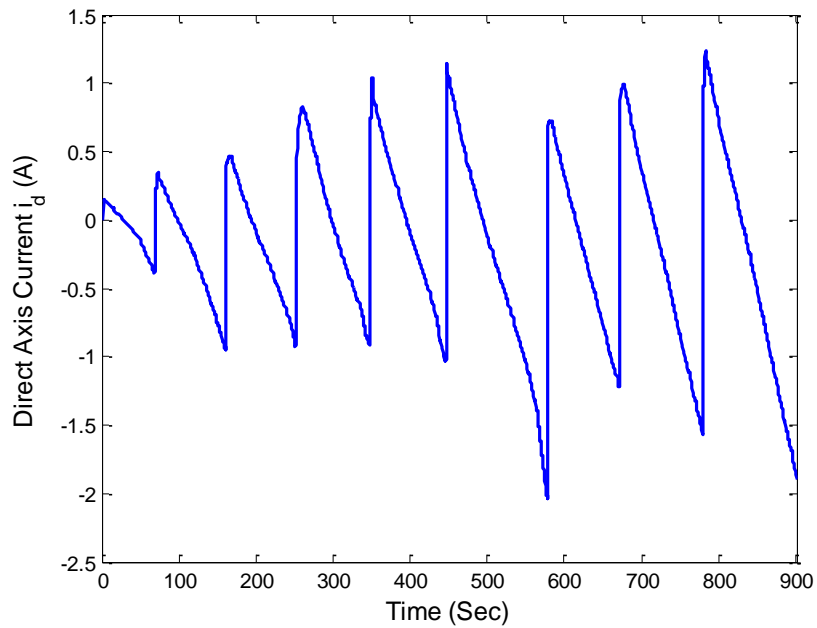


Figure 4-16: Change in direct axis current with the change in phase advance angle. As anticipated, higher values of δ generated larger d -axis current in negative axis giving higher reluctance torque.

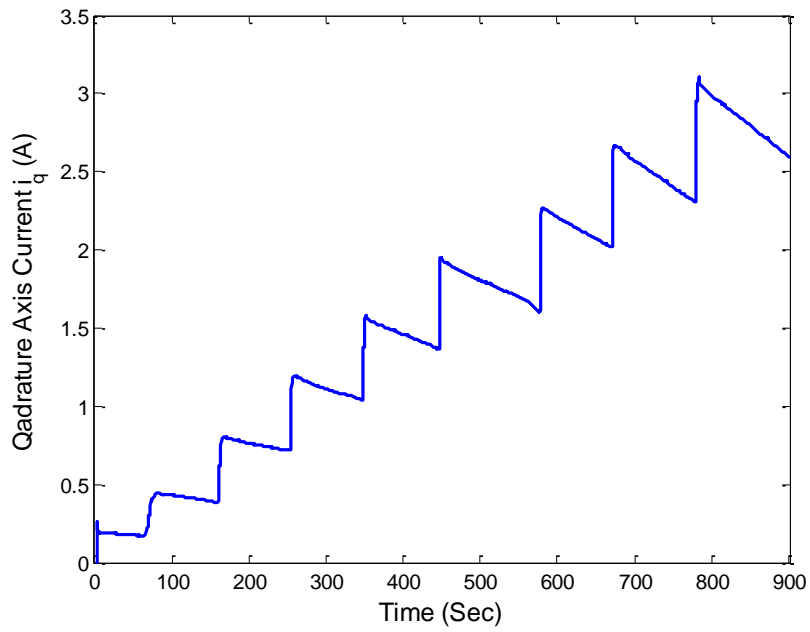


Figure 4-17: Variation in quadrature axis current with the change in δ .

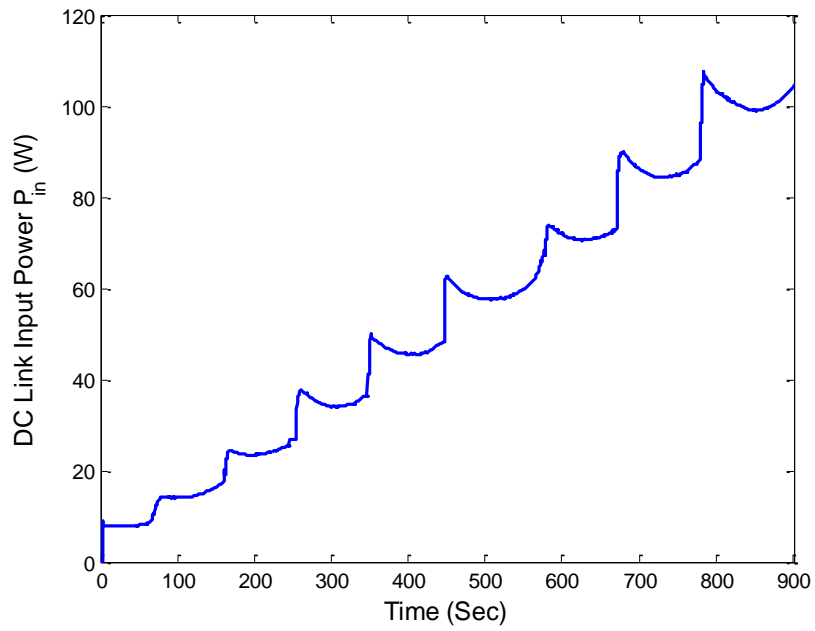


Figure 4-18: Variation in DC link input power with the change in δ . The curve holds a 'bowl' shape at each torque level with the change in δ .

4.8. MTPA and MPPA Coincidence

The proposed MPPA control scheme works on minimizing DC link input power. Since the well-established method for optimizing IPM performance is running the motor in the MTPA condition, a comparison is provided through Figure 4-19 to Figure 4-24. The automated program for analyzing the training data was run for finding δ s that minimize DC link input power (MPPA). The same program was run for finding δ s that minimize the magnitude of stator current (MTPA). The MPPA points are marked by squares whereas MTPA points are marked by ∇ in Figure 4-19 to Figure 4-24. It was found that, for most of the cases, these points coincide with one another. A slight mismatch was found in certain cases as shown in Figure 4-23 and Figure 4-24 which might be caused by measurement errors.

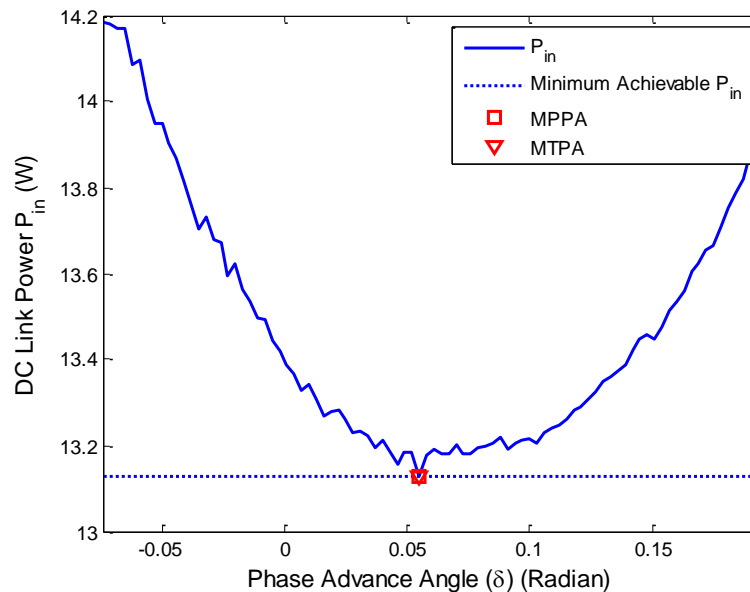


Figure 4-19: DC link input power for different δ (700 RPM with 0.1 Nm load torque).

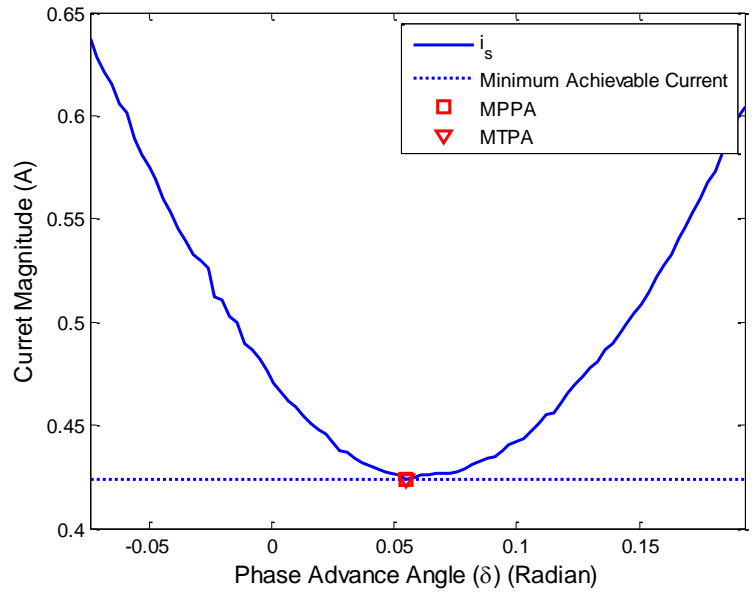


Figure 4-20: Current magnitude for different δ (700 RPM with 0.1 Nm load torque).

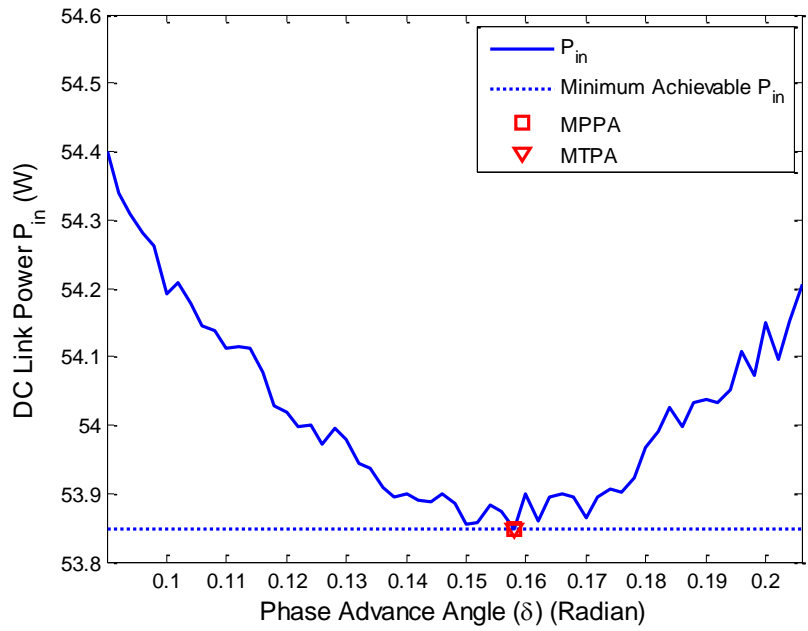


Figure 4-21: DC link input power for different δ (700 RPM with 0.5 Nm load torque).

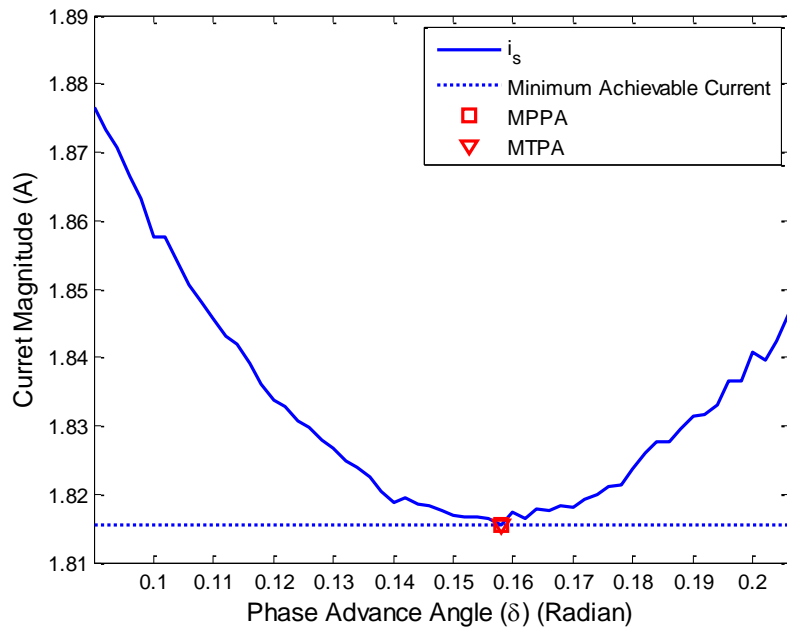


Figure 4-22: Current magnitude for different δ (700 RPM with 0.5 Nm load torque).

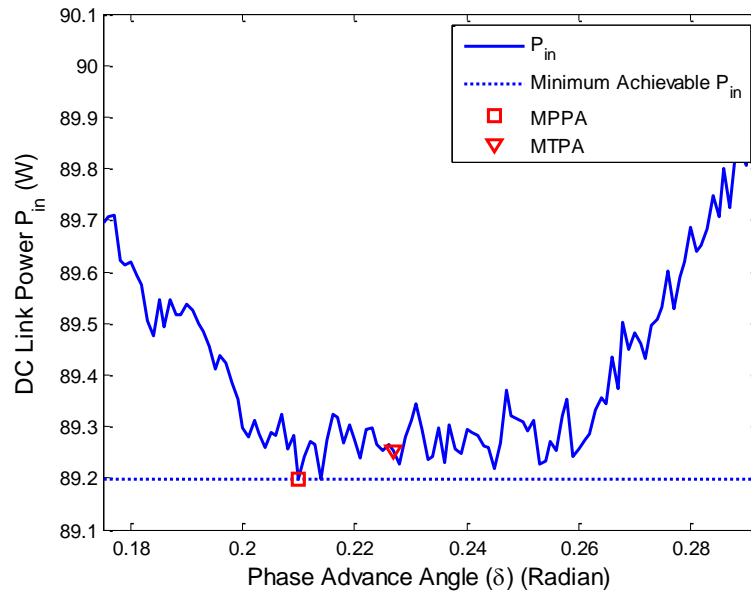


Figure 4-23: DC link input power for different δ (700 RPM with 0.8 Nm load torque).

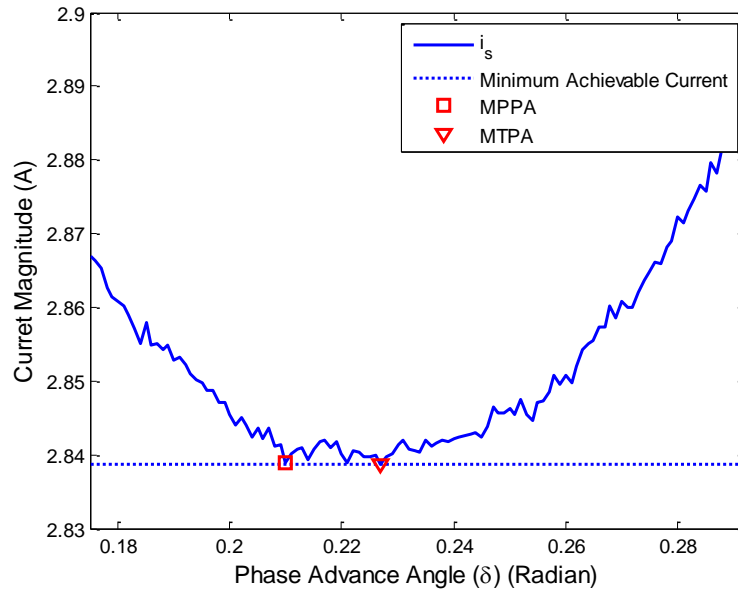


Figure 4-24: Current magnitude for different δ (700 RPM with 0.8 Nm load torque).

The same brute-force search algorithm was run in the simulation as well. Since measurement error was absent in simulation, coincidence between MPPA and MTPA was stronger. Figure 4-25 and Figure 4-26 show the curves obtained using simulation where ‘square’ marks and ∇ present the points of MPPA and MTPA respectively. Minor deviation were found, which were due to the delay in DC link current measurement that arose from the DC link capacitor. The capacitor attached at the input of the inverter filters the DC link input current introducing a smoothing effect with some delay. This effect due to the inverter input capacitor was also incorporated in the simulation.

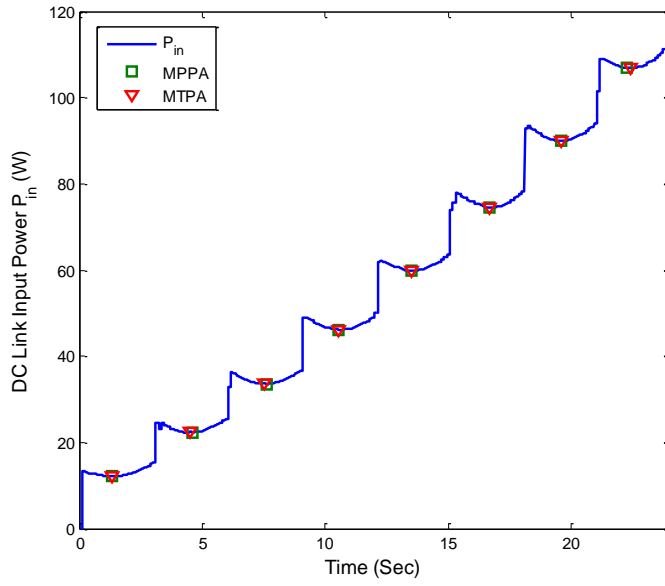


Figure 4-25: DC link input power with the change in δ obtained using simulation for 800 RPM.

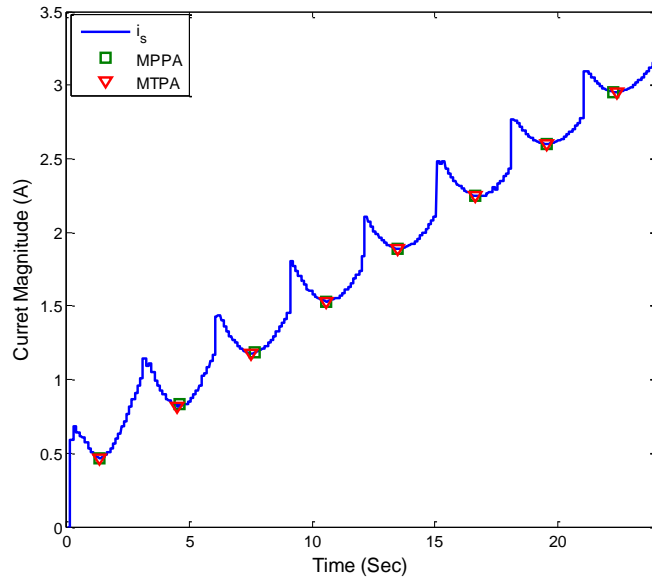


Figure 4-26: Current phasor magnitude with the change in δ obtained using simulation for 800 RPM.

4.9. Analysis for Optimum δ_{opt}

Following the procedures described in Section 4.7, a two dimensional matrix for optimum phase advance angle δ_{opt} was obtained. The 2D matrices for δ_{opt} are plotted in Figure 4-27 and Figure 4-28. Figure 4-27 shows the δ_{opt} matrix found experimentally, whereas Figure 4-28 is the one found from the simulation. Substantial resemblance is present between Figure 4-27 and Figure 4-28 due to the incorporation of non-idealities created by inductance droop in the simulation model. For easier observation, δ_{opt} versus torque curves for three different speeds are presented in Figure 4-29 and Figure 4-30 respectively. Both of the plots show noteworthy dissimilarities with the one computed using ideal motor model (shown in Figure 4-8).

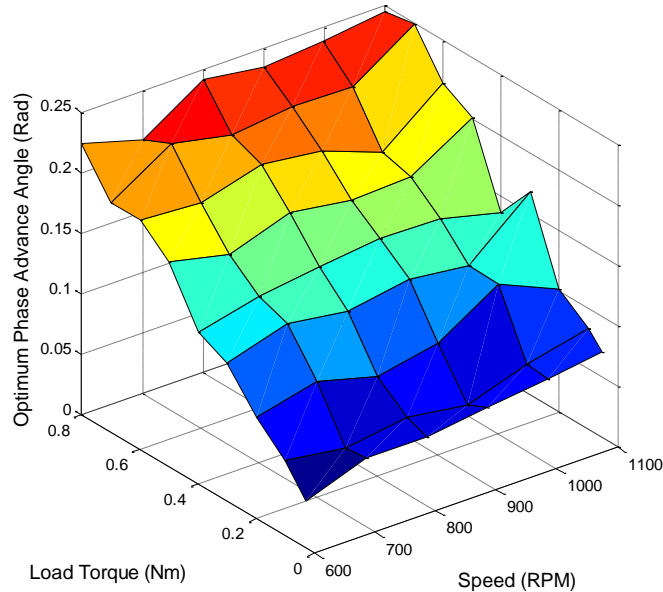


Figure 4-27: Optimum phase advance angle δ_{opt} with the variation of load torque and operating speed (Experimental).

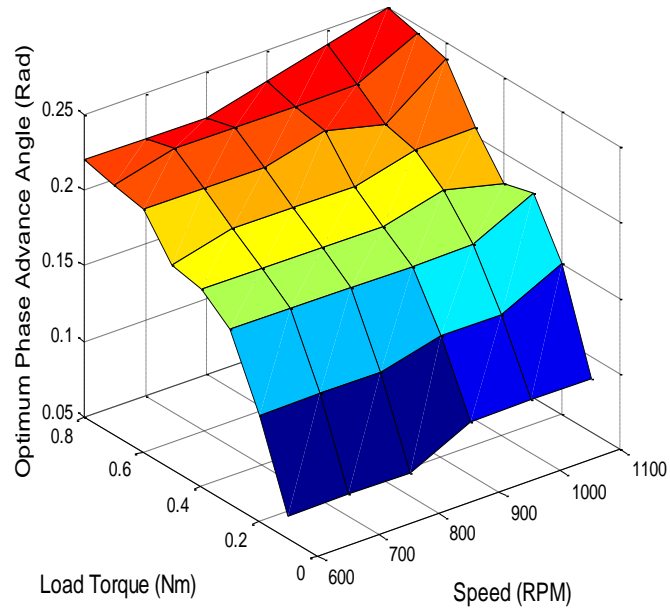


Figure 4-28: Optimum phase advance angle δ_{opt} with the variation of load torque and operating speed (Simulation).

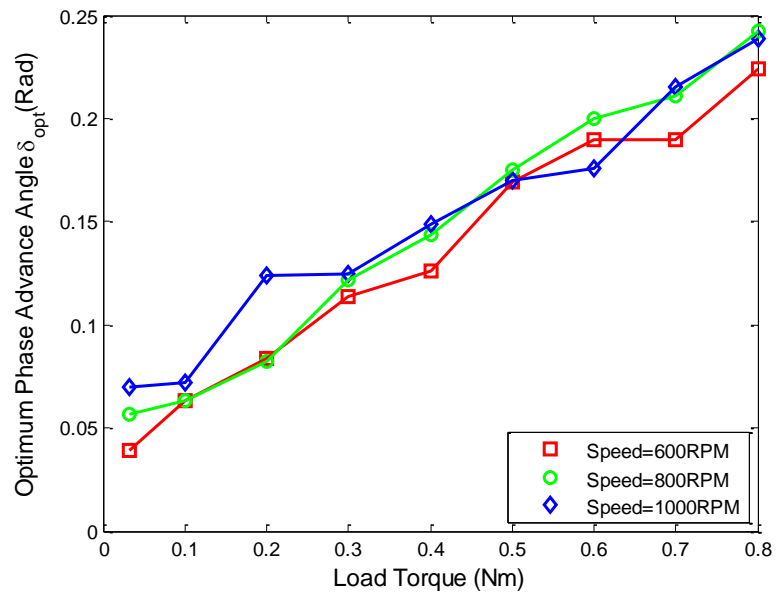


Figure 4-29: Optimum phase advance angle variation with load torque obtained for three different speed (Experimental).

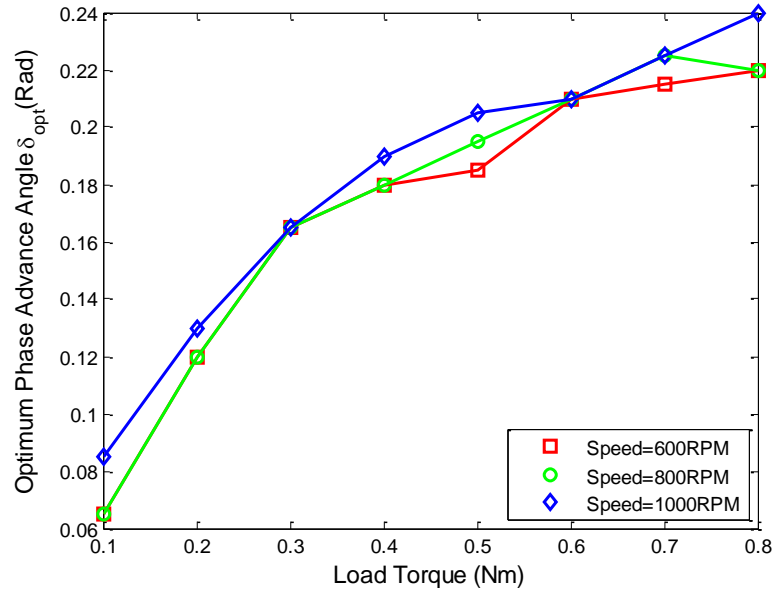


Figure 4-30: Optimum phase advance angle variation with load torque obtained for three different speed (Simulation).

4.10. Estimation for Optimum δ_{opt}

As mentioned in Section 4.2, the proposed algorithm was developed based on measurement of only DC link power and operating speed. All the plots shown so far presented δ_{opt} as a function of load torque at different speeds. To avoid the expense of a costly torque sensor and additional current sensors to measure 3-phase current, it is necessary to find δ_{opt} as a function of DC link input power. δ_{opt} matrices as functions of DC link power for different operating speeds, are shown in Figure 4-31 (experimental) and Figure 4-32 (simulation). It is observed that, both simulation and experimental plots hold near identical limits in the DC link power. In order to simulate losses in the power devices, an additional resistance was considered in series with each phase of the motor. δ_{opt} as a function of DC link power for three different speeds are also presented in Figure 4-33 and Figure 4-34 for ease of

observation. The primary and most important task for the proposed algorithm is to compute optimum δ based on DC link power and operating speed.

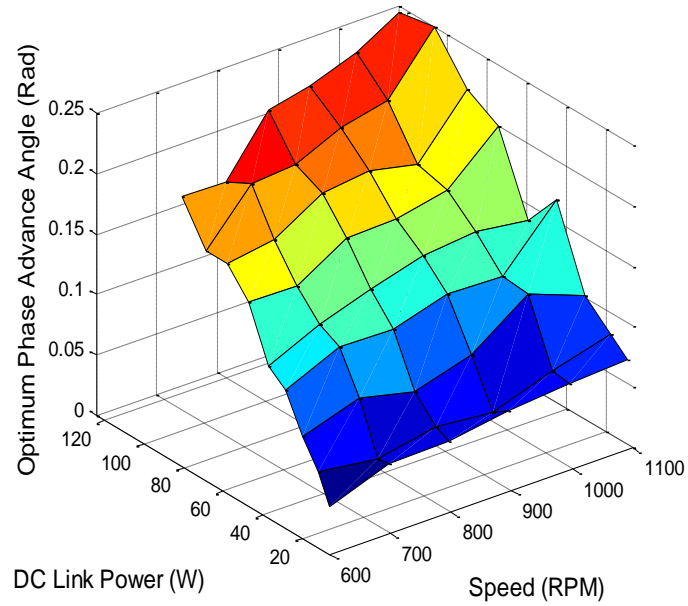


Figure 4-31: Optimum phase advance angle δ_{opt} as a function of DC link power and operating speed (Experimental).

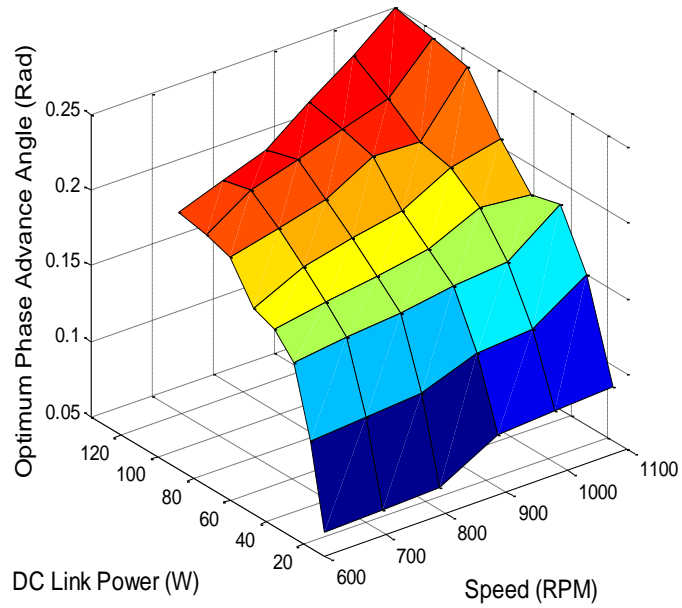


Figure 4-32: Optimum phase advance angle δ_{opt} as a function of DC link power and operating speed (Simulation).

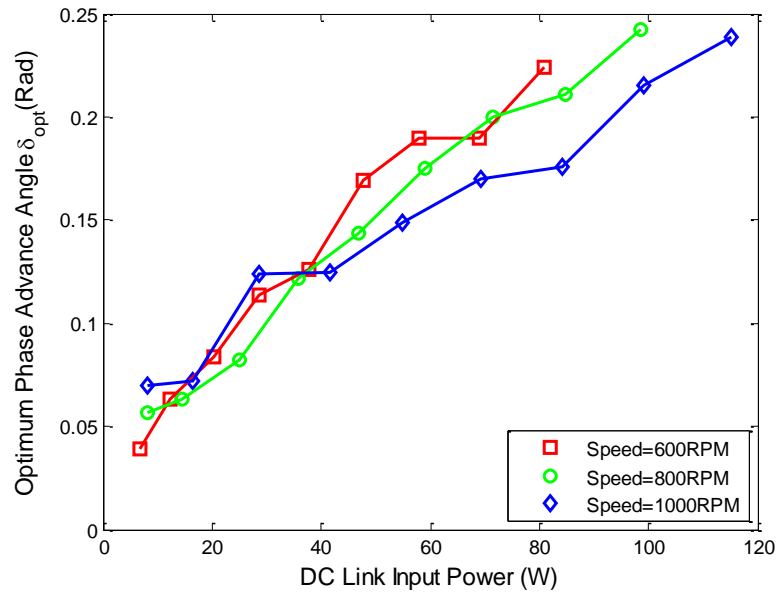


Figure 4-33: Optimum phase advance angle Vs. DC link input power obtained for three different speeds (Experimental).

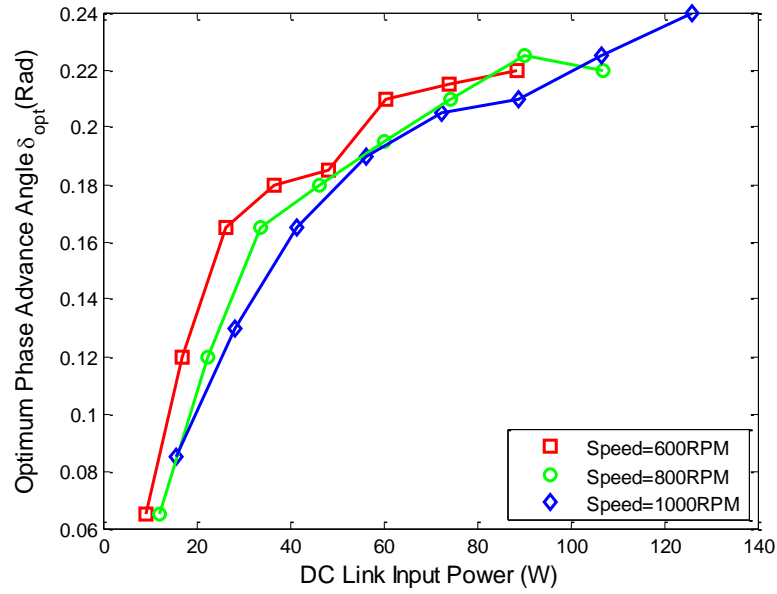


Figure 4-34: Optimum phase advance angle Vs. DC link input power obtained for three different speeds (Simulation).

Careful observation of the locus of δ_{opt} suggests estimating δ_{opt} using a non-linear polynomial of DC link power P_{dc} . It was found that, a second order polynomial was sufficient for satisfactory estimation of δ_{opt} at a certain speed. The following equation was used for primary estimation of δ_{opt}

$$\delta_{optE_p}(\omega_M, P_{dc}) = M_{\omega_M}(1)P_{dc} + M_{\omega_M}(2)P_{dc}^2 \quad (4-20)$$

here, δ_{optE_p} = primary estimated value for δ_{opt}

M_{ω_M} = estimation coefficient vector at operating speed of ω_M

The error in estimation can be expressed as

$$Error = \left(\delta_{optE_p} - \delta_{opt} \right)^2 \quad (4-21)$$

Equation 4-21 represents the error between actual and estimated δ_{opt} and was taken as the objective function to be minimized. Least Square Estimation (LSE) [44] was adopted to find the elements of M_{ω_M} for different operating speeds.

The phase advance angle obtained using the estimation polynomial given in Eqn. 4-20 is shown in Figure 4-35. This plot was generated for the operating speed of 800 RPM. For successful implementation of the algorithm, similar coefficients must be obtained for speeds which cover the entire speed-torque region the motor is intended to operate.

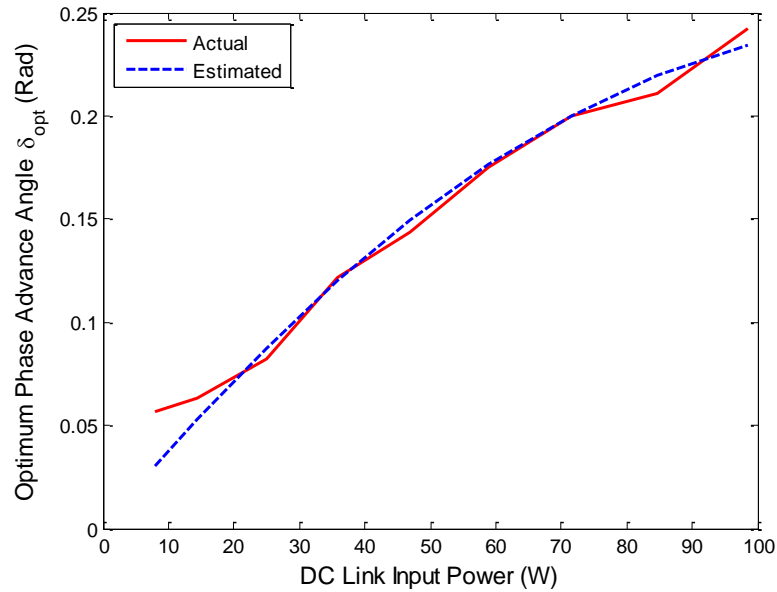


Figure 4-35: Optimum phase advance angle δ_{opt} estimated using Eqn. 4-20 for 800 RPM. Solid line presents the actual δ_{opt} whereas estimated angle is shown in dotted line.

The search algorithm mentioned in Section 4.7 was run on the experimental platform for 6 different speeds between 600 RPM to 1100 RPM. If δ_{opt} had been calculated for N_s different speeds, the estimation technique expressed so far would require $N_s \times 2$ coefficients. This would not be a feasible solution especially when a wide speed range is

to be covered. That is why, a 2-dimensional LSE was considered for covering a wide speed-torque range. If δ_{opt} is calculated for N_s different speeds, each speed will provide one vector M_{ω_M} . Thus, M_{ω_M} can be considered as an $N_s \times 2$ matrix. To avoid storage of a larger number of coefficients, each column vector of the $N_s \times 2$ matrix can be further estimated as a function of mechanical speed. It was found that, a third order polynomial was necessary for satisfactory estimation of the primary estimation matrix. Thus, the estimation coefficients can be expressed as

$$M_{\omega_{ME}}(n) = \sum_{m=1}^3 D_M(n, m) \omega_M^m \quad (4-22)$$

The D_M matrix was the final estimation matrix stored in the algorithm. Since only two coefficients were chosen for the primary estimation and the final estimation required three degree polynomials, D_M was a 2×3 matrix containing only 6 elements.

The performance of the D_M matrix for estimating the coefficients M_{ω_M} as a function of speed are shown in Figure 4-36 and Figure 4-37. Estimated values of M_{ω_M} are shown in dotted line. The final estimated value of δ_{opt} found using calculated $M_{\omega_{ME}}$ and DC link power is shown in Figure 4-38.

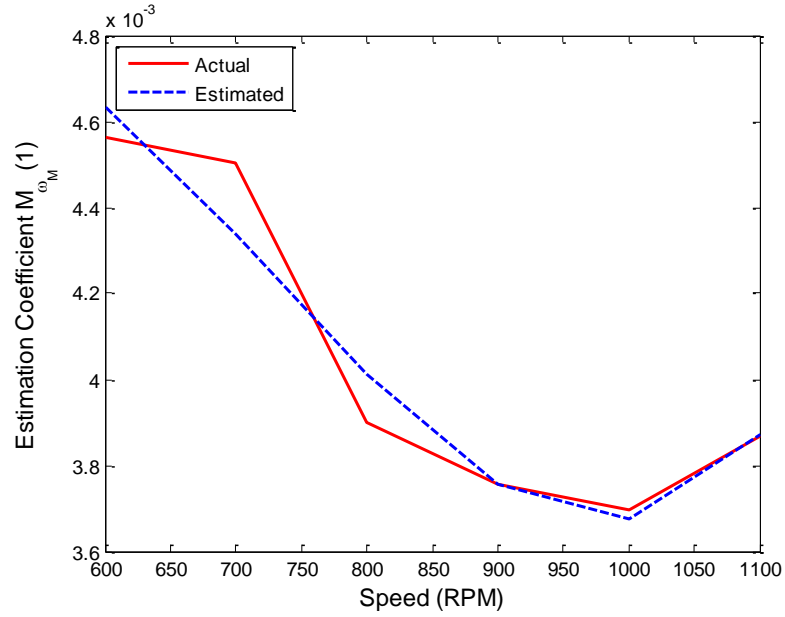


Figure 4-36: $M_{\omega_{ME}}(1)$ plotted as a function of speed using Eqn.4-22 (Shown in dotted line). The solid line shows $M_{\omega_M}(1)$ obtained during primary adaptation of Least Square method.

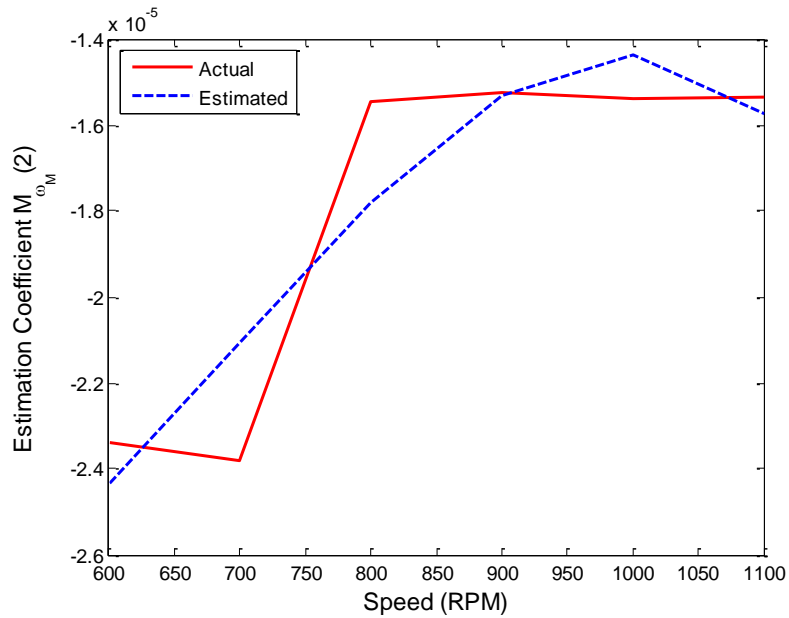


Figure 4-37: $M_{\omega_{ME}}(2)$ plotted as a function of speed using Eqn.4-22 (Shown in dotted line). The solid line shows $M_{\omega_M}(2)$ obtained during primary adaptation of least square method.

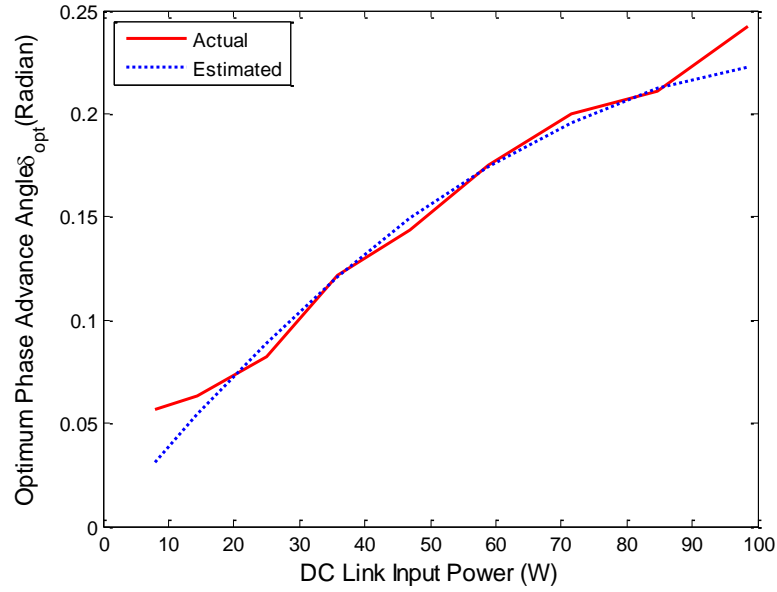


Figure 4-38: Optimum phase advance angle δ_{opt} estimated using Eqn. 4-20 for 800 RPM. M_{ω_M} vector for computing δ_{opt} was estimated using Eqn. 4-22. Solid line presents the actual δ_{opt} whereas estimated angle is shown in dotted line.

Thus, the final estimation for optimum phase advance angle can be expressed using the following matrix notation

$$\begin{bmatrix} M_{\omega_{ME_1}} \\ M_{\omega_{ME_2}} \end{bmatrix} = \begin{bmatrix} D_{M_{11}} & D_{M_{12}} & D_{M_{13}} \\ D_{M_{21}} & D_{M_{22}} & D_{M_{23}} \end{bmatrix} \begin{bmatrix} \omega_M \\ \omega_M^2 \\ \omega_M^3 \end{bmatrix} \quad (4-23)$$

$$[\delta_{optE}] = [P_{dc} \quad P_{dc}^2] \begin{bmatrix} M_{\omega_{ME_1}} \\ M_{\omega_{ME_2}} \end{bmatrix} \quad (4-24)$$

Thus following matrix multiplication provides the optimum δ at any operating condition

$$[\delta_{optE}] = [P_{dc} \quad P_{dc}^2] \begin{bmatrix} D_{M_{11}} & D_{M_{12}} & D_{M_{13}} \\ D_{M_{21}} & D_{M_{22}} & D_{M_{23}} \end{bmatrix} \begin{bmatrix} \omega_M \\ \omega_M^2 \\ \omega_M^3 \end{bmatrix} \quad (4-25)$$

4.11. Convergence of the Proposed Algorithm

The estimation procedure for optimum phase advance angle δ_{opt} takes the DC link input power as an input parameter. The input power used for building the estimation matrix D_M is the minimum achievable power level at a certain operating condition. In other words, this level is the power level located at the trough of the bowl shaped curve shown in Figure 4-19. Since the objective of the control scheme is to reach that minimum power level located at the bottom of the curve, this level should be the outcome of the algorithm, not an input. At this point, the algorithm seems to lose its applicability in practical operation. But a closer look at Figure 4-39 and Figure 4-40 proves the algorithm to be self-converging to the optimum point. DC link input power P_{dc} at a constant speed is presented in Figure 4-39 which is a function of phase advance angle. The input variable δ is shown in Figure 4-40 as blue steps. The estimated phase advance angle δ_{optE} is shown as red line in Figure 4-40. δ_{optE} was calculated using the estimation matrix D_M proposed in Section 4.10 with P_{dc} shown in Figure 4-39 as an input variable.

For a given δ at point 'A' of Figure 4-40, IPM would draw a DC power amount given at point 'B' of Figure 4-39. For a DC power given at point 'B' in Figure 4-39, the algorithm generates a δ given at point 'C' of Figure 4-40. Since δ at 'C' is lower than the δ at 'A' the operation would not diverge.

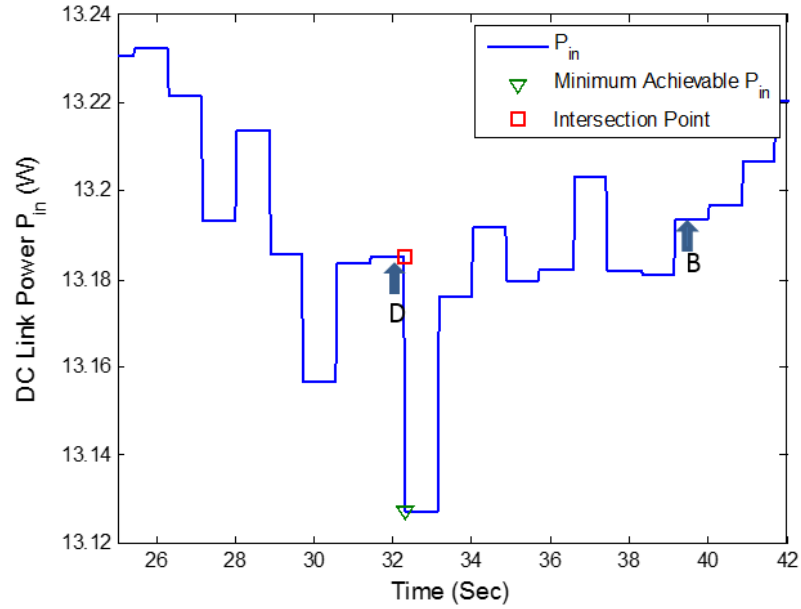


Figure 4-39: The bowl shaped DC link input power curve at 700 RPM with 0.1 Nm load torque (Zoomed in at the bottom of the curve).

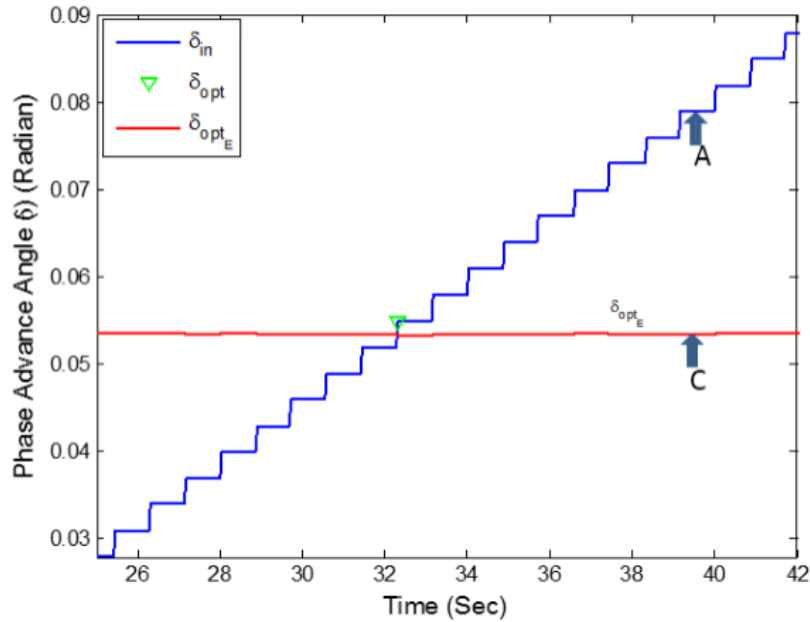


Figure 4-40: Variation in δ is shown in blue step function which resulted power variation shown in Figure 4-39. δ_{opt} is marked by ∇ . The red line represents the phase advance angle calculated using estimation matrix D_M with power variation shown in Figure 4-39 as input.

4.12. Design Procedure of the PI Controller

The PI controller shown in Figure 4-1 is responsible for generating the necessary voltage for achieving commanded speed and must be designed carefully for satisfactory performance. In this section, the steps taken for analyzing the system and going through a successful design procedure for the PI controller will be described.

Any mechanical rotating body with inertia J and damping coefficient B_c can be expressed using the following differential equation under a load torque of T_L [46][47]

$$T_e = J \frac{d\omega}{dt} + B_c \omega + T_L \quad (4-26)$$

To get a linear transfer function, the load torque can be considered as an increase in damping coefficient and thus Eqn.4-26 can be rewritten as

$$T_e = J \frac{d\omega}{dt} + B_c \omega \quad (4-27)$$

This gives the following linear transfer function in the Laplace domain

$$\omega(s) = \frac{T_e(s)}{Js + B_c} \quad (4-28)$$

Instead of using the mechanical speed as a measure of speed, electrical speed in radians per second was considered to avoid conflict with the electrical speed used in all voltage current relationships. At this point, a relationship between voltage magnitude v_m and produced torque T_e must be determined. Combining Eqn. 4-7, 4-8, 4-9, we get

$$T_e = \left(k_1 + k_2 \left(\frac{1}{Z_m^2} (RV \cos(\delta) - \omega R \phi_M + \omega L_d V \sin(\delta)) \right) \right) \left(\frac{1}{Z_m^2} (-RV \sin(\delta) - \omega^2 L_q \phi_M + \omega L_q V \cos(\delta)) \right) \quad (4-29)$$

where $Z_m^2 = R^2 + \omega^2 L_q L_d$, $k_1 = \frac{3}{2} P \phi_M$, $k_2 = \frac{3}{2} P (L_d - L_q)$

Equation 4-29 provides a straight forward relationship between torque output and applied voltage at a certain speed. Algebraic manipulation on Eqn. 4-29 provides the following torque equation

$$T_e = F_1(\omega, \delta) + F_2(\omega, \delta)V + F_3(\omega, \delta)V^2 \quad (4-30)$$

where

$$F_1(\omega, \delta) = -\frac{k_1}{Z_m^2} \omega R_s \phi_M + \frac{k_2}{Z_m^4} \omega^3 L_q R_s \phi_M^2 \quad (4-31)$$

$$F_2(\omega, \delta) = -\frac{k_1}{Z_m^2} R_s \cos(\delta) + \frac{k_1}{Z_m^2} \omega L_d \sin(\delta) + \frac{k_2}{Z_m^4} R_s^2 \omega \phi_M \sin(\delta) - \frac{k_2}{Z_m^4} R_s \omega^2 \phi_M L_q \cos(\delta) - \frac{k_2}{Z_m^4} \omega^3 L_q L_d \phi_M \sin(\delta) + \frac{k_2}{Z_m^4} R_s \omega^2 L_q \phi_M \cos(\delta) \quad (4-32)$$

$$F_3(\omega, \delta) = -\frac{k_2}{Z_m^4} R_s^2 \sin(\delta) \cos(\delta) + \frac{k_2}{Z_m^4} R_s \omega L_d \sin^2(\delta) + \frac{k_2}{Z_m^4} \omega L_q R_s \cos^2(\delta) + \frac{k_2}{Z_m^4} \omega^2 L_q L_d \sin(\delta) \cos(\delta) \quad (4-33)$$

Using Eqn. 4-30 in Eqn. 4-27 gives the following differential equation in the time domain

$$\dot{\omega} = -B_c\omega + F_1(\omega, \delta) + F_2(\omega, \delta)V + F_3(\omega, \delta)V^2 \quad (4-34)$$

here, $\dot{\omega}$, ω , δ are all time varying quantities. Equation 4-34 is clearly a non-linear function of voltage reference and thus difficult to analyze for PI controller design. A linearization of the non-linear function around a nominal operating point would be helpful in the design process [48]. If ω_n and V_n are the nominal system input and output respectively, then Eqn. 4-34(4-34) can be rewritten as

$$\begin{aligned} \dot{\omega}_n + \Delta\dot{\omega} = & -B_c\omega_n - B_c\Delta\omega + F_1(\omega_n + \Delta\omega) + F_2(\omega_n + \Delta\omega)V \\ & + F_3(\omega_n + \Delta\omega)V^2 \end{aligned} \quad (4-35)$$

δ is assumed constant in the modeling as the bandwidth of the PI controller is much faster than the variation in δ . The right hand side of the expansion can be expressed using a Taylor series expansion ignoring the higher order terms. Thus

$$\begin{aligned} \dot{\omega}_n + \Delta\dot{\omega} = & -B_c\omega_n - B_c\Delta\omega + F_1(\omega_n) + F_2(\omega_n)V + F_3(\omega_n)V^2 + \\ & \frac{\partial F_1(\omega_n)}{\partial \omega} \Delta\omega + \frac{\partial F_2(\omega_n)V_n}{\partial \omega} \Delta\omega + \frac{\partial F_3(\omega_n)V_n^2}{\partial \omega} \Delta\omega + \frac{\partial F_1(\omega_n)}{\partial V} \Delta V + \frac{\partial F_2(\omega_n)V_n}{\partial V} \Delta V + \\ & \frac{\partial F_3(\omega_n)V_n^2}{\partial V} \Delta V + \text{H.O.T} \end{aligned} \quad (4-36)$$

If the nominal operating points are chosen correctly, Eqn. 4-36 will be simplified into

$$\begin{aligned} \Delta\dot{\omega} = & -B_c\Delta\omega + \frac{\partial F_1(\omega_n)}{\partial \omega} \Delta\omega + \frac{\partial F_2(\omega_n)V_n}{\partial \omega} \Delta\omega + \frac{\partial F_3(\omega_n)V_n^2}{\partial \omega} \Delta\omega \\ & + \frac{\partial F_1(\omega_n)}{\partial V} \Delta V + \frac{\partial F_2(\omega_n)V_n}{\partial V} \Delta V + \frac{\partial F_3(\omega_n)V_n^2}{\partial V} \Delta V \end{aligned} \quad (4-37)$$

The derivatives of $F_1(\omega)$, $F_2(\omega)$ and $F_3(\omega)$ with respect to ω around the nominal speed of ω_n were found numerically since the functions containing ω are highly non-linear. Derivatives with respect to the voltage were quite simple to compute since $F_1(\omega)$, $F_2(\omega)$ and $F_3(\omega)$ are independent of V . Performing all the computations, Eqn.4-37 can be rewritten as

$$\Delta\dot{\omega} = G\Delta\omega + H\Delta V \quad (4-38)$$

where

$$G = -B_c + \frac{\partial F_1(\omega_n)}{\partial \omega} + \frac{\partial F_2(\omega_n)V_n}{\partial \omega} + \frac{\partial F_3(\omega_n)V_n^2}{\partial \omega} \quad (4-39)$$

$$H = F_2(\omega_n) + 2V_n F_3(\omega_n) \quad (4-40)$$

Taking the Laplace transformation, the following transfer function results

$$\Delta\omega(s) = \frac{H\Delta V(s)}{s - G} \quad (4-41)$$

Considering the operating voltage range of the experimental and simulation model of the IPM, 25 V was chosen as a nominal voltage. Using the steady state parameters of the IPM, the nominal speed is found to be 143.8 rad/sec for 25 V operation with 0.015 Nmsec/rad damping coefficient. Thus, considering $\omega_n = 143.8$ rad/sec, $V_n = 25$ V and $B_c = 0.015$ Nmsec/rad, the following linearized transfer function was obtained

$$\Delta\omega(s) = \frac{167.8 \Delta V(s)}{s + 47.68} \quad (4-42)$$

Figure 4-41 shows the frequency response of the linearized system. Since the PI controller is responsible for maintaining reference speed, a system with slower response time is required. Thus, a PI controller should be chosen to increase the DC gain to achieve lower steady state error, at the same time maintaining smaller gain at higher frequencies.

Figure 4-42 shows the frequency response of the PI controller with $K_p = 0.1671$ and $K_i = 0.9549$. Transfer function of the PI controller is thus given by

$$\Delta V(s) = \frac{0.1671s + 0.9549}{s} \Delta\omega_{error} \quad (4-43)$$

Frequency response of the combined system is shown in Figure 4-43. The system has a crossover frequency of 4 rad/sec, which is sufficient for the speed control loop.

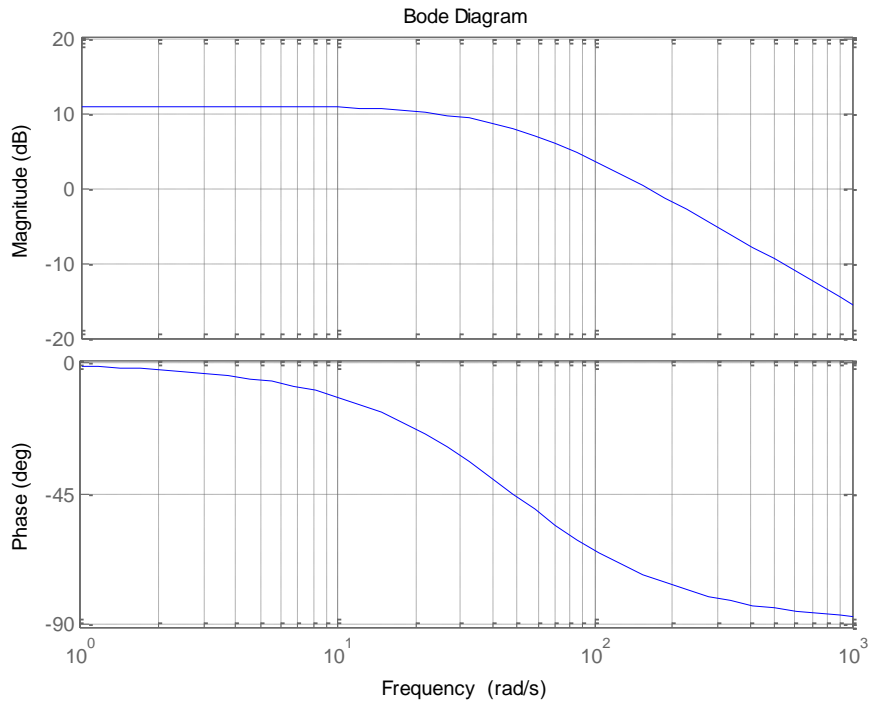


Figure 4-41: Frequency response of the linearized system at $\omega_n = 143.8$ rad/sec and $V_n = 25$ Volt.

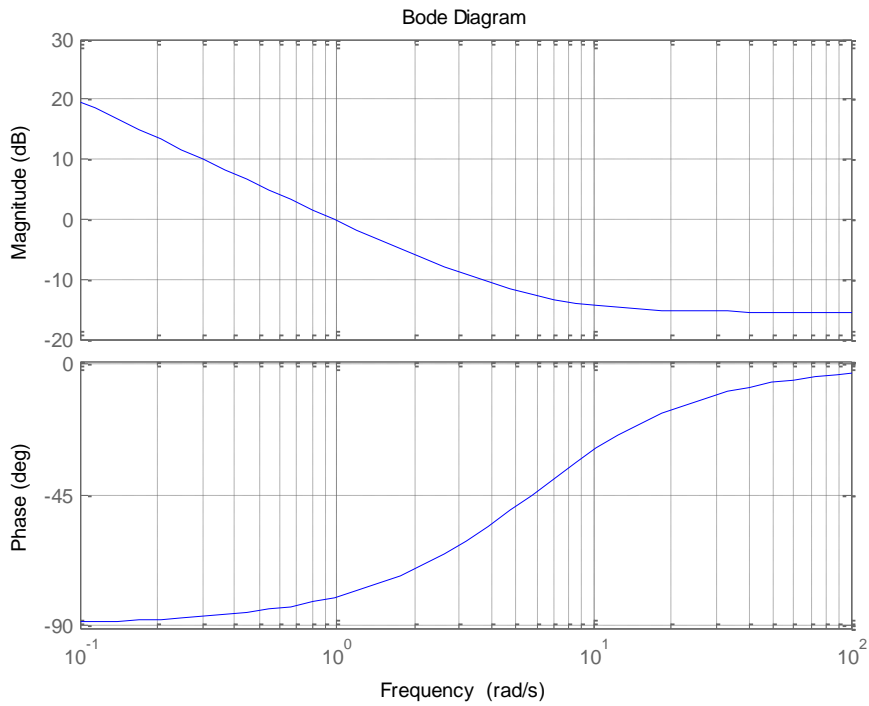


Figure 4-42: Frequency response of the PI controller.

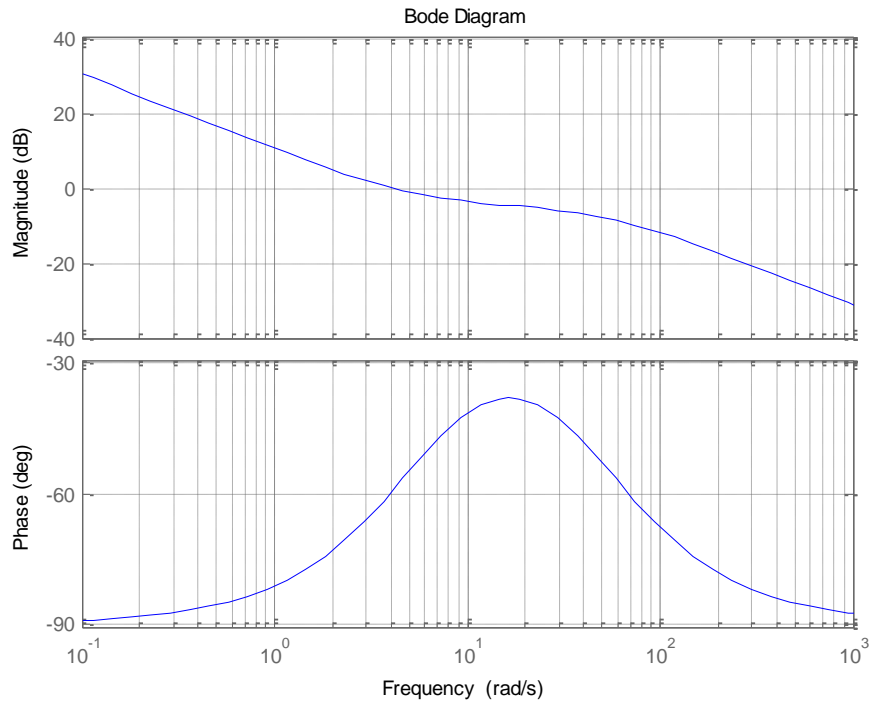


Figure 4-43: Frequency response of the combined system.

4.13. Compensation for Temperature Variation and Estimation Error

Though the procedure described for finding optimum δ considers magnetic saturation, parameter variations due to change in temperature were not included in the modeling. Moreover, the estimation matrix D_M is not ideal and some estimation error is inherent. Magnetic flux linkage Φ_M changes quite a bit with the temperature variation [17][18][19]. Integration of some adaptation in the algorithm would be necessary to improve the performance of the proposed controller.

To compensate for errors, a second block was added to aid in estimating optimum phase advance angle. This block would affect performance only at the steady state after reaching

commanded speed. The basic block diagram for adding the compensation is shown in Figure 4-44.

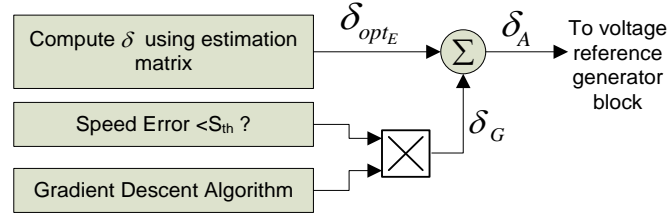


Figure 4-44: Basic block diagram for error compensation.

Since both Figure 4-19 and Figure 4-39 show the DC link power holding a bowl shaped curve for δ variation, it is suitable to use a gradient descent algorithm for finding the minima of the curve [49]. The following equation is implemented to provide adaptation in the MPPA algorithm

$$\delta_G(n) = \delta_G(n - 1) - \gamma \nabla P_{dc}(n - 1) \quad (4-44)$$

where

$$\nabla P_{dc}(n - 1) = \frac{\hat{P}_{dc}(\delta_G(n - 1)) - \hat{P}_{dc}(\delta_G(n - 2))}{\delta_G(n - 1) - \delta_G(n - 2)} \quad (4-45)$$

here, $\hat{P}_{dc}(\delta_G(n - 1))$ = Average DC link input power while $\delta(n - 1)$ was the phase advance angle

This will result in $P_{dc}(\delta_G(n)) < P_{dc}(\delta_G(n - 1))$ when the operation moves towards the bottom of the curve. Successive iteration would bring the operation to the bottom of the curve and δ would oscillate around the optimum point. Calculation of the gradient of the power curve requires a division operation which might result in unacceptably large values. That is why a lower and upper limit was set for the gradient magnitude. In the experiment,

the boundary limits for ∇P_{dc} were set to $[-1 \ 1]$. γ was set to 0.005 which added a small contribution in the applied phase advance angle δ_A shown in Figure 4-44.

4.14. Proposed Control Scheme

Considering all the analytical and experimental discussions, the proposed control scheme can be implemented following some simple steps mentioned below.

- 1) The motor should be connected to the inverter incorporated with necessary sensors for collecting feedback signals. Figure 4-45 shows the connection diagram with the required feedback signals essential for the control scheme.

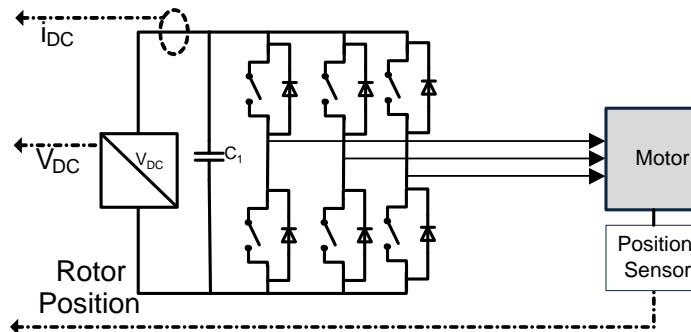


Figure 4-45: Motor connection diagram with necessary feedback signals

- 2) Procedures described in Section 4.7 should be followed. Though several plots have been shown while describing the procedures, the required signals for performing the analysis are the phase advance angle and corresponding DC link input power for different loading conditions (plots shown in Figure 4-14 and Figure 4-18 respectively). Similar plots should be obtained for different operating speeds.

- 3) Some offline analysis of the collected data should be performed. That includes finding the phase advance angle which results in minimum input power at certain loading conditions. Offline analysis and least square estimation would provide the estimation matrix D_M . A PI controller should be designed for generating the voltage magnitude for attaining commanded speed.
- 4) Once the six coefficients of the matrix D_M are obtained, the control scheme can be implemented according to the simple block diagram shown in Figure 4-3. Here, the block responsible for generating the phase advance angle should hold the block shown in Figure 4-44. In this block, δ_{optE} is generated using the computations given in Eqn. 4-25. δ_G is computed using the gradient descent algorithm given in Eqn. 4-45. Since δ_G is multiplied with the speed error checking block (this gives either zero or one as output), the gradient descent algorithm will be effective only at steady state when the actual speed reaches a value close enough to the referred speed.

CHAPTER V

SIMULATION RESULTS

5.1. Overview

In this chapter, the effectiveness of the proposed algorithm is verified at both transient and steady state conditions through simulations. Performance of the control scheme at different temperatures is discussed as well.

5.2. Used Motor Model

As stated earlier, the same motor model as the experimental one was used for simulation. To incorporate direct axis inductance variation, the small droop in L_d was introduced using the following equation

$$L_d(i_q) = L_d(0)(1 - D_{L_d}i_q) \quad (5-1)$$

The value of D_{L_d} was chosen to introduce 10 % droop for 4A of quadrature axis current.

Since the i_d, i_q magnitude depends motor inductances L_q, L_d , trying to solve the system will result in an algebraic loop for the simulation solver. The simulation was performed at high sampling rate (sampling time = 3×10^{-6} second), and this resulted in a small difference between two consecutive samples of current magnitudes. Therefore, L_q, L_d

values computed from the previous sample were taken in all the calculations to avoid an algebraic loop. A small sampling time in simulation would result in a negligibly small difference between two consecutive values of the computed inductances causing minimal error.

5.3. Steady State Performance Analysis

For assessing the motor performance, the motor was operated at a particular speed while a step change in load torque was introduced in two second intervals starting from 0.1 Nm and ending at 0.8 Nm. Though the motor controller only requires DC Link current measurement for computing the input power, three phase currents are used for analyzing the performance of the algorithm in the dq domain. Variations of different quantities during tests are shown in Figure 5-1 through Figure 5-5. To achieve the desired speed command of 900 RPM, motor output torque increased with the application of higher load torque as seen in Figure 5-1. The phase advance angle δ generated by the control scheme is shown in Figure 5-2. Figure 5-3 shows the DC link input power variation with the application of load torque. The dotted lines represent the minimum possible power levels attainable at different load torque levels. Close observation of Figure 5-3 shows successful achievement of desired power levels. i_q, i_d are shown in Figure 5-4 and Figure 5-5 respectively during load variation.

Steady state performance can be better analyzed by examining Figure 5-6 and Figure 5-7. The lines marked by ‘squares’ in both figures present the desired states found by the brute-force search method mentioned in Section 4.7. Figure 5-6 shows successful estimation of

desired phase advance angles (marked by ∇) by the algorithm. The desired and achieved i_d, i_q trajectory is presented in Figure 5-7.

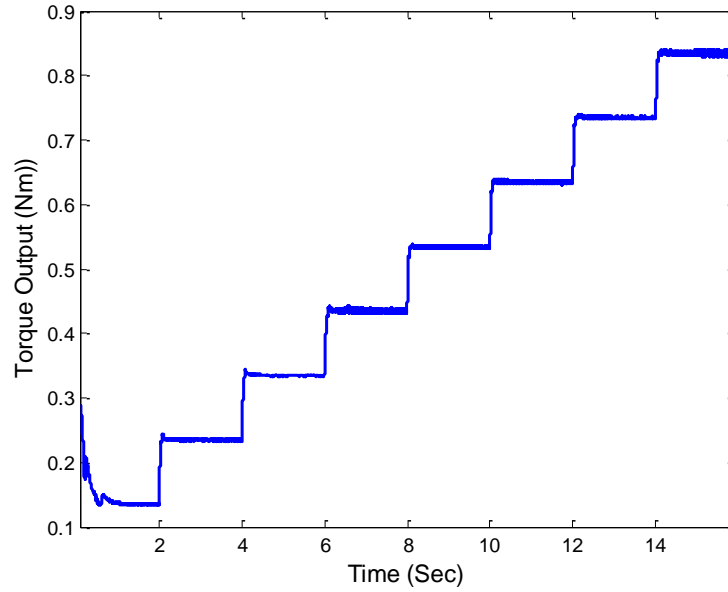


Figure 5-1: Torque output for load torque variation at 900 RPM.

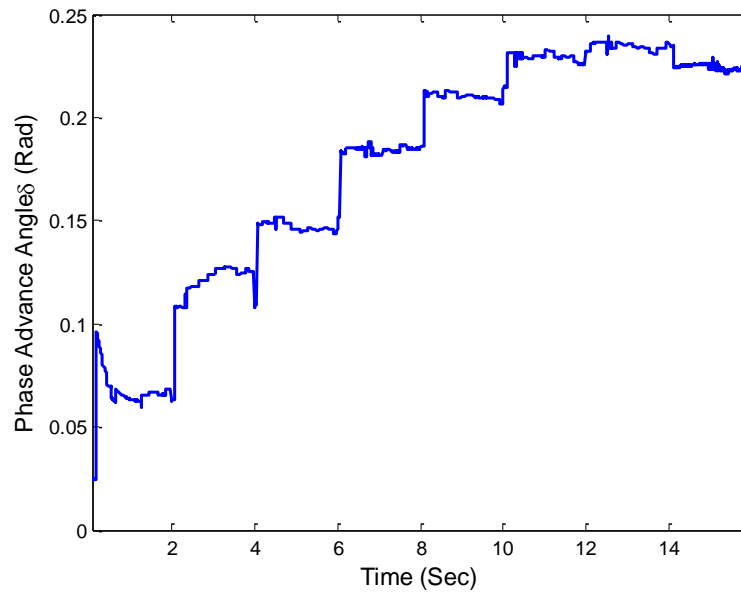


Figure 5-2: Phase advance angle variation with change in load torque at 900 RPM.

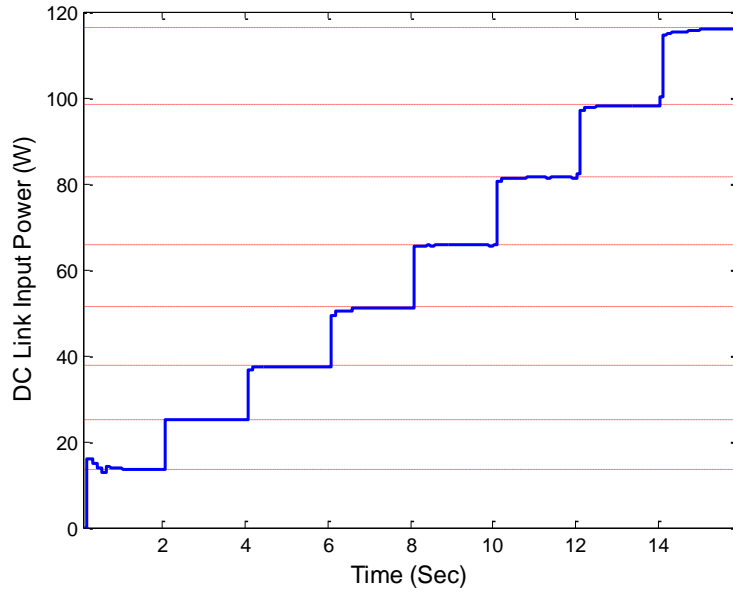


Figure 5-3: DC Link input power variation at 900 RPM while step change in load torque was introduced in steps starting from 0.1 Nm. Dotted lines represent the minimum achievable power computed during motor training.

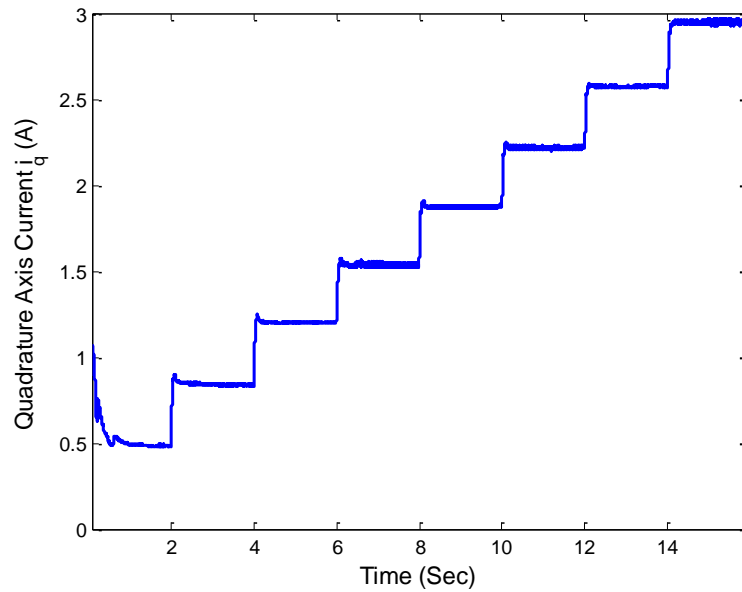


Figure 5-4: Quadrature axis current i_q variation during load variation at 900 RPM (Filtered value is shown).

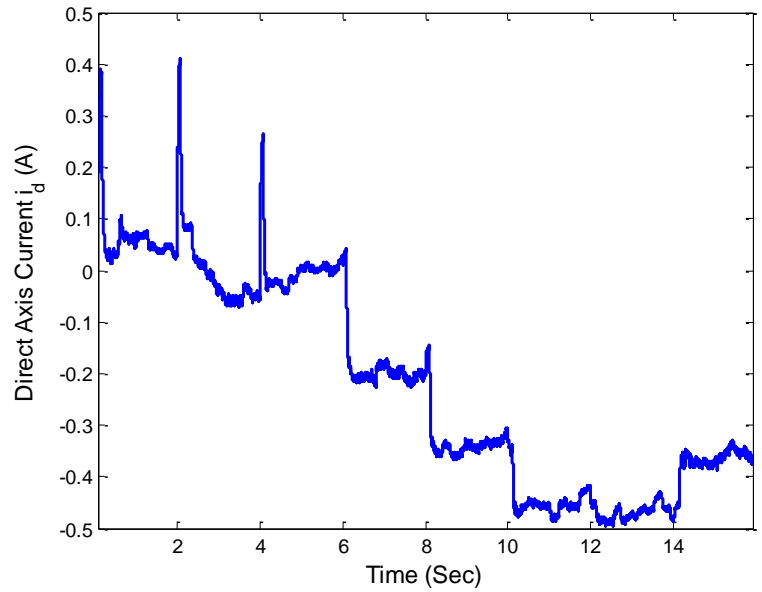


Figure 5-5: Direct axis current i_d variation during load variation at 900 RPM (Filtered value is shown).

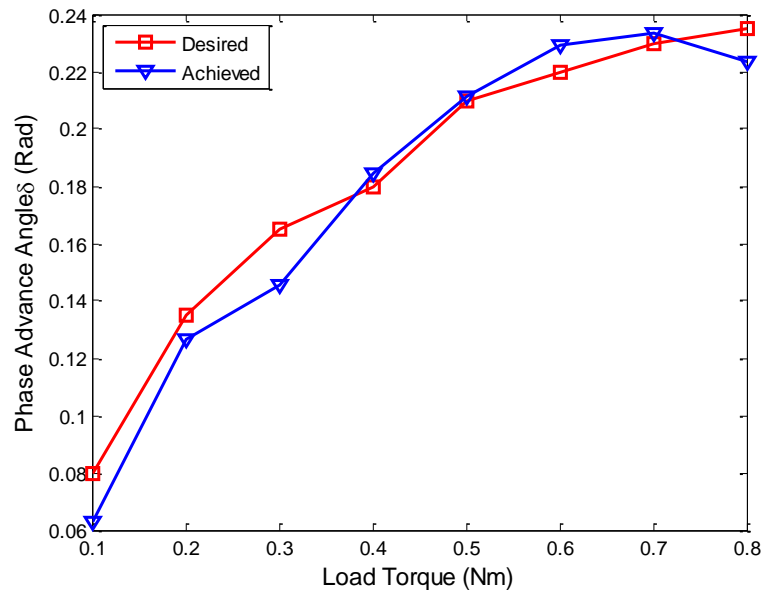


Figure 5-6: Phase advance angle achieved at steady state are marked by ∇ . Angles computed during motor training for generating the D_M matrix are marked by square.

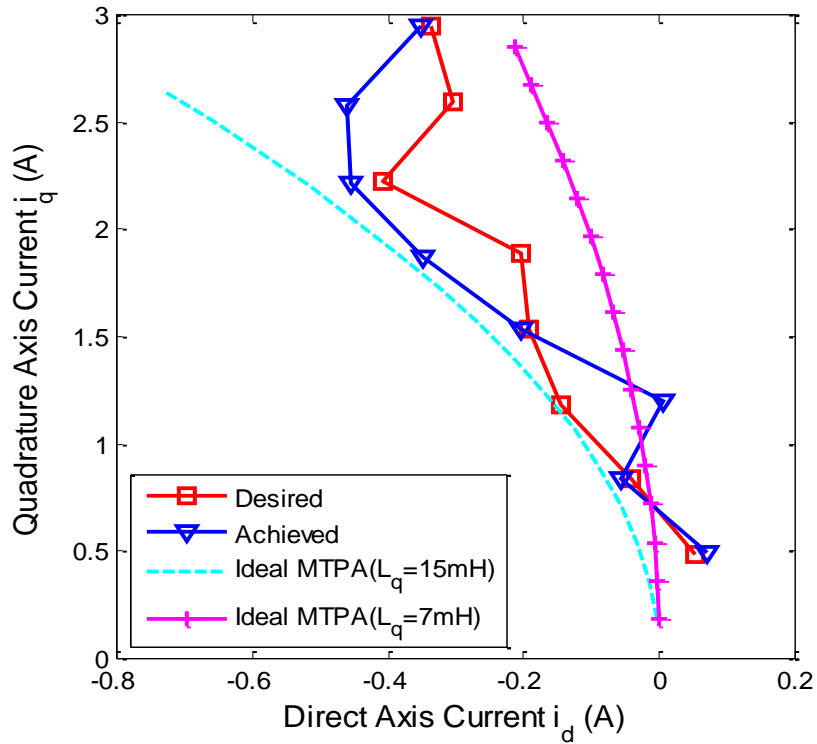


Figure 5-7 : i_d, i_q trajectory obtained by the algorithm is marked by ∇ . Trajectory computed during motor training is marked by square. Two dotted lines show the trajectory computed using constant motor model.

5.4. Temperature Effects

As described in Section 2.6, temperature variation can inflict changes in motor parameters such as conductor resistance and flux linkage. Since temperature was assumed constant while going through the procedure described in Section 4.7, the estimation matrix D_M would be considered ideal only for that particular operating temperature. Since this would not be the situation in the case of a real motor, the perturbation technique based on a gradient descent algorithm described in Section 4.13 was incorporated. To assess the performance of the perturbation algorithm, the motor was later operated with different

parameters computed for higher temperature. The modification made in stator resistance and flux linkage are provided in Table 5-1

Table 5-1 : Motor parameters considered for higher temperature operation

Parameter	Value	Unit
DC Resistance (Line to Neutral)	4.9	Ω
Flux linkage ϕ_M	0.0861	V/rad/sec (considering electrical angular velocity)

To assess the contribution of the perturbation algorithm, the motor was operated at the same speed and loading condition twice. The same estimation matrix D_M (computed at lower temperature) was used for both runs. The first run was made with the usual scheme proposed in Chapter IV (both δ_{optE} and δ_G in Figure 4-44 operating). For the second run, δ_G was forcefully made zero (the gradient descent algorithm was turned off).

The performance of the perturbation algorithm can be observed in Figure 5-8 and Figure 5-9. The red dotted lines in both figures represent the power obtained with the active perturbation algorithm. A closer look at Figure 5-9 reveals that, both approaches produced the same DC link power input during transients since the perturbation was only introduced after achieving steady state. At steady state, the perturbation reduced the DC link input power to the lowest level possible.

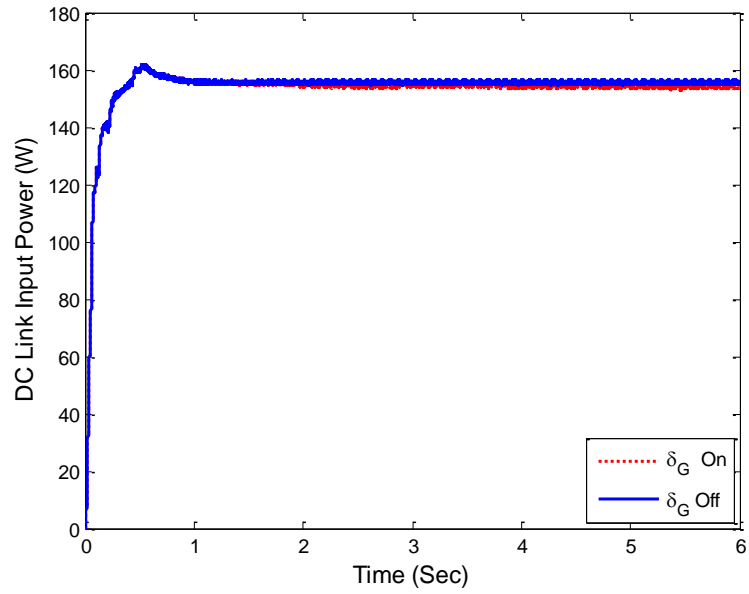


Figure 5-8: DC link input power at 900 RPM with 0.8 Nm load torque.

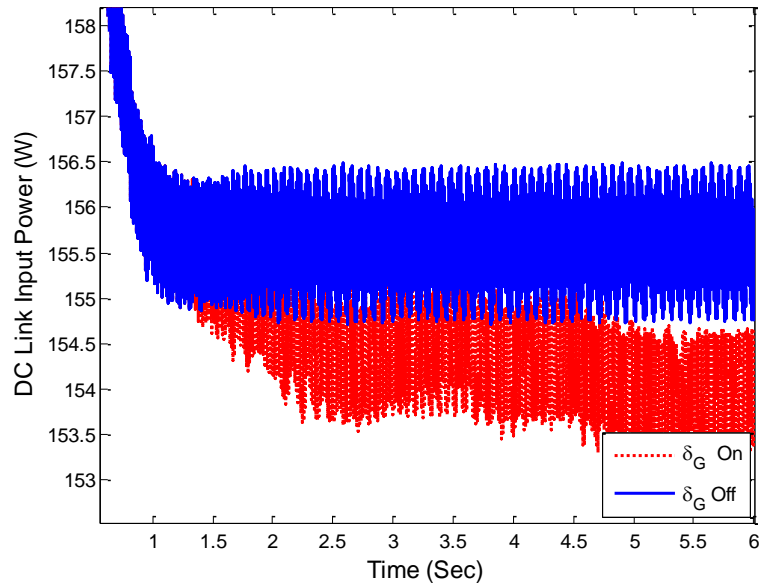


Figure 5-9: DC link input power at 900 RPM with 0.8 Nm load torque at steady state.

Steady state performance based on current trajectory and phase advance angle can be better compared from Figure 5-10 and Figure 5-11. In Figure 5-10, the desired current trajectory computed for higher temperature is marked by 'squares'. This trajectory was only computed for comparison purposes and was not used while forming the estimation matrix D_M . Thus, the motor control block has no idea about this desired trajectory at higher temperature. The trajectories marked by circles and ∇ are the achieved trajectories by the control scheme at higher temperature without and with the aid from gradient descent block respectively. It is found that, for most of the cases, gradient descent helped in achieving operating points closer to the desired coordinates. This is also observed in Figure 5-11, where the phase advance angles marked by ∇ are closer to the angles marked by squares in most of the operating points.

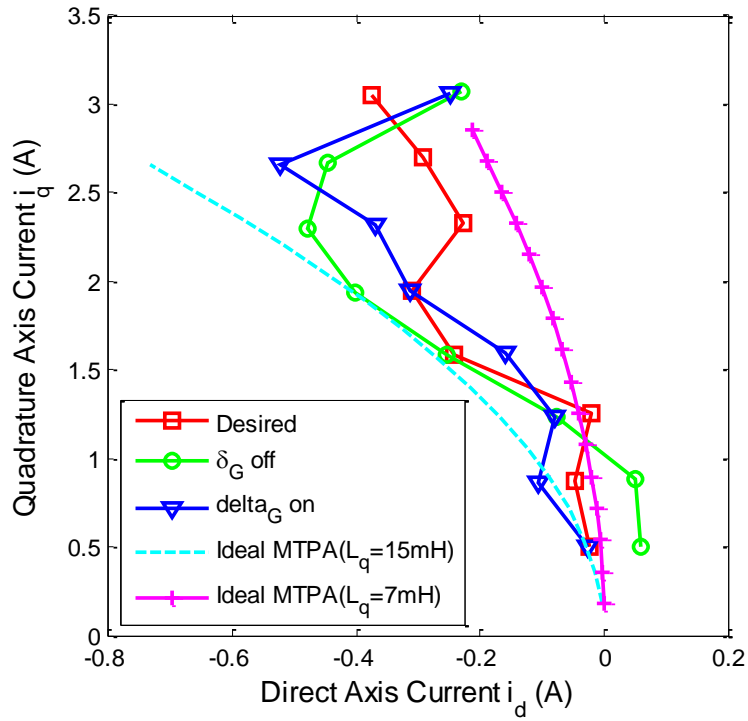


Figure 5-10: i_d, i_q trajectory obtained by the algorithm when perturbation was ‘ON’ is marked by ∇ . Trajectory obtained without the aid of perturbation is marked by circles. Desired trajectory computed for higher temperature is marked by squares.

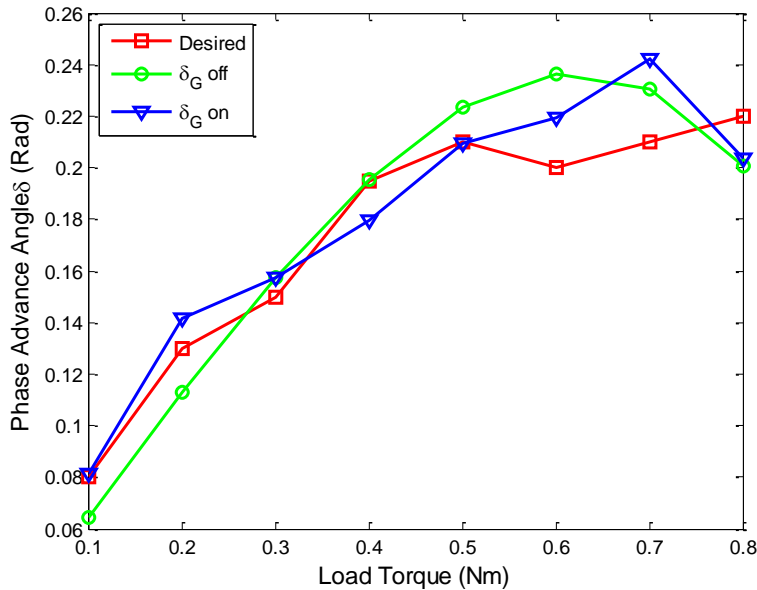


Figure 5-11: Desired phase advance angle at higher temperature is marked by squares. Phase advance angle achieved at steady state with and without the help of perturbation are marked by ∇ and circles respectively.

CHAPTER VI

EXPERIMENTAL IMPLEMENTATION

6.1. Hardware Development

A test platform was prepared to run experiments on different types of motors. The test bench consists of a high power inverter that can be controlled from a standard PC using dSPACE MicroAutobox II. For practical implementation of the control algorithm, an interfacing board was required to link the inverter with the dSPACE system. Necessary protection circuits were incorporated in the interfacing board for the safety of the devices.

6.2. Design of Control Interface

dSPACE allows any control algorithm developed using Matlab Simulink to be implemented on a real system. Installation of dSPACE adds some extra libraries on Simulink library browser. These libraries are equipped with necessary blocks to interface the Simulink program with the dSPACE MicroAutobox II. Figure 6-1 shows the front and rear view of the system. The system is connected to the PC via Ethernet port and communicates using Ethernet TCP/IP protocol. The module has two Zero Insertion Force (ZIF) I/O connectors- DS1511 and DS1512.



Figure 6-1: dSPACE MicroAutobox II, Front and rear view.

In the system, DS1511 was used for controlling the motor. DS1511 has following types of I/O interfaces

- i) Two 16 channel digital output ports
- ii) One 8 channel digital output port
- iii) Two 16 channel digital input ports
- iv) One 8 channel digital input port
- v) One 4 channel analog output port (DAC)

- vi) One 16 channel analog input port (ADC)
- vii) Four Analog trigger pins
- viii) Pins for CAN and serial communication
- ix) Power pins and other pins

6.3. Design of Interface Board

dSPACE is equipped with safety devices in each input and output port. Extra safety measures were taken to protect the system from any possible damage. The interfacing board connects the dSPACE system to the inverter and other input devices. It ensures safety of the equipment and also performs necessary scaling and filtration of the signals. Major parts of the interfacing board are shown on Figure 6-2.

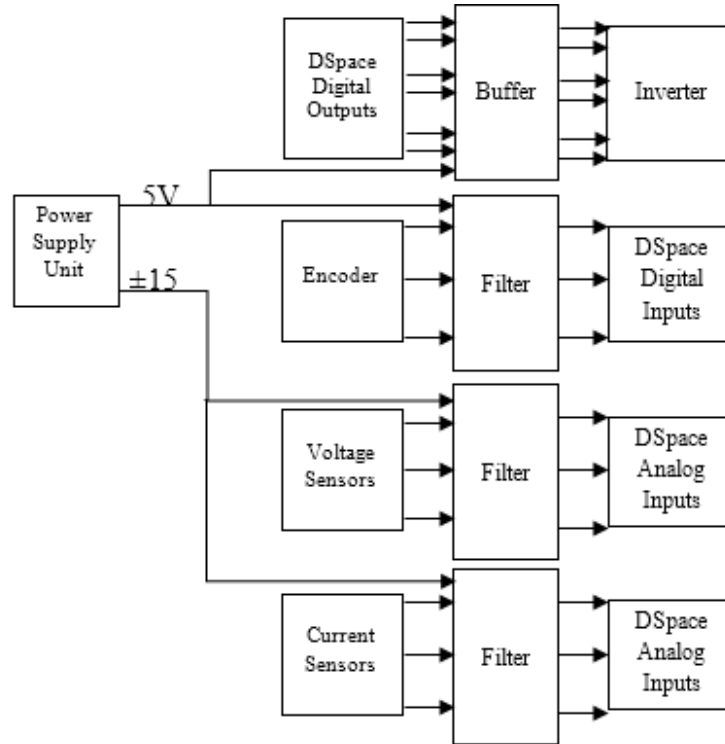


Figure 6-2: Simplified block diagram of the interfacing board (Only major sections are shown).

6.4. Current Conditioning Circuitry

dSPACE analog input pins work only for positive voltage ranging from 0 V to 5 V. LTS15-NP current sensors by LEM were used for measuring currents. They produce 2.5 V at zero current. Voltage can swing +/- 2.5V depending on the current direction. This results in voltage variation between 0 V to 5 V, perfectly usable by dSPACE. To ensure safety and get rid of high frequency measurement error ripple, a simple first order low pass filter (LPF) (shown in Figure 6-3) was used in the interfacing board. The filter contains a simple buffer that eliminates the loading effects of the current sensor output. The buffered signal is passed into the first order LPF with following cut off frequency

$$f_c = \frac{1}{2\pi RC} \quad (6-1)$$

with $R = 31.8 \Omega$ and $C = 0.1 \mu F$ $f_c = 50kHz$

This filter caused negligible delay and removed high frequency spikes from the measured currents.

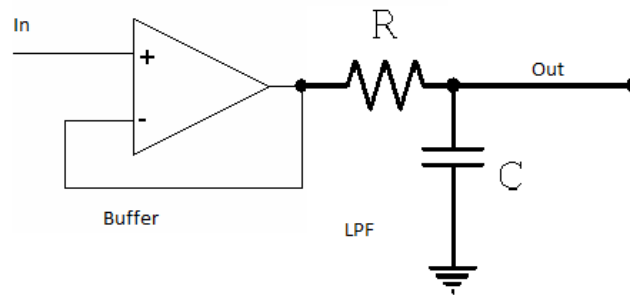


Figure 6-3: First order low pass filter.

6.5. Implementation of Position Decoding and Conditioning

A 10 bit optical encoder attached with the motor was used for position decoding of the PMSM. The optical encoder output contains rectangular pulses containing higher frequency components compared to current signals. Encoder outputs may contain high frequency spikes and filtration is needed to protect the controller from unwanted voltage spikes. A low pass Butterworth filter shown in Figure 6-4 was used to filter the encoder outputs. This filter has the following transfer function

$$H(s) = \frac{1}{1 + C_2(R_1 + R_2)s + R_1R_2C_1C_2} \quad (6-2)$$

The following values were used in the circuit

$$R_1 = 28.0 \text{ k}\Omega \quad R_2 = 10.0 \text{ k}\Omega \quad C_1 = 22 \text{ pF} \quad C_2 = 470 \text{ pF}$$

This resulted in a cut off frequency of 89.2 kHz

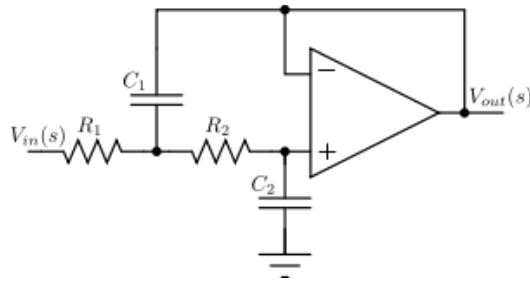


Figure 6-4: Butterworth filter used for encoder and voltage sensor output filtration.

6.6. Shoot Through Protection

The dSPACE MicroAutobox is equipped with its own shoot through protection technique. System blocks used to deliver PWM signals to the output ports have an adjustable shoot

through protection scheme. By controlling the dead time, MicroAutobox is supposed to deliver a clean PWM signal. Due to connection noise, line delay and other factors, shoot through may appear. To protect the inverter from high current and potential damage, a hardware shoot through prevention circuit was incorporated in the interfacing board.

For all the digital outputs from dSPACE, a three state buffer was used. This buffer has an enable pin that ensures 3 state operation. Output pins can be set to a high impedance state by disabling the buffer. The enable pin of the buffer is controlled by the shoot through detection circuit and the buffer stops sending PWM signals to the inverter when shoot through is detected. Figure 6-5 shows the simple logic circuit that sends the enable signal to the buffer circuit. The buffer enable pin is an active low pin and the buffer stops sending signals at its output when this pin is high, either due to shoot through effects or by the 'Enable' control pin from dSPACE.

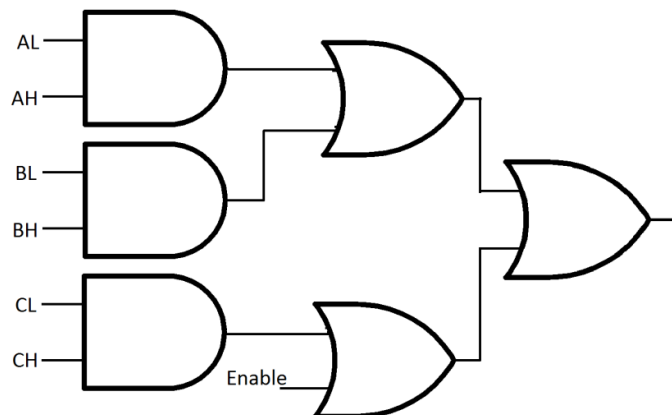


Figure 6-5: Shoot through protection circuit.

6.7. Experimental Setup

The experimental motor is coupled with a Magtrol hysteresis dynamometer for loaded tests. The dynamometer is controlled using Magtrol DSP6000 dynamometer controller. dSPACE Control Desk 3.7.4 was used for control and data acquisition purpose. The experimental setup is shown in Figure 6-6.

Table 6-1: Experimental implementation details

DC bus voltage	90 Volt
Inverter switching frequency	20 kHz
Control scheme sampling time	20 kHz
Dead time (Shoot through protection)	0.1 μ Sec

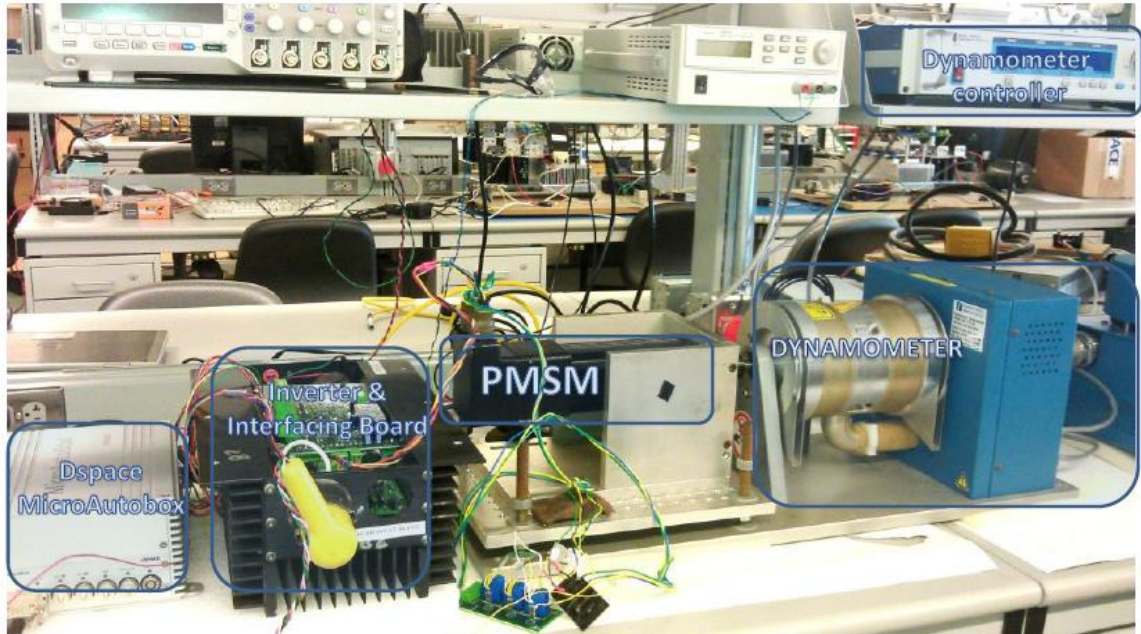


Figure 6-6: Experimental Setup

6.8. Implementation of Space Vector Modulation

Considering the 3-phase circuit model for PMSM shown in Figure 2-4, it is evident that a 3-phase voltage must be applied to the stator to operate the motor. Though the ideal motor model suggests applying a 3-phase ideal sinusoidal voltage to the stator terminals, it is most of the time not possible to generate an exact sinusoidal voltage with variable frequency. Thus, a convenient PWM (pulse width modulation) [50] technique must be adopted that can generate necessary PWM signals which drive the inverter to replicate ideal sinusoidal voltages at the stator terminals.

For properly applying the reference voltage to the stator terminals, two different types of modulation schemes are available to implement on the 3-phase 6 switch inverters. The simplest approach is to use the sinusoidal PWM (SPWM) [51] technique which is simple and can be used with lower computational cost. But limited magnitude of the DC bus voltage also limits the available voltage that can be applied to the stator terminal. This in turns leads to a more complex technique called Space Vector Modulation (SVM) [51][50]. SVM has higher efficiency in utilizing the available DC voltage. Figure 6-7 shows the basic block diagram for motor control using the Voltage Source Inverter (VSI) with the SVM technique.

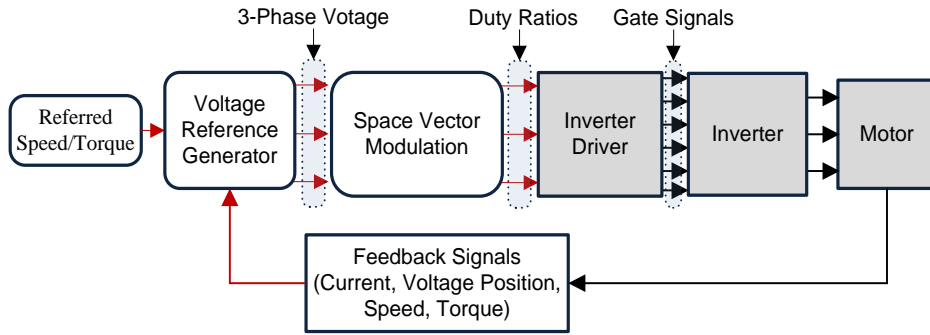


Figure 6-7: Basic block diagram for motor control using Space Vector Modulation for voltage regulation.

Figure 6-8 shows the detailed block diagram for implementing SVM. To compute necessary duty ratios for the three legs of the inverter, voltages are first converted into the $\alpha\beta$ reference frame as shown in the block diagram. In the $\alpha\beta$ reference frame, a 3-phase voltage can be represented by only one voltage vector V_M rotating counter clockwise at a frequency exactly equal to the frequency of the 3-phase voltage.

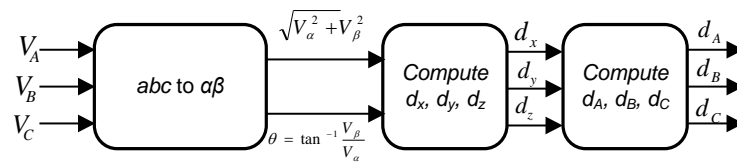


Figure 6-8: Space Vector Modulation Implementation.

The SVM technique can be better understood from Figure 6-9. On-off conditions of the six switches in a 3-phase inverter result in 8 possible outcomes at the output voltage. Turning off the three top switches or the three bottom switches results in zero voltage at the VSI output and is marked by V_0 and V_7 in Figure 6-9. The other six possible outputs are represented by six vectors shown in the diagram. Any desired voltage in between these vectors can be generated by combining these six vectors in a suitable manner provided that the desired voltage falls within the dotted circle. This dotted circle represents the maximum

possible voltage magnitude achievable and is equal to $\frac{1}{\sqrt{3}}$ times the available DC bus voltage at the inverter.

All the vectors shown in Figure 6-9 represent particular switching states. To achieve a particular voltage phasor, appropriate duty ratios for the inverter switches must be calculated. To reduce switching losses, it is desirable to operate the inverter with minimum possible switching. Minimum Loss Space Vector Pulse Width Modulation (MLSVPWM)

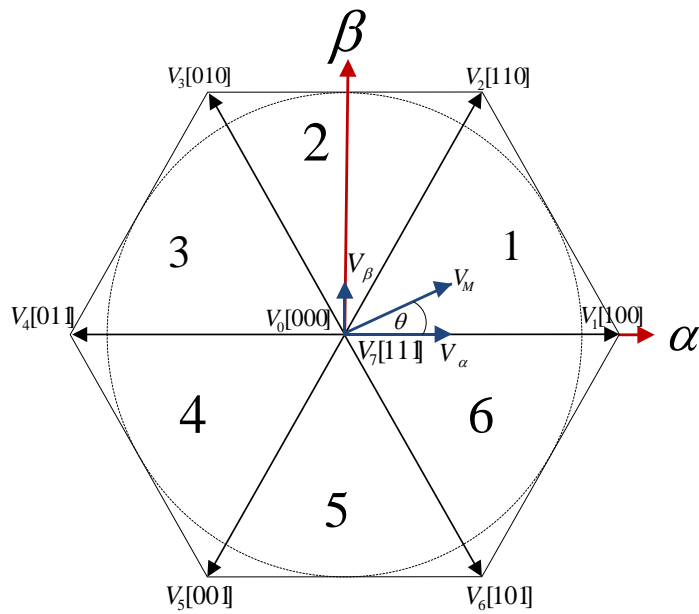


Figure 6-9: Voltage vectors in $\alpha\beta$ reference frame.

was proposed [52] to generate the required voltage with minimum possible switching.

Necessary duty ratios can be found using following equations [53][54]

$$d_x = \frac{V_M \sin(60^\circ - \theta)}{\sqrt{\frac{2}{3}} V_{dc} \sin(60^\circ)} \quad (6-3)$$

$$d_y = \frac{V_M \sin(\theta)}{\sqrt{\frac{2}{3}} V_{dc} \sin(60^\circ)} \quad (6-4)$$

$$d_z = 1 - d_x - d_y \quad (6-5)$$

Duty ratios for 3 inverter legs are chosen in such a way that, for each sector, any two of the six switches remains either completely turned on or completely turned off. Table 6-2 shows the duty ratios for the upper switches of the three legs. To reduce switching losses, the upper switch for phase A is completely turned on at sector 1 and completely turned off at sector 4.

Table 6-2: Duty ratios for different switches

Sector	dA	dB	dC
1	1	$dz + dy$	dz
2	dx	$dx + dy$	0
3	dz	1	$dy + dz$
4	0	dx	$dx + dy$
5	$dz + dy$	dz	1
6	$dx + dy$	0	dx

Figure 6-10 and Figure 6-11 show the performance of MLSVPWM for a 3 phase 50 Hz voltage reference. As anticipated, the duty ratio for each phase becomes either 0 or 1 once in every cycle indicating complete turn off or turn on of the respective switches.

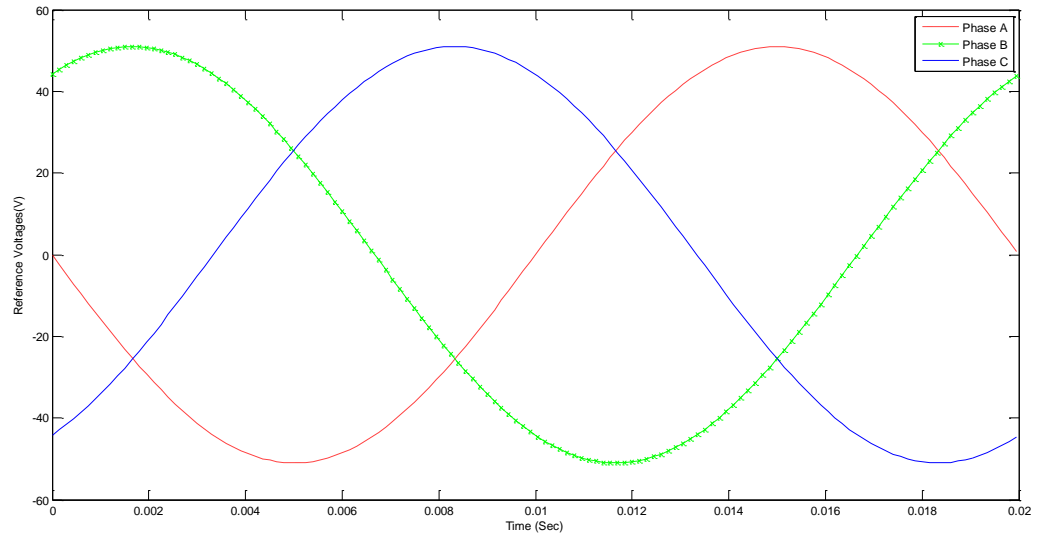


Figure 6-10: 3-phase 50 Hz reference voltage V_a, V_b, V_c .

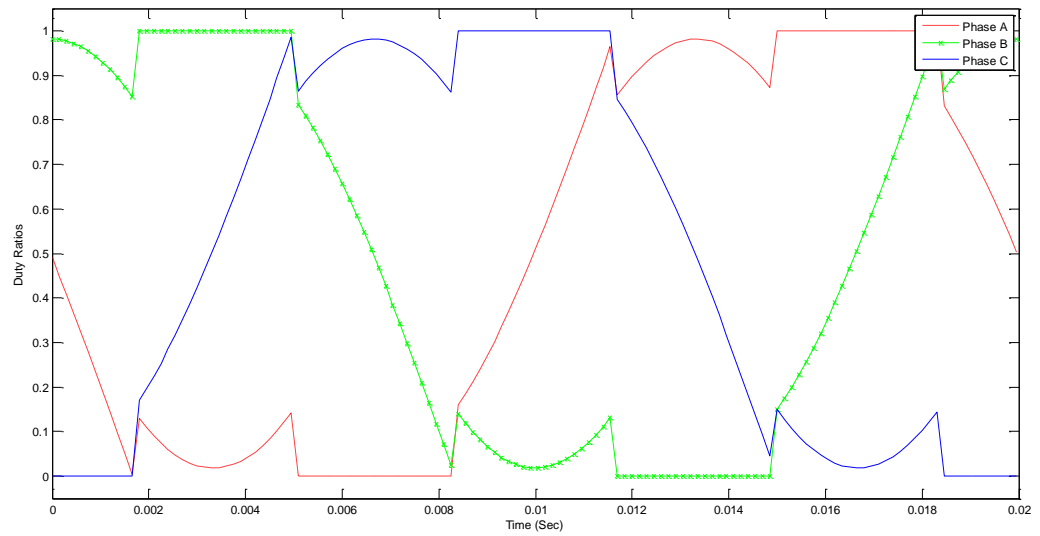


Figure 6-11: Duty ratios for inverter upper switches.

CHAPTER VII

EXPERIMENTAL RESULTS

7.1. Overview

The proposed algorithm was implemented on a Kollmorgen Goldline motor using the hardware described in Chapter VI. Steady state and dynamic performance of the experimental motor is described throughout this chapter. Numerical values of different parameters used in the control scheme are provided as well.

7.2. Primary Data Collection

The motor was first operated according to the procedures described in Section 4.7. After getting necessary data, the estimation matrix was obtained by applying the least square estimation technique described in Section 4.10. The procedure was not performed for constant temperature. Thus, the estimation matrix is not expected to perform exactly like the simulation where the model assumes constant resistance and flux linkage. The motor was operated at six different speeds in 100 RPM intervals between 600 RPM to 1100 RPM. At each speed, the load torque was varied by 0.1 Nm between no load conditions to 0.8 Nm. The collected data is presented in Table 7-1. The speed, minimum DC link input power and optimum δ are necessary to get the coefficients for the controller. The other parameters

are taken only for analysis and comparison. The MTPA trajectories obtained from Table 7-1 data are shown in Figure 7-1.

After performing the least square estimation, the following matrix D_M was found for estimating δ

$$D_M = \begin{bmatrix} 2.2983 \times 10^{-4} & -3.4210 \times 10^{-6} & 1.4910 \times 10^{-8} \\ -1.5058e \times 10^{-6} & 2.4902 \times 10^{-8} & -1.1299 \times 10^{-10} \end{bmatrix}$$

For applying the perturbation technique for error compensation through the gradient descent algorithm, the γ value in Eqn. 4-44 was set to 0.005. The upper and lower limit of the calculated gradient value ∇P_{dc} were set to unity in both directions. An upper and lower limit was also set for the phase advance angle generated using the graduated descent. The limit was set to [-0.05 0.05] to limit the contribution of the perturbation algorithm.

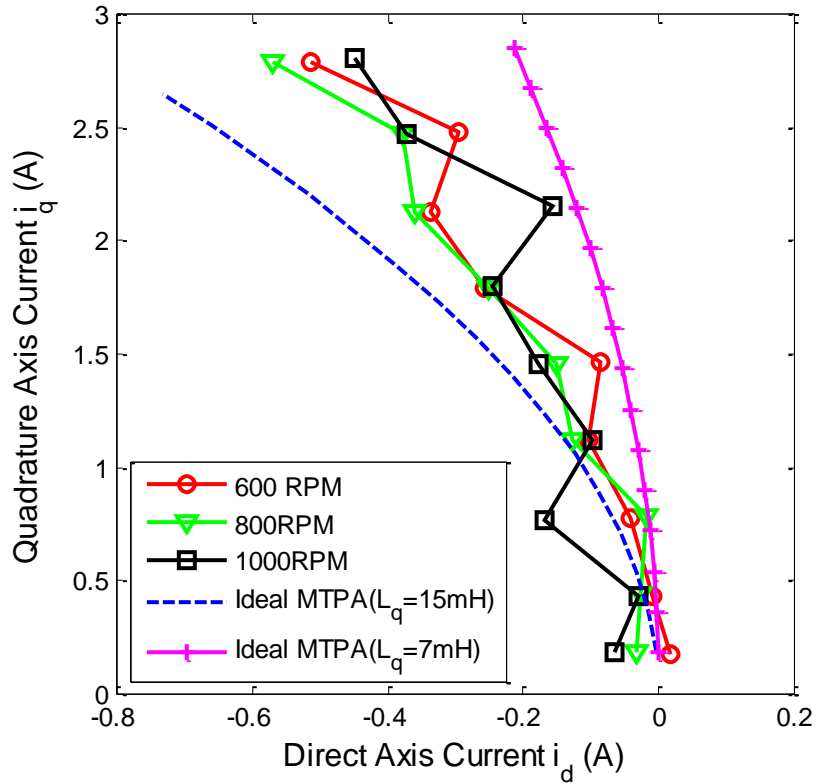


Figure 7-1: i_d, i_q trajectories at different speeds computed from data obtained following the procedures described in Section 4.7. Two dotted lines show the trajectories computed using constant motor model.

Table 7-1: Data obtained from procedure described in Section 4.7

Mechanical Speed (RPM)	Torque (Nm)	Minimum DC Link Input Power (W)	Optimum Phase Advance Angle δ_{opt}	Quadrature Axis Current i_q (A)	Direct Axis Current i_d (A)	Terminal Voltage Magnitude v_m (V)
600	0.03	6.912	0.039	0.173	0.0162	12.2191
	0.1	12.249	0.063	0.4296	-0.0085	16.286
	0.2	20.25	0.084	0.7751	-0.0417	16.4685
	0.3	28.728	0.114	1.1176	-0.1028	16.737
	0.4	37.629	0.126	1.4657	-0.0872	17.0399
	0.5	47.565	0.169	1.7937	-0.2579	17.3378
	0.6	57.906	0.19	2.1247	-0.3383	17.6971
	0.7	68.967	0.19	2.4781	-0.2962	18.1713
	0.8	80.847	0.224	2.7935	-0.5128	18.7015

700	0.03	7.38	0.057	0.1776	-0.0425	16.4148
	0.1	13.131	0.055	0.4238	-0.0063	16.7896
	0.2	22.032	0.096	0.7679	-0.0846	17.2939
	0.3	32.085	0.129	1.1194	-0.1715	17.7502
	0.4	42.516	0.138	1.4654	-0.1572	18.2467
	0.5	53.847	0.158	1.8036	-0.2074	20.729
	0.6	64.782	0.186	2.1304	-0.3175	22.746
	0.7	76.311	0.221	2.454	-0.4572	22.813
	0.8	89.199	0.21	2.8196	-0.3298	22.97
800	0.03	8.037	0.057	0.1834	-0.0322	17.1423
	0.1	14.427	0.063	0.4352	-0.0286	17.9486
	0.2	24.921	0.082	0.7847	-0.0175	19.6427
	0.3	35.919	0.122	1.1186	-0.1262	22.7478
	0.4	46.989	0.144	1.4581	-0.1503	22.8341
	0.5	58.959	0.175	1.7935	-0.2512	23.0035
	0.6	71.586	0.2	2.1263	-0.3593	23.2414
	0.7	84.735	0.211	2.4702	-0.3785	23.5841
	0.8	98.595	0.242	2.7877	-0.5689	23.9465
900	0.03	8.415	0.064	0.1851	-0.0622	18.5461
	0.1	15.921	0.056	0.4383	0.0341	22.7735
	0.2	27.054	0.092	0.7774	-0.0419	22.9925
	0.3	38.79	0.131	1.1106	-0.1631	23.294
	0.4	51.264	0.15	1.4545	-0.1998	23.6973
	0.5	64.458	0.168	1.8018	-0.2309	24.1281
	0.6	78.156	0.194	2.133	-0.3329	24.5554
	0.7	92.799	0.216	2.4681	-0.4254	25.0888
	0.8	108.099	0.235	2.8031	-0.5005	25.8235
1000	0.03	8.037	0.07	0.1773	-0.0646	22.8465
	0.1	16.398	0.072	0.4258	-0.0289	23.123
	0.2	28.71	0.124	0.7612	-0.1675	23.6003
	0.3	41.58	0.125	1.1199	-0.0983	24.2519
	0.4	54.972	0.149	1.4583	-0.1789	24.912
	0.5	69.201	0.17	1.7979	-0.2442	25.6732
	0.6	84.321	0.176	2.1551	-0.1572	29.2253
	0.7	99.126	0.215	2.4722	-0.3717	29.2666
	0.8	115.191	0.239	2.8079	-0.4495	29.3988
1100	0.0547	9.234	0.071	0.1939	-0.0592	23.5786
	0.1	17.712	0.084	0.4294	-0.0413	24.4479
	0.2	30.933	0.102	0.7725	-0.0846	25.4095
	0.3	44.946	0.168	1.0874	-0.3773	26.0444
	0.4	59.265	0.137	1.4732	-0.0094	29.268

	0.5	74.106	0.201	1.7749	-0.3687	29.364
	0.6	90.153	0.215	2.1262	-0.3785	29.5862
	0.7	106.695	0.25	2.4359	-0.6073	29.8402
	0.8	124.164	0.245	2.8075	-0.4752	30.3624

7.3. Load Torque Variation at Constant Speed

For assessing the performance of the algorithm, step changes in load torque was introduced. Performance of the algorithm at 800 RPM operating speed while application of step load changes is presented through Figure 7-2 to Figure 7-11. Torque generated by the motor was estimated using the measured currents and motor parameters. While computing the reluctance torque, Eqn. 4-18 was used to estimate quadrature axis inductance L_q . Figure 7-2 shows the estimated torque generated by the motor. Since the speed was kept constant, the generated torque is supposed to have a constant value for a particular loading condition. This phenomenon is reflected in Figure 7-2, which ensures proper torque estimation. In the plots, filtered values of currents are used.

The phase advance angle introduced in the voltage is shown in Figure 7-3, whereas the contribution of the gradient descent algorithm for generating the angle is shown in Figure 7-4.

The solid line in Figure 7-5 shows the DC link input power to the inverter, whereas the dotted lines present the minimum achievable power found using the brute force searching technique. These are also the power levels indicated in Table 7-1. It seemed strange that, for most of the torque levels, the power levels achieved by the controller were found to be smaller than the minimum levels given in Table 7-1. The reason behind this can be the

change in stator resistance with temperature. While going through procedures described in Section 4.7, running the motor for long duration can significantly increase temperature.

i_q and i_d during load variation are presented in Figure 7-6 and Figure 7-7 respectively. The generated voltage by the PI controller to attain commanded speed is shown in Figure 7-8. Figure 7-9 shows the speed response of the motor with the application of load torque.

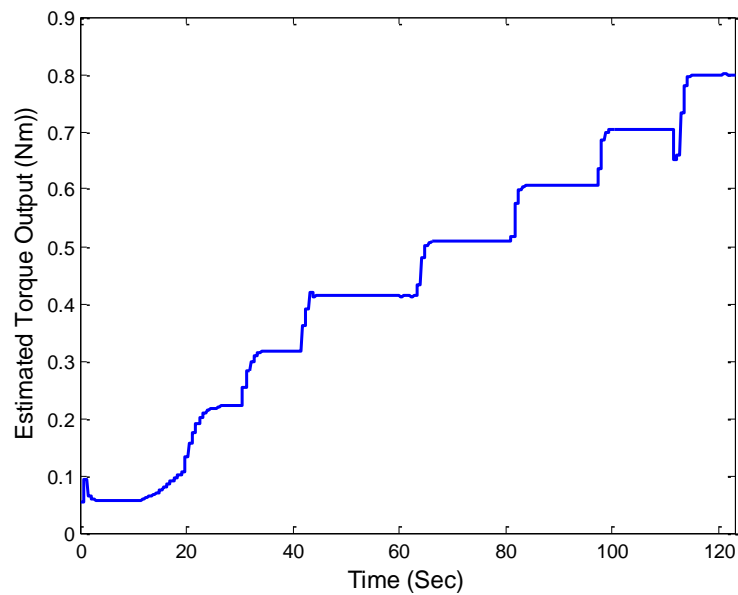


Figure 7-2: Estimated Torque Output for load torque variation at 800 RPM.

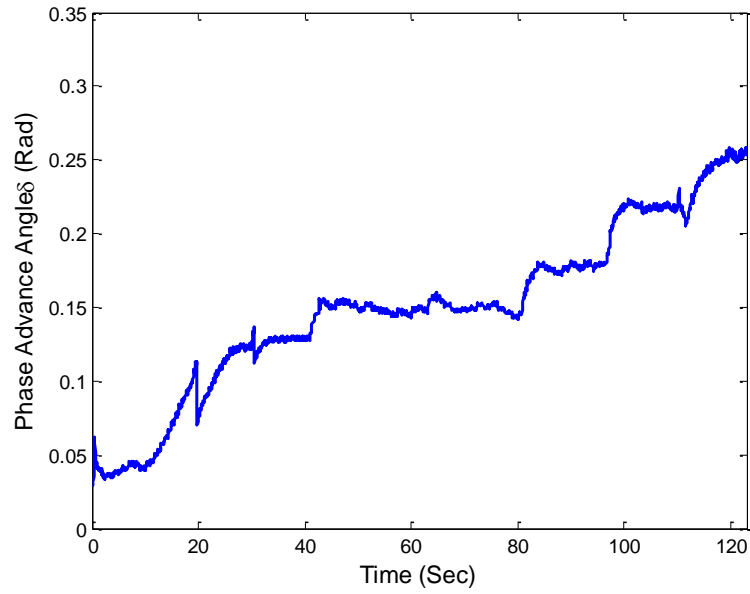


Figure 7-3: Phase advance angle variation with change in load torque at 800 RPM.

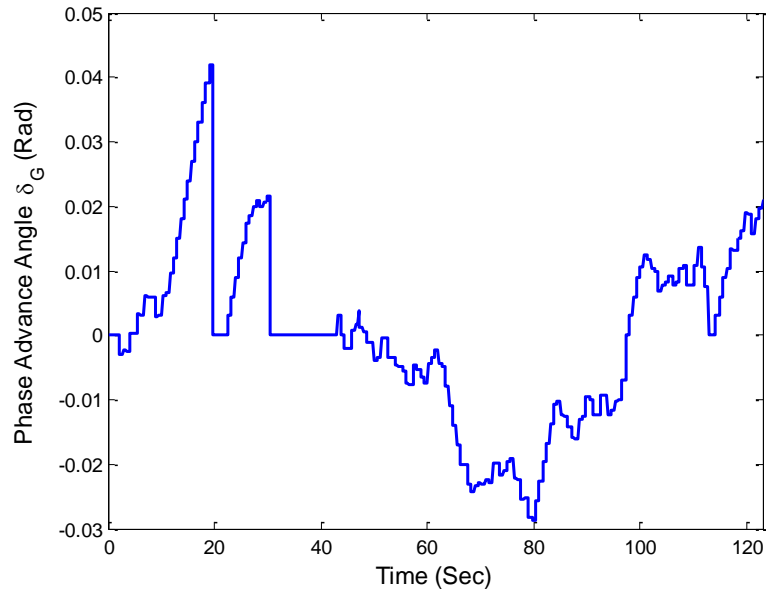


Figure 7-4: Contribution of phase advance angle variation from perturbation algorithm at 800 RPM.

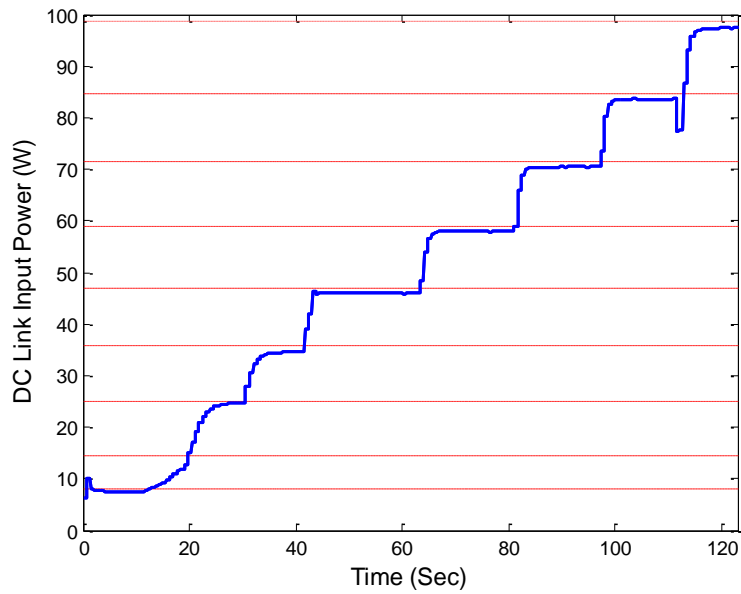


Figure 7-5: DC Link input power at 800 RPM while step change in load torque was introduced starting from 0.1Nm. Dotted lines represent the minimum achievable power levels computed during motor training.

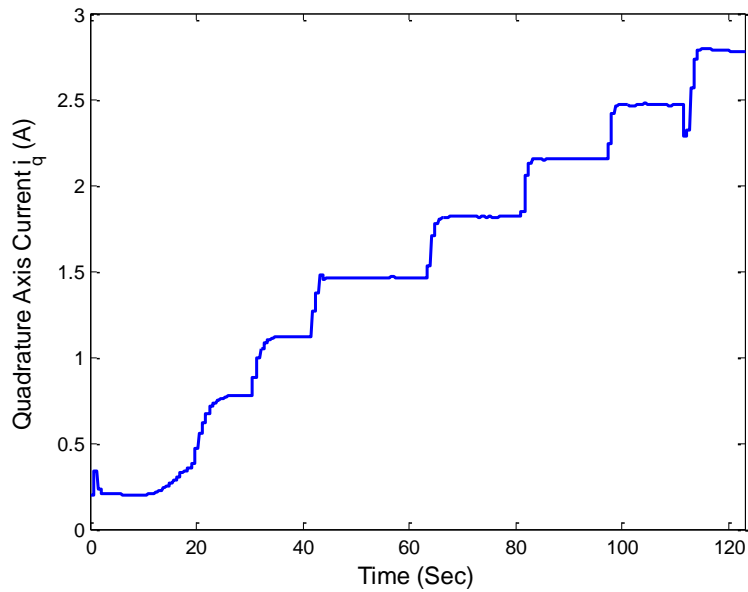


Figure 7-6: Quadrature axis current i_q during load variation at 800 RPM (Filtered value is shown).

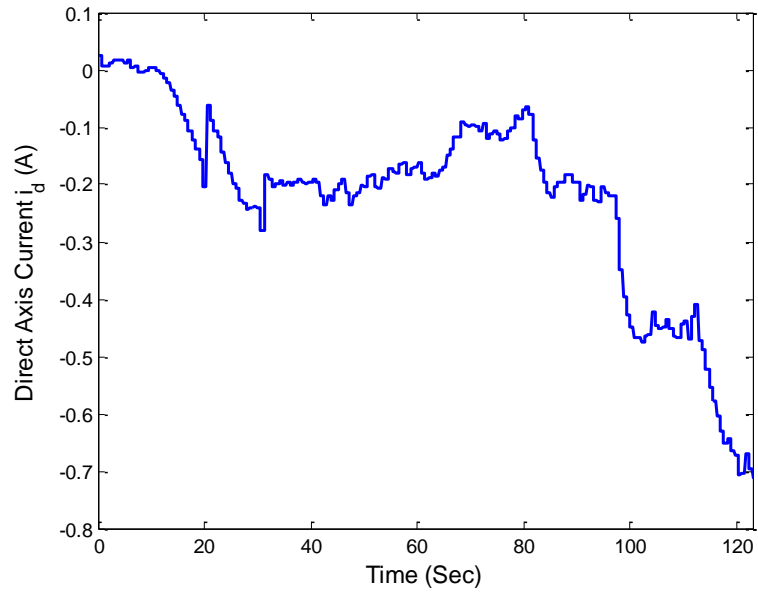


Figure 7-7: Direct axis current i_d during load variation at 800 RPM (Filtered value is shown).

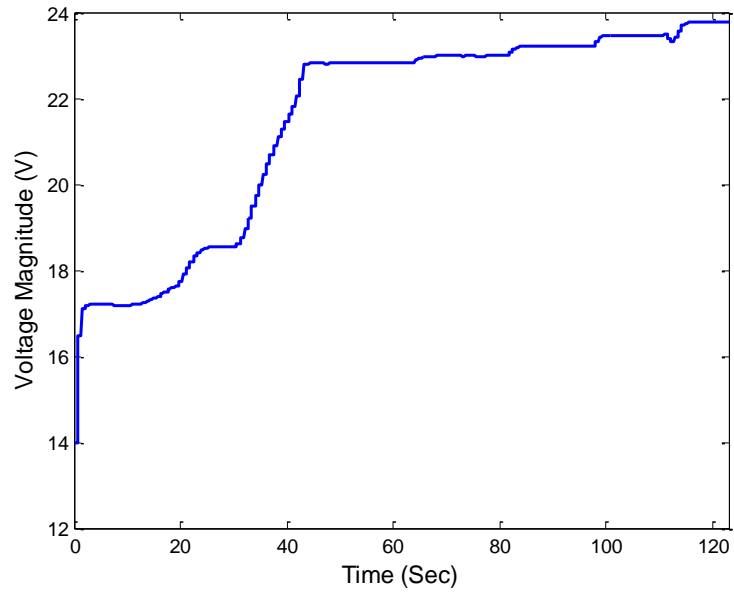


Figure 7-8 : Voltage magnitude during load variation at 800 RPM (Filtered value is shown).

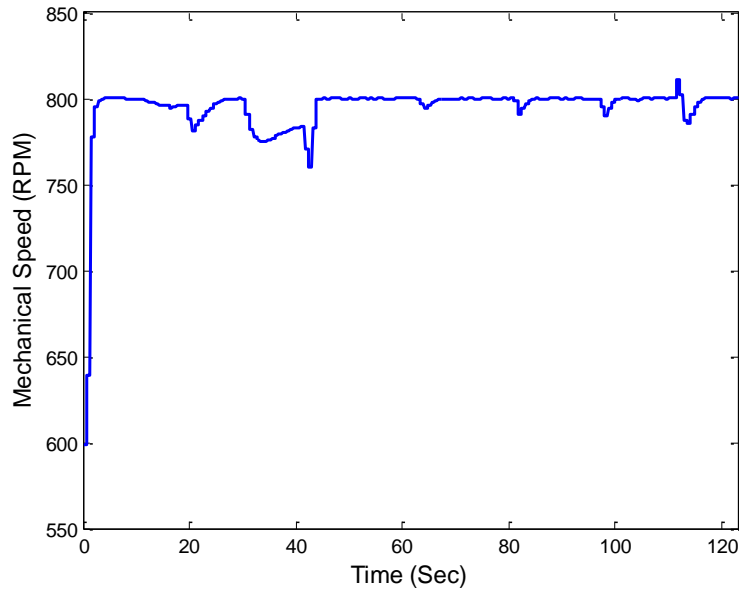


Figure 7-9: Speed Response of the motor with the application of load variation.

The steady state response of the motor can be better analyzed by observing Figure 7-10 and Figure 7-11. In Figure 7-10, the line marked by ∇ shows phase advance angle generated by the algorithm at different loading conditions. These values were computed by taking a time average of the phase advance angle shown in Figure 7-3 after achieving steady state at different torque levels. The line marked by ‘squares’ presents the optimum angles and can be found in Table 7-1. Figure 7-11 shows the i_d, i_q trajectory computed from steady state data with the same markings as shown in Figure 7-10.

As stated earlier, larger phase advance angles caused larger d -axis currents on negative axis. That phenomenon can be observed by analyzing Figure 7-10 and Figure 7-11. At 0.2 Nm load torque, the estimated phase advance angle is significantly larger than the desired angle. This effectively caused larger i_d and moved the i_q, i_d trajectory towards the left of

the desired trajectory. The opposite scenario is observed at 0.5 Nm and 0.6 Nm load torque levels.

Though the trajectories obtained during motor training using the brute force search technique are marked as desired trajectories in the figures, essentially this should not be the most appropriate term. The changing operating temperature shifts the desired trajectory and thus it should be a function of temperature as well.

Similar steady state analysis for the 700 RPM operating speed is shown in Figure 7-12 and Figure 7-13. For this speed as well, the estimation matrix aided by the gradient descent perturbation algorithm succeeded in generating a phase advance angle close to the optimum one.

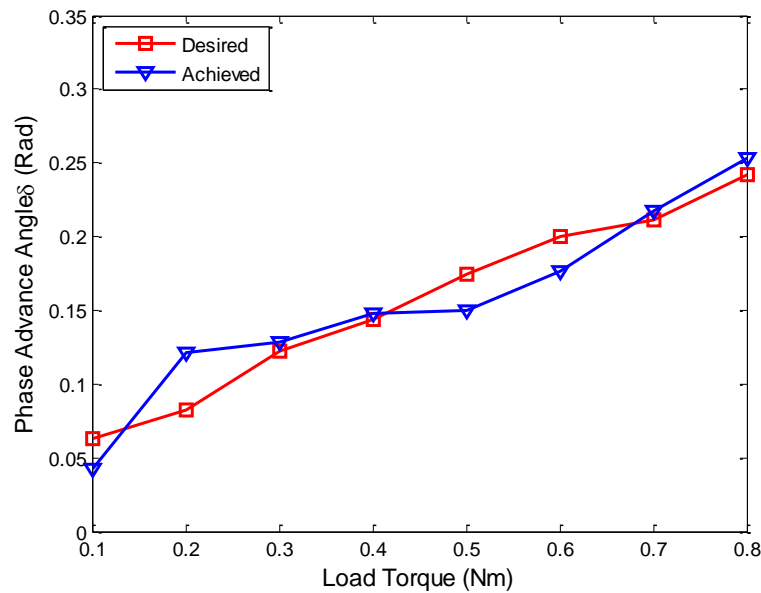


Figure 7-10: Phase advance angles achieved at steady state for 800 RPM are marked by ∇ . Angles computed during motor training for generating the D_M matrix are marked by squares.

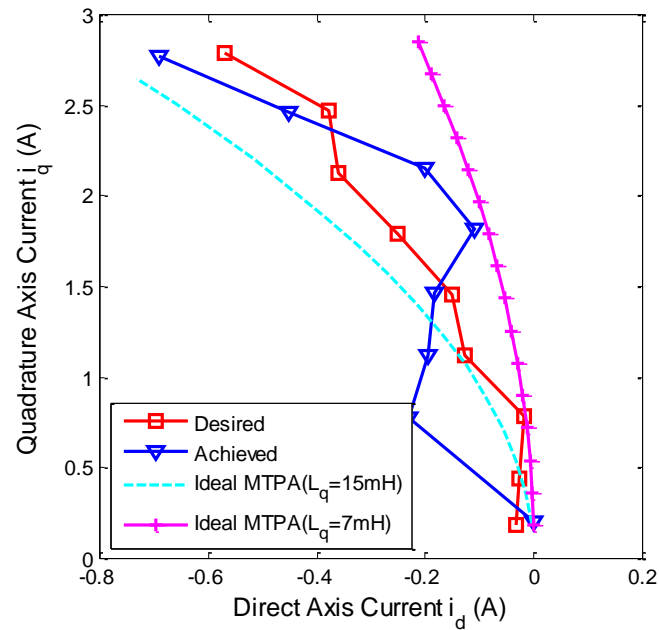


Figure 7-11 : i_d, i_q trajectory at 800 RPM obtained by the algorithm is marked by ∇ . Trajectory computed during motor training is marked by squares. Two dotted lines show the trajectories computed using constant motor model.

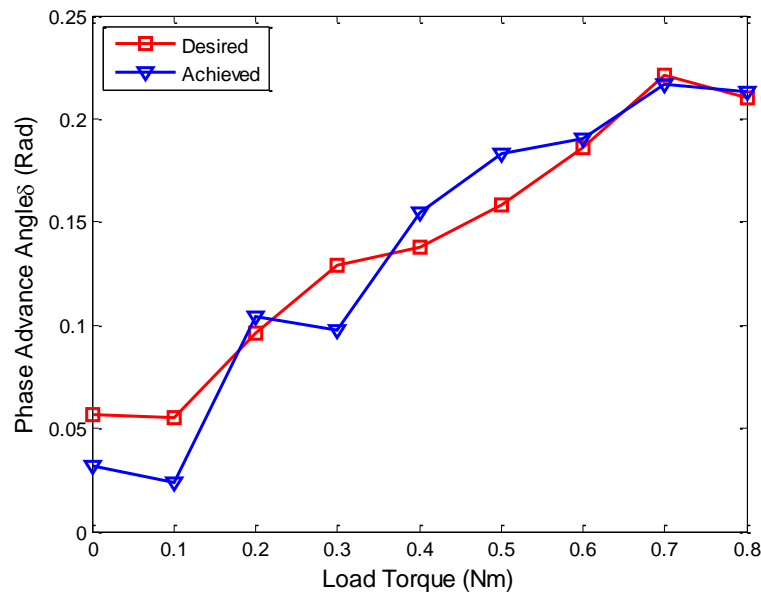


Figure 7-12: Phase advance angles achieved at steady state for 700 RPM are marked by ∇ . Angles computed during motor training for generating the D_M matrix are marked by squares.

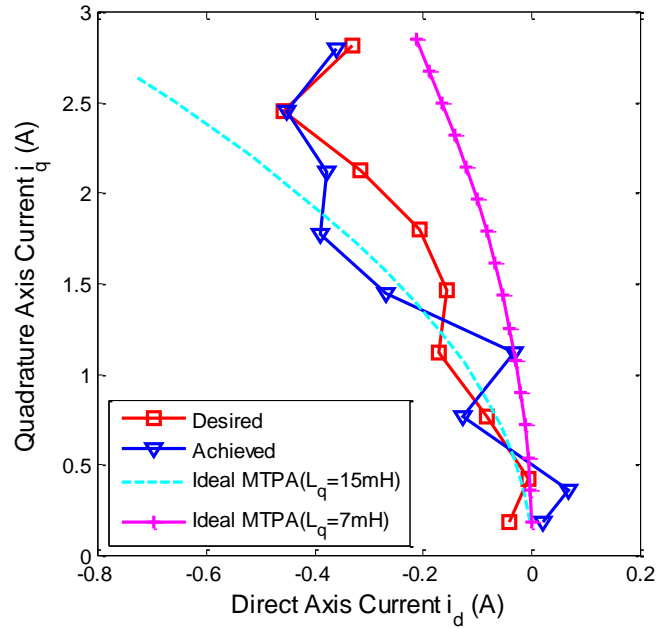


Figure 7-13: i_d, i_q trajectory at 700 RPM obtained by the algorithm is marked by ∇ . Trajectory computed during motor training is marked by squares. Two dotted lines show the trajectories computed using constant motor model.

7.4. Speed Variation at Constant Load Torque

To test the algorithm performance with changes in operating speed, the commanded speed was varied keeping the load torque at a constant level. Results are shown in Figure 7-14 through Figure 7-23 in a similar fashion. Speed was varied at 50 RPM intervals as shown in Figure 7-14. Estimated torque increases with the increase in speed to compensate for higher viscous damping as seen in Figure 7-15. The generated phase advance angle and contribution from the perturbation algorithm are shown in Figure 7-16 and Figure 7-17 respectively. The voltage magnitude generated by the PI controller is shown in Figure 7-18. Significant change in voltage level is observed unlike the one generated for load torque

variation shown in Figure 7-8. This is due to the fact that, with the increase in speed, the back EMF voltage content increases, contributing largely in increasing the required voltage level. q and d axis currents are shown in Figure 7-19 and Figure 7-20 which have little variations because of smaller changes in required torque level. Figure 7-21 shows the DC link input power variation which was found to be significantly smaller than the previously calculated minimum values.

Steady state performance of the control scheme can be better analyzed from Figure 7-22 and Figure 7-23. An excellent match between desired and achieved phase advance angles was observed at these speed-torque levels. Thus, the i_d, i_q trajectory followed the pre-computed values as well as seen in Figure 7-23.

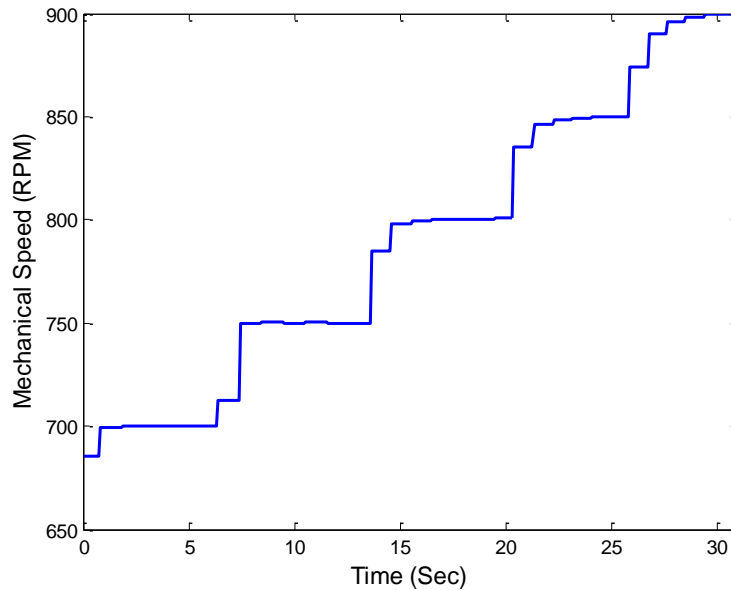


Figure 7-14: Speed response at constant load torque of 0.6 Nm.

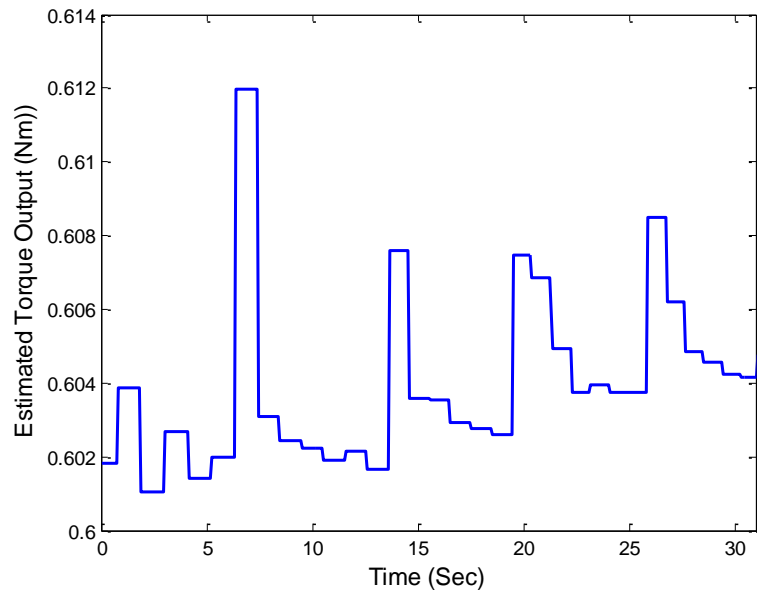


Figure 7-15: Estimated torque output at 0.6 Nm load torque. Generated torque increases with the increase in speed to overcome additional damping.

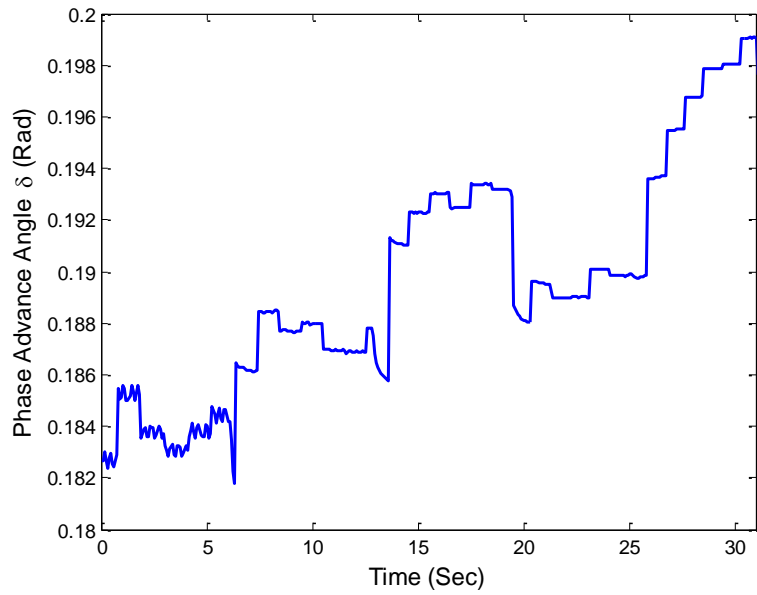


Figure 7-16: Phase advance angle generated by the control scheme for different speeds at 0.6 Nm load torque.

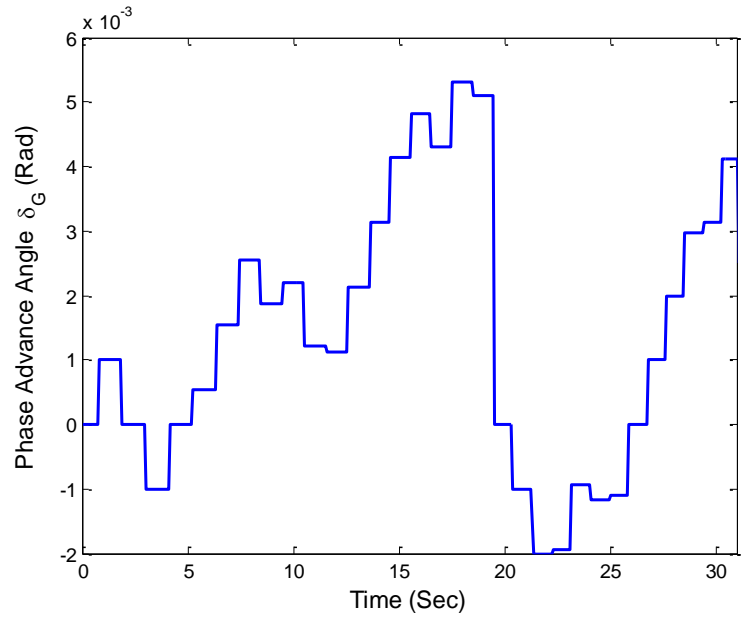


Figure 7-17: Contribution of phase advance angle variation from perturbation algorithm for different speeds at 0.6 Nm load torque.

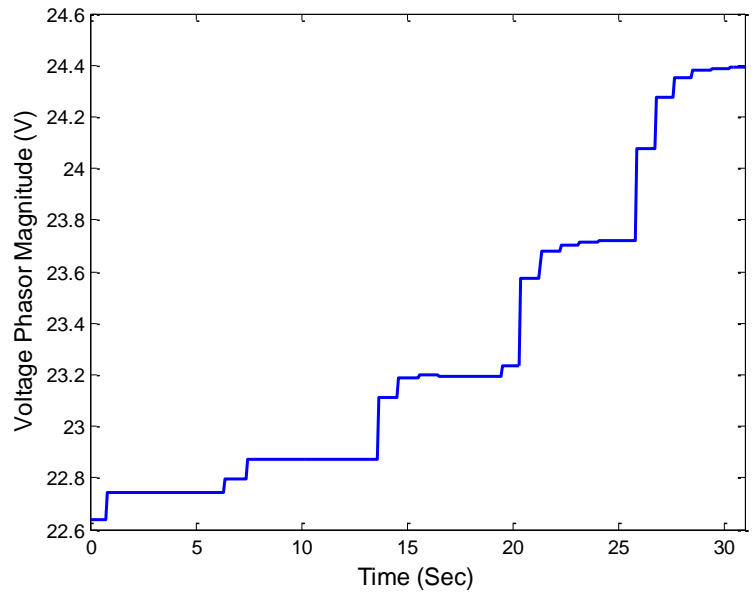


Figure 7-18: Voltage magnitude during speed variation at 0.6 Nm load torque (Filtered value is shown).

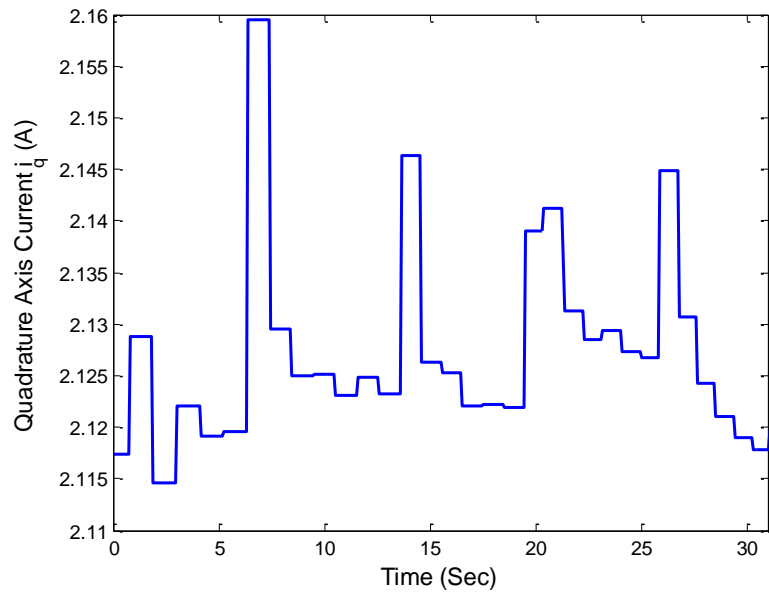


Figure 7-19: Quadrature axis current i_q during speed variation at 0.6 Nm load torque (Filtered value is shown).

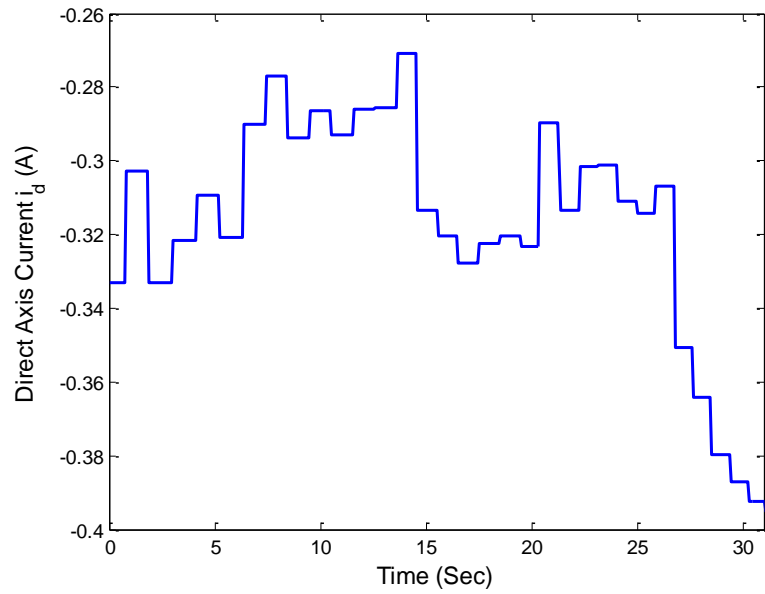


Figure 7-20: Direct axis current i_d during speed variation at 0.6 Nm load torque (Filtered value is shown).

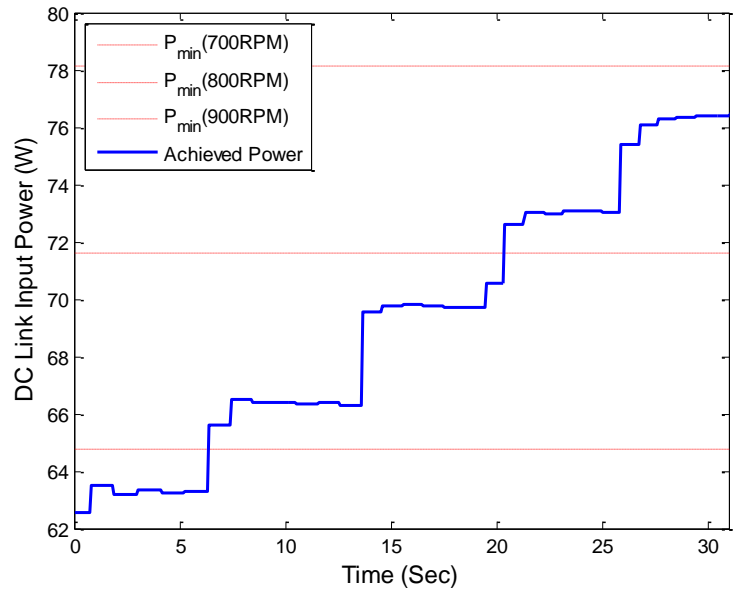


Figure 7-21: DC Link input power at 0.6 Nm while step change in speed command was introduced at 50 RPM interval starting from 700 RPM and ending at 900 RPM. Dotted lines represent the minimum achievable power levels computed during motor training.

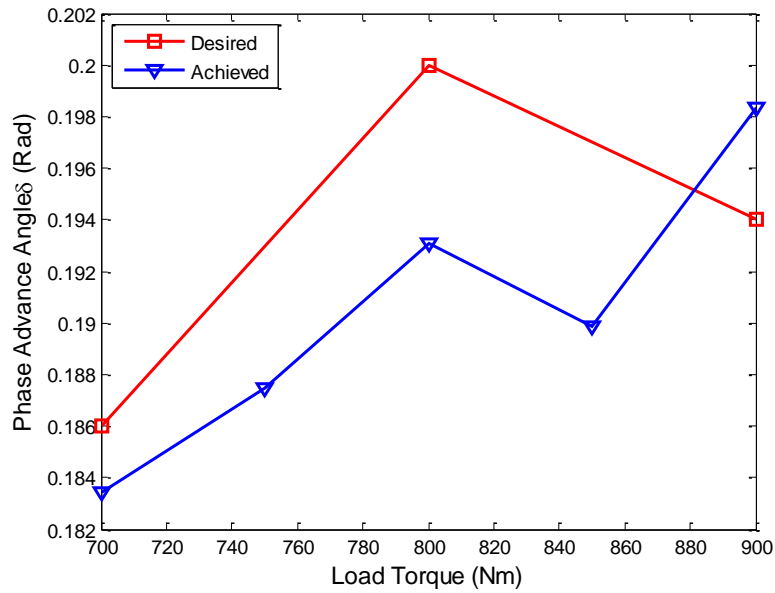


Figure 7-22: Phase advance angles achieved at steady state for 0.6 Nm are marked by ∇ . Angles computed during motor training for generating the D_M matrix are marked by squares.

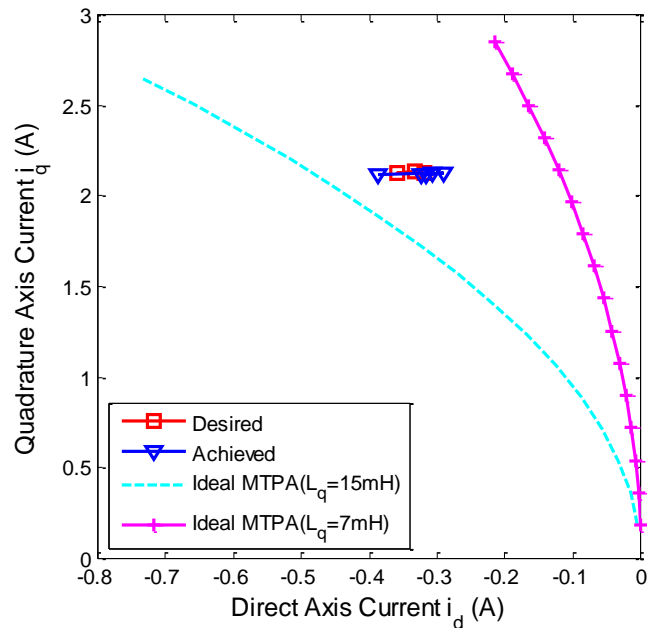


Figure 7-23: i_d, i_q trajectory at 0.6 Nm obtained by the algorithm is marked by ∇ . Trajectory computed during motor training is marked by squares. Two dotted lines show the trajectories computed using constant motor model.

7.5. Effect of Gradient Descent Compensation

To assess the contribution of the perturbation algorithm for altering δ , the motor was operated twice at the same speed-torque condition. The first run was performed under normal conditions with full contribution of the proposed scheme. Another run was performed with turning off the gradient descent algorithm by forcefully making δ_G zero. The motor was operated at 1000 RPM at 0.4 Nm load torque. A step change in load torque was introduced making the total load torque equal to 0.8 Nm. This additional load torque was removed after approximately 20 seconds. Figure 7-24 shows the glitches in the speed response due to sudden application and removal of load torque. The DC link power input is shown in Figure 7-25 where only minute differences were observed. The difference in power level depends on the speed-torque pair the motor is operating and the estimation

accuracy of the estimation matrix. The region where there is a large error between the estimated and actual optimum phase advance angle, the difference in power input level by turning the perturbation algorithm on or off can make a significant difference at steady state.

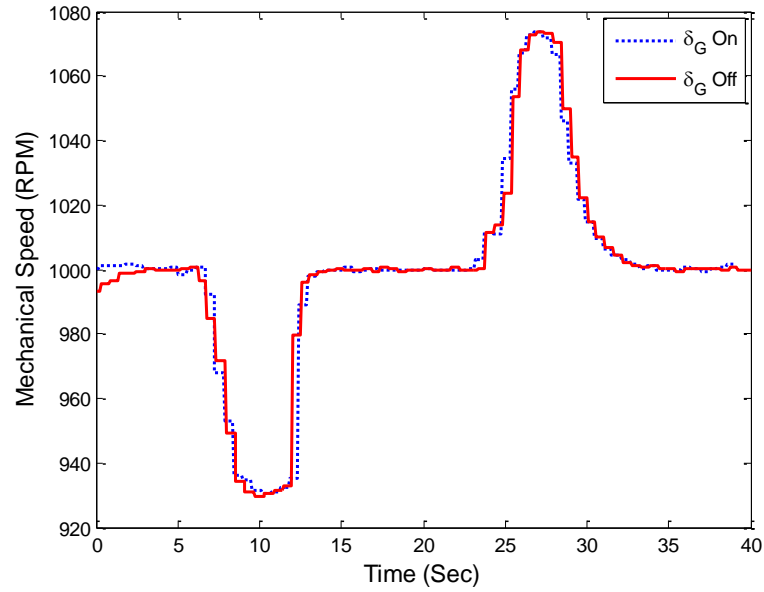


Figure 7-24: Speed variation due to application of load torque at 1000 RPM. Speed response shows two glitches generating from the application and removal of sudden load torque.

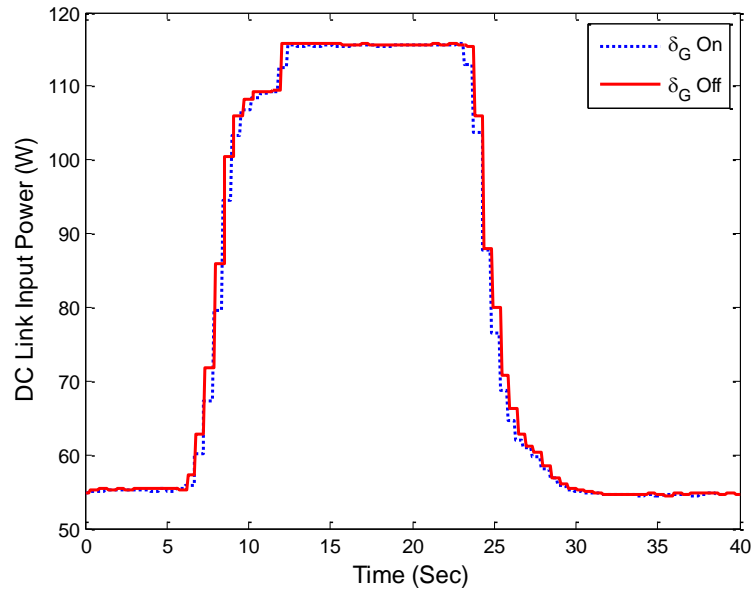


Figure 7-25: DC link input power variation at 1000 RPM. The dotted line represents the power input with perturbation whereas the solid line is for phase advance angle solely estimated by D_M .

7.6. Steady State Current Wave Shapes

In all the previous sections, all the quantities shown from experimental results were the filtered quantities free from high frequency switching ripples. To demonstrate the performance of the voltage source inverter and also the generated reference voltage, unfiltered quantities will be shown in this section.

The DC link input power at 900 RPM is shown in Figure 7-26. Since the motor was running at constant speed, ripple in DC link input power indicates the presence of torque ripple in the motor. The torque ripple can be explained from the shapes of the quadrature and direct axis currents i_q and i_d shown in Figure 7-27 and Figure 7-28 respectively. The dotted lines in both figures represent the average values used throughout the experiments.

Three phase stator currents are shown in Figure 7-29. Since proper current regulation was not performed, significant harmonic components are seen in the stator currents. A PI controller with faster response for speed regulation would improve the result but with risk of going into an unstable region.

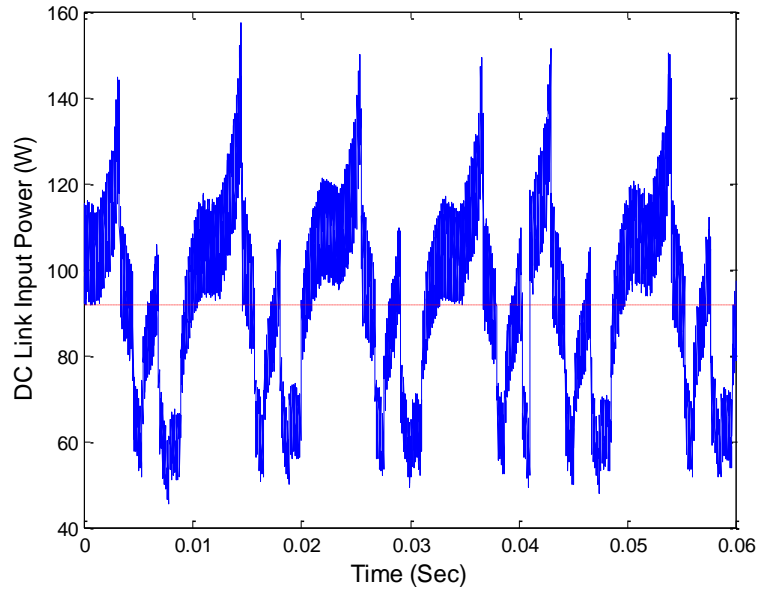


Figure 7-26: Unfiltered DC link input power at 900 RPM.

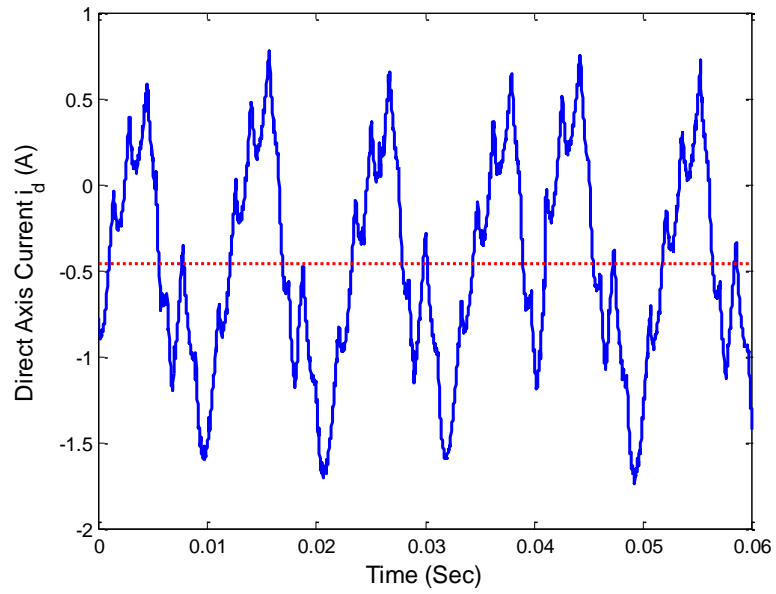


Figure 7-27: Unfiltered direct axis current i_d at 900 RPM.

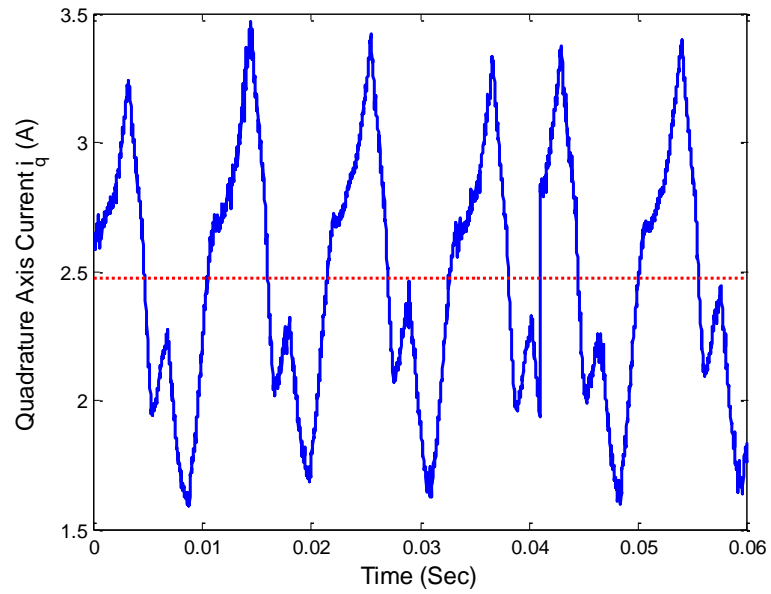


Figure 7-28: Unfiltered quadrature axis current i_q at 900 RPM.

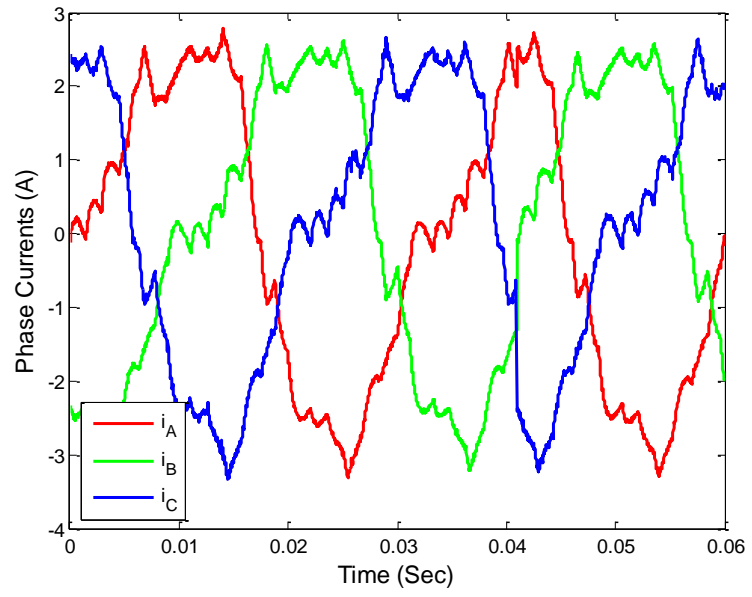


Figure 7-29: Unfiltered three phase current at 900 RPM.

CHAPTER VIII

CONCLUSION

A robust control algorithm for PMSMs is proposed in this research that would achieve MPPA operation without needing phase current measurements. Most of the parameter dependent control schemes developed so far, do not include any technique to cope with unexpected changes in operating conditions. Conversely, schemes based on search algorithms appear to be robust against unexpected parameter variation, but suffer from poor dynamic response. The proposed method is rather a hybrid scheme, having a-priori knowledge as well as a search based algorithm.

The control mechanism is developed based on only the DC link power measurement, which makes the algorithm a cost effective solution. The self-converging nature of the algorithm makes it unsusceptible self-induced instability and reduces the risk of system failure. Stability analysis of the closed loop system also ensures a stable operating region of the scheme. The phase advance angle generation algorithm based on the estimation matrix ensures satisfactory dynamic performance when rapid variations in operating speed or load torque is introduced. Integration of the perturbation technique based on a gradient descent algorithm reduces the possibility of functioning in an inefficient region regardless of the operating condition and motor parameters. Further improvements were made by reducing

switching loss using a minimum loss space vector PWM. Achieving MTPA trajectory without phase current feedback appeared to be a challenging task that was successfully performed by the control algorithm. Both simulation and experimental results validated the ability of the control scheme in attaining efficient operations.

BIBLIOGRAPHY

- [1] R. Saidur, “A review on electrical motors energy use and energy savings,” *Renewable and Sustainable Energy Reviews*, vol. 14, no. 3, pp. 877–898, Apr. 2010.
- [2] B. C. Mecrow and a. G. Jack, “Efficiency trends in electric machines and drives,” *Energy Policy*, vol. 36, no. 12, pp. 4336–4341, Dec. 2008.
- [3] A. Binder, “Potentials for energy saving with modern drive technology — a survey,” in *Proc. of IEEE International Symposium on Power Electronics, Electrical Drives, Automation and Motion*, 2008, pp. 90–95.
- [4] C. T. Pan and S. M. Sue, “A linear maximum torque per ampere control for IPMSM drives over full-speed range,” *IEEE Transactions on Energy Conversion*, vol. 20, no. 2, pp. 359–366, Jun. 2005.
- [5] Z. Zhu, Y. Chen, and D. Howe, “Online optimal flux-weakening control of permanent-magnet brushless AC drives,” *IEEE Transactions on Industry Applications*, vol. 36, no. 6, pp. 1661–1668, 2000.
- [6] H. Murakami, Y. Honda, H. Kiriyama, S. Morimoto, and Y. Takeda, “The performance comparison of SPMSM, IPMSM and SynRM in use as air-conditioning compressor,” in *Proc. of IEEE Industry Applications Society Annual Meeting*, 1999, vol. 2, pp. 840–845.
- [7] L. Chen, R. Davis, S. Stella, T. Tesch, and A. Fischer-Antze, “Improved control techniques for IPM motor drives on vehicle application,” in *Proc. of IEEE Industry Applications Society Annual Meeting*, 2002, vol. 3, pp. 2051–2056.
- [8] B. H. Bae and S. K. Sul, “Practical design criteria of interior permanent magnet synchronous motor for 42V integrated starter-generator,” in *Proc. of IEEE International Electric Machines and Drives Conference, (IEMDC)*, 2003, vol. 2, pp. 656–662.
- [9] D. Anton, K. Young-kwan, L. Sang-joon, and L. Sang-taek, “Robust self-tuning MTPA algorithm for IPMSM drives,” in *Proc. of IEEE Industrial Electronics, (IECON)*, 2008, pp. 1355–1360.

- [10] P. Niazi, H. A. Toliyat, and A. Goodarzi, "Robust maximum torque per ampere (MTPA) control of PM-assisted SynRM for traction applications," *IEEE Transactions on Vehicular Technology*, vol. 56, no. 4, pp. 1538–1545, 2005.
- [11] P. C. Krause, O. Wasynczuk, S. D. Sudhoff, and S. Pekarek, *Analysis of electric machinery and drive systems*. Wiley. com, 2013.
- [12] S. C. Carpiuc, D. I. Patrascu, and C. Lazar, "Optimal torque control of the interior permanent magnet synchronous machine," in *Proc. of IEEE International Symposium on Information, Communication and Automation Technologies, (ICAT)*, 2011, pp. 1–8.
- [13] P. Pillay and R. Krishnan, "Modeling, simulation, and analysis of permanent-magnet motor drives. II. The brushless DC motor drive," *IEEE Transactions on Industry Applications*, vol. 25, no. 2, pp. 274–279, 1989.
- [14] T. A. Lipo, *Vector control and dynamics of AC drives*. Oxford University Press, USA, 1996.
- [15] K. Nakamura, K. Saito, and O. Ichinokura, "Dynamic analysis of interior permanent magnet motor based on a magnetic circuit model," *IEEE Transactions on Magnetics*, vol. 39, no. 5, pp. 3250–3252, Sep. 2003.
- [16] Y. Yan, J. Zhu, H. Lu, Y. Guo, and S. Wang, "Study of a PMSM model incorporating structural and saturation saliencies," in *Proc. of IEEE International Conference on Power Electronics and Drives Systems, (PEDS)*, 2007, pp. 575–580.
- [17] R. Nalepa and T. Orłowska-Kowalska, "Optimum trajectory control of the current vector of a nonsalient-pole PMSM in the field-weakening region," *IEEE Transactions on Industrial Electronics*, vol. 59, no. 7, pp. 2867–2876, 2012.
- [18] R. Martis, N. Gupta, S. Sankar, and V. Rao, "Permanent magnetic materials with low reversible temperature coefficient," *IEEE Transactions on Magnetics*, pp. 948–950, 1979.
- [19] T. Sebastian, "Temperature effects on torque production and efficiency of PM motors using NdFeB magnets," *IEEE Transactions on Industry Applications*, vol. 3, no. 2, pp. 353–357, 1995.
- [20] Y. Zou, M. Elbuluk, and Y. Sozer, "A complete modeling and simulation of induction generator wind power systems," in *Proc. of IEEE Industry Applications Society Annual Meeting*, 2010, no. 1, pp. 1–8.
- [21] R. H. Park, "Two-reaction theory of synchronous machines generalized method of analysis-part I," *Transactions of the American Institute of Electrical Engineers*, vol. 48, no. 3, pp. 716–727, Jul. 1929.

- [22] P. Pillay and R. Krishnan, "Modeling, simulation, and analysis of permanent-magnet motor drives. I. The permanent-magnet synchronous motor drive," *IEEE Transactions on Industry Applications*, vol. 25, no. 2, pp. 265–273, 1989.
- [23] P. Pillay and R. Krishnan, "Modeling of permanent magnet motor drives," in *Proc. of Robotics and IECON Conferences*, 1987, pp. 289–293.
- [24] A. Consoli, G. Scarcella, G. Scelba, and A. Testa, "Steady-state and transient operation of IPMSMs under maximum-torque-per-ampere control," *IEEE Transactions on Industry Applications*, vol. 46, no. 1, pp. 121–129, 2010.
- [25] A. Consoli, G. Scarcella, G. Scelba, and S. Sindoni, "Modeling control of IPM synchronous motors," in *Proc. of IEEE Power and Energy Society General Meeting-Conversion and Delivery of Electrical Energy in the 21st Century*, 2008, pp. 1–6.
- [26] J. Kang, "General purpose permanent magnet motor drive without speed and position sensor," *Yaskawa Electric Corp., Japan, Yaskawa Application Note WP. AFD*.
- [27] T. M. Jahns, G. B. Kliman, and T. W. Neumann, "Interior permanent-magnet synchronous motors for adjustable-speed drives," *IEEE Transactions on Industry Applications*, vol. IA-22, no. 4, pp. 738–747, Jul. 1986.
- [28] S.Y. Jung, J. Hong, and K. Nam, "Current minimizing torque control of IPMSM using Ferrari's method," *IEEE Transactions on Power Electronics*, vol. 28, no. 12, pp. 5603–5617, 2013.
- [29] G. Cardano, *The Rules of Algebra (Ars Magna)*, translated and edited by T. Richard Witmer. Dover Publications, Inc., Mineola, 2007.
- [30] H. Kim, J. Hartwig, and R. D. Lorenz, "Using on-line parameter estimation to improve efficiency of IPM machine drives," in *Proc. of IEEE Power Electronics Specialists Conference, (PESC)*, 2002, vol. 2, pp. 815–820.
- [31] Y.S. Kim and S.K. Sul, "Torque control strategy of an IPMSM considering the flux variation of the permanent magnet," in *Proc. of IEEE Industry Applications Society Annual Meeting*, 2007, pp. 1301–1307.
- [32] S. Morimoto, M. Sanada, and Y. Takeda, "Wide-speed operation of interior permanent magnet synchronous motors with high-performance current regulator," *IEEE Transactions on Industry Applications*, vol. 30, no. 4, pp. 920–926, 1994.
- [33] S. Morimoto, T. Ueno, M. Sanada, A. Yamagiwa, Y. Takeda, and T. Hirasaka, "Effects and compensation of magnetic saturation in permanent magnet synchronous motor drives," in *Proc. of IEEE Industry Applications Society Annual Meeting*, 1993, no. 2, pp. 59–64.

- [34] R. Bellman, "Dynamic programming and Lagrange multipliers," in *Proc. of the National Academy of Sciences of the United States of America*, 1956, vol. 42, p. 767.
- [35] S. Morimoto, K. Hatanaka, Y. Tong, Y. Takeda, and T. Hirasa, "Servo drive system and control characteristics of salient pole permanent magnet synchronous motor," *IEEE Transactions on Industry Applications*, vol. 29, no. 2, pp. 338–343, 1993.
- [36] Y. R. Mohamed and T. K. Lee, "Adaptive self-tuning MTPA vector controller for IPMSM drive system," *IEEE Transactions on Energy Conversion*, vol. 21, no. 3, pp. 636–644, Sep. 2006.
- [37] G. C. Goodwin and K. S. Sin, *Adaptive filtering prediction and control*. Courier Dover Publications, 2013.
- [38] G. Rang, J. Lim, K. Nam, H. Bin Ihm, and H. G. Kim, "A MTPA control scheme for an IPM synchronous motor considering magnet flux variation caused by temperature," in *Proc. of IEEE Applied Power Electronics Conference and Exposition (APEC)*, 2004, vol. 3, no. 5, pp. 1617–1621.
- [39] C. Mademlis, I. Kioskeridis, and N. Margaritis, "Optimal efficiency control strategy for interior permanent-magnet synchronous motor drives," *IEEE Transactions on Energy Conversion*, vol. 19, no. 4, pp. 715–723, Dec. 2004.
- [40] R. S. Colby and D. W. Novotny, "An efficiency-optimizing permanent-magnet," *IEEE Transactions on Industry Applications*, vol. 24, no. 3, pp. 462–469, 1988.
- [41] S. Kim, Y.D. Yoon, S.K. Sul, K. Ide, and K. Tomita, "Parameter independent maximum torque per ampere (MTPA) control of IPM machine based on signal injection," in *Proc. of IEEE Applied Power Electronics Conference and Exposition (APEC)*, 2010, no. 1, pp. 103–108.
- [42] S. Bolognani, R. Petrella, A. Prearo, and L. Sgarbossa, "Automatic tracking of MTPA trajectory in IPM motor drives based on AC current injection," *IEEE Transactions on Industry Applications*, vol. 47, no. 1, pp. 105–114, Jan. 2011.
- [43] A. Consoli and A. Abela, "Transient performance of permanent magnet AC motor drives," *IEEE Transactions on Industry Applications*, vol. IA-22, no. 1, pp. 32–41, Jan. 1986.
- [44] D. W. Marquardt, "An algorithm for least-squares estimation of nonlinear parameters," *Journal of the Society for Industrial & Applied Mathematics*, vol. 11, pp. 431–441, 1963.
- [45] M. Haque and M. Rahman, "Dynamic model and parameter measurement of interior permanent magnet synchronous motor," in *Proc. of Australasian Universities Power Engineering Conference (AUPEC)*, 2006, pp. 10–13.

- [46] Y. Sozer and D. A. Torrey, “Adaptive torque ripple control of permanent magnet brushless DC motors,” in *Proc. of IEEE Applied Power Electronics Conference and Exposition (APEC)*, 1998, pp. 86–92.
- [47] Y. Sozer, H. Kaufman, and D. A. Torrey, “Direct model reference adaptive control of permanent magnet brushless DC motors,” in *Proc. of the 1997 IEEE International Conference on Control Applications*, 1997, pp. 633–638.
- [48] Z. Gajic, *Linear dynamic systems and signals*. Prentice Hall/Pearson Education, 2003.
- [49] G. B. Arfken, H. J. Weber, and L. Ruby, *Mathematical methods for physicists*. Academic press, 2005.
- [50] R. Kazmierkowski, Marian P and Krishnan, *Control in power electronics: selected problems*. Academic press, 2002.
- [51] V. Der Broeck, H. Willi, H. C. Skudelny, and G. V. Stanke, “Analysis and realization of a pulsewidth modulator based on voltage space vectors,” *IEEE Transactions on Industry Applications*, vol. 24, no. 8716204, pp. 142–150, 1988.
- [52] A. M. Trzynadlowski and S. Legowski, “Minimum-loss vector PWM strategy for three-phase inverters,” *IEEE Transactions on Power Electronics*, vol. 9, no. 1, pp. 26–34, 1994.
- [53] Y. Sozer, “Direct adaptive control of permanent magnet motors,” Rensselaer Polytechnic Institute, 2000.
- [54] Y. Zou, “Modeling, control and maximum power point tracking (MPPT) of doubly-fed induction generator (DFIG) wind power system,” University of Akron, 2012.